GEOMATICS
ENGINEERING

UCGE Reports
Number 20215

Department of Geomatics Engineering

High-Sensitivity GPS L1 Signal Analysis for Indoor Channel Modelling

(URL: http://www.geomatics.ucalgary.ca/links/GradTheses.html)

by

John Robert A. Watson

April 2005

UNIVERSITY OF
CALGARY

THE UNIVERSITY OF CALGARY

High-Sensitivity GPS L1 Signal Analysis for Indoor Channel Modelling

by

John Robert A. Watson

A THESIS
SUBMITTED TO THE FACULTY OF GRADUATE STUDIES
IN PARTIAL FULFILLMENT OF THE REQUIREMENTS FOR THE
DEGREE OF MASTER OF SCIENCE

DEPARTMENT OF GEOMATICS ENGINEERING

CALGARY, ALBERTA

April, 2005

Abstract

New applications of indoor positioning and navigation demand GPS-level performance but in environments where GPS suffers performance degradation and failures. Development of GPS technologies to function indoors requires means to validate receiver performance without the time, complexity, and cost required to field test each development. Propagation models that can accurately predict signal behaviour indoors could potentially be used in signal simulators to test hardware in the laboratory with repeatable results.

A limited understanding of indoor GPS signal behaviour has prevented the creation of adequate propagation models to date. Existing models do not account for both fading and ranging errors that degrade GPS indoor performance. In this thesis, high-bandwidth raw GPS data are analyzed with high-sensitivity techniques to characterize fading and multipath characteristics in a pair of indoor environments. The measured behaviour suggests characteristics required for a novel channel model, and provides an estimate of the possible performance improvement gained in using these models as opposed to existing channel models.

Acknowledgements

- I owe everything I've been able to accomplish to my parents, who have supported my pursuits as a student for far longer than could have been expected. I can't imagine where I would be without your guidance.

- Thanks to my supervisors, Dr. Gérard Lachapelle and Dr. Richard Klukas. Their support, direction, and especially their unbelievable patience have made this work possible.

- Nokia Mobile Telephones Ltd. is acknowledged for providing data, expertise, and financial support for this research.

- The Alberta Informatics Circle of Research Excellence (iCORE) and the Natural Sciences and Engineering Research Council of Canada (NSERC) are acknowledged for their financial support.

- Thanks to my colleagues and associates in Geomatics Engineering, who have made this a personally and professionally rewarding experience. I never would have believed that I could work with people from ten different countries and have so much in common! I owe special thanks to several people for their tireless ability to answer my unending questions: Changlin Ma, Mark Petovello, Glenn MacGougan, Olivier Julien, and many others. To my many, many office-mates over the last 30 months, thanks for keeping things light.

- And of course, my deepest thanks to Angela for helping me keep things in perspective in the down times, and for giving me a reason to succeed.

Table of Contents

List of Tables

List of Figures

Notation

Abbreviations and Acronyms

3D	Three-Dimensional
ADC	Analog-to-Digital Converter
A-GPS	Assisted-GPS
AWGN	Additive White Gaussian Noise
BPSK	Binary Phase-Shift Keying
C/A	Coarse/Acquisition PRN code (GPS civilian code)
C/N_o	Carrier to noise density ratio
CDF	Cumulative Density Function
CDMA	Code Division Multiple Access
DLL	Delay-Locked Loop
DOP	Dilution of Precision
EDOP	East Dilution of Precision
EPE	Estimated Pseudorange Error
FDE	Fault Detection and Exclusion
GNSS	Global Navigation Satellite System
GPS	Global Positioning System
HOW	Handover Word
HS(GPS)	High-Sensitivity (GPS)
INS	Inertial Navigation System
ISI	Intersymbol Interference
L1	GPS Carrier at 1575.42 MHz
LHCP	Left-Hand Circularly Polarized
LO	Local Oscillator
LOS	Line of Sight
LTI	Linear Time-Invariant
MEO	Medium Earth Orbit
MUSIC	Multiple Signal Classification algorithm
NBP	Narrowband Power
NDOP	North Dilution of Precision
NLOS	Non-Line of Sight
NRID	NLOS Range-rate Induced Doppler
P(Y)	GPS Precise (encrypted) code
PDF	Probability Density Function
PDP	Power Delay Profile
PLAN	Position, Location, and Navigation group
PLL	Phase-Locked Loop

PPS	Pulse per Second
PRN	Pseudo-Random Noise code / also used to refer to a signal with a specific PRN code
PSD	Power Spectral Density
RHCP	Right-Hand Circularly Polarized
RF	Radio Frequency
RMS	Root Mean Square
RV	Random Variable
SMR	Signal to Multipath Ratio
SNR	Signal to Noise Ratio
STEC	Slant TEC (see TEC)
SV	Space Vehicle (GPS Satellite)
TEC	Total Electron Content
TECU	TEC Unit (see TEC)
TOA	Time of Arrival
TOW	Time of Week
TTFF	Time-to-first-fix
UERE	User Equivalent Range Error
UTC	Universal Time Coordinated
UTSFM	Urban Three-State Fade Model
VDOP	Vertical Dilution of Precision
VTEC	Vertical TEC (see TEC)
WBP	Wideband Power

Symbols

δ	Parameter correction vector
ϵ	Error value
μ	Mean value
ϕ	Phase value
$\dot{\phi}$	Doppler
$\ddot{\phi}$	Doppler drift
σ	Standard deviation
σ^2	Variance
$\mathbf{A}$	Design matrix
B	Bandwidth
$\mathbf{C_l}$	Observable variance-covariance matrix
$\mathbf{C_x}$	Parameter variance-covariance matrix
G	Gain
I/i	Inphase

j	Imaginary number (square root of -1)
J_d	Doppler jerk
$\mathbf{l}$	Observation vector
N_o	Noise density
P	Power
Q/q	Quadrature
$\mathbf{Q_x}$	Cofactor matrix
$\mathbf{r}$	Residual vector
$R(\cdot)$	Autocorrelation function
T	Period or time / Temperature
$\mathbf{x}$	Parameter vector

Usage Note: While the abbreviation ‘PRN’ refers to a pseudorandom noise code, it is used in this thesis as an identifier for the entire signal received from a GPS satellite. The satellites themselves are often also referred to simply by the number of the PRN they transmit.

Chapter 1

Introduction

1.1 The Indoor Positioning Problem

Since its launch in the 1980s, the Global Positioning System (GPS) has emerged as a dominant positioning technology by offering worldwide availability, precise location and navigation capability, low cost, and portability for end-users. These characteristics make GPS a desirable choice for applications of personal positioning and navigation. Various emerging applications require positioning of users indoors, however, and in other environments where typical GPS receivers suffer degraded performance or complete failure. One of the most important potential applications of personal positioning is emergency call location in cellular telephone networks, for which both availability and accuracy are critical. This is particularly important due to the U.S. Federal Communications Commission's E-911 mandate and a similar initiative by the European Commission (FCC, 1996). Research into the performance and characteristics of GPS in signal-degraded indoor environments is required if it is to be developed as a possible solution to the indoor positioning problem.

1.2 Indoor GPS Challenges

GPS suffers from two basic limitations indoors:

1. tracking of multipath-affected signals degrades accuracy, and
2. tracking fails due to low signal power or, if tracking is possible, accuracy is degraded by noisy measurements.

System developers and researchers have been challenged to overcome these limitations and develop receivers that are functional and accurate indoors. A first step in doing this is thoroughly understanding the failure mechanisms. The two basic limitations are briefly reviewed in the remainder of this section. For readers who are unfamiliar with GPS technology, a review of GPS fundamentals is provided in Appendix A. More comprehensive resources for GPS information include Parkinson & Spilker (1996), Kaplan (1996), and Hoffman-Wellenhof et al. (2001).

1.2.1 Multipath Tracking Errors

The Global Positioning System is fundamentally a timing system, relying on line-of-sight (LOS) propagation, at the speed of light, between satellites and users to ensure accurate ranges, and therefore positions. This contrasts with systems designed for digital communications, whose measure of success is the rate of bit errors encountered at the receiver. In communications systems, the propagation path is unimportant if the desired bit-error-rate can be achieved. With GPS, any deviation from the LOS path disrupts timing, and therefore compromises accuracy.

The LOS signal propagation channel consists of free space and Earth's atmosphere. Even on the LOS channel, timing errors are not insignificant for metre-level positioning, but these effects have been modelled by many researchers and can be largely mitigated by existing receiver technologies and techniques (see, e.g., Ray, 2003; Parkinson & Spilker, 1996; and Hoffman-Wellenhof et al., 2001). Established techniques include the use of dual-frequency receivers to mitigate ionospheric effects, and single- and double-differencing to largely mitigate most other errors including tropospheric, orbital, and clock errors (Lachapelle, 2002). The remaining significant errors are due to non-line-of-sight (NLOS) propagation—with NLOS effects collectively referred to as *multipath*—and receiver noise.

NLOS propagation increases the length of a GPS signal's propagation path, and is therefore a source of ranging error both indoors and out. Outdoors, NLOS effects can be insignificant or severe depending on circumstances. In the best of cases, minor reflections with low power may be insignificant when strong LOS signals are also available. Conversely, in cases where only a reflected signal is available, positioning is severely affected. Most outdoor cases fall somewhere in between these two extremes, with combinations of LOS and NLOS signals available to cause varying degrees of position degradation.

Indoors, there is a high likelihood of NLOS propagation. Often, no LOS signals are available indoors due to obstruction by various materials. The medium of propagation between a satellite and indoor receiver may range from an open window to thick concrete, metal, or other obstructive media. In addition, a multitude of surrounding objects are available to cause reflections and scattering. The complexity and variation of and among indoor environments have made characterization of NLOS effects difficult to impossible as yet.

1.2.2 Attenuation and Fading

The minimum received signal level of the GPS signal under open-sky conditions is defined as -160 dBW for the L1 coarse/acquisition (C/A) code, assuming a receiver antenna with hemispherical gain pattern (ICD200C, 2000). This power is spread over a large bandwidth by a code division multiple access (CDMA) technique, leading to a peak power spectral density (PSD) near -220 dBW/Hz, which is significantly lower than average radio frequency (RF) noise levels of about -204–208 dBW/Hz (Parkinson & Spilker, 1996; Pritchard, 1997; Ray, 2003). Thus, significant processing gain is required to extract GPS signals from noise even under ideal conditions.

Indoor signal levels are generally weaker than those received outdoors. Propagation through building materials induces anywhere from 0 dB to greater than 30 dB attenuation on LOS signals. In addition, the interference between multiple NLOS signals causes fading. Fading is particularly detrimental to GPS reception because signal levels become highly variable, with levels and temporal variations dependent on the characteristics of the environment. In the presence of strong multipath, extremely deep fades can result and can persist for seconds, minutes, or longer depending on environmental geometry.

1.2.3 Meeting the Challenges

Given the severe conditions encountered indoors, an understanding of NLOS characteristics is critical for indoor GPS performance improvement. New methods must be developed and tested to characterize both the net NLOS error observed indoors and the individual propagation effects thought to cause that error. Research aimed at understanding the propagation effects under various conditions has been conducted, along with practical development of technologies and techniques to mitigate the errors.

Studies of Error Effects

GPS errors due to multipath and signal strength degradation have been studied extensively in several classes of outdoor environments. Studies under forest canopies, in urban canyons, and in suburban environments have been conducted with the belief that multipath and fading effects in other similar environments would be comparable (e.g. MacGougan et al., 2002). Receiver technologies and algorithms have also been developed to partially mitigate the resultant position errors in such conditions. These technologies have not proven sufficient to enable accurate or reliable indoor performance, however. Indoor NLOS conditions and fading are extremely difficult to model, especially from a general perspective, because they may depend on very specific local multipath conditions, rather than more generic conditions as are often found outdoors.

A further difficulty in studying indoor error effects has been in simply receiving GPS signals indoors. Indoor studies have been limited by the very low signal levels until the recent developments of high-sensitivity (HS) receivers. Even with high-sensitivity receivers, understanding of indoor fading remains inadequate; signals still fall below HS receivers' tracking thresholds, and raw signal effects are masked by receiver processing.

Some specific studies of errors are reviewed in Chapter 3. It is clear from these studies that additional research is required to more thoroughly understand the effects of indoor propagation on the GPS signal.

Modern Technologies

Certain technologies have been developed to overcome the limitations of indoor GPS. The most significant include high-sensitivity GPS (HSGPS) and assisted-GPS (A-GPS), which are designed to improve tracking and acquisition of low-power signals. Information on these technologies can be found in Chansarkar & Garin (2000) and Syrjärinne (2001), for example, among numerous other references. Multipath error mitigation techniques have been developed for severe outdoor multipath conditions, but are not specifically designed for, nor suitable for, indoor conditions. For example, antennas that reject low-elevation signals are not necessarily suitable for indoor multipath rejection because of the likelihood of multipath from higher elevations. Other common techniques such as narrow correlator spacing may not be suitable for, or capable of, rejecting short-delay multipath. There is not yet a sufficient understanding of indoor NLOS propagation to develop techniques suitable for the unique conditions encountered indoors.

1.3 Research Overview

1.3.1 Motivation

The limited performance, availability, and understanding of indoor GPS is the overarching motivation for this research. An additional important motivation is the potential application of hardware GPS simulators to the testing and validation of GPS receivers designed for indoor operation. Simulators have the potential to provide repeatable and accurate tests of receivers in simulated indoor environments with much less expense and time than would be required for true field tests. However, simulator models must be capable of accurately reproducing the GPS-indoor channel in order to conduct valid tests.

1.3.2 Objective and Intended Contributions

Based on the aforementioned motivation, the objective of this research is to improve modelling of the GPS-indoor channel to advance receiver testing and development. The larger objective of developing and testing a complete novel channel model comprises a number of tasks. Major tasks include empirical measurement of channel effects, theoretical examination of propagation, synthesis of models, implementation, and verification and test. The primary scope of this research is limited to empirical channel measurement, with some theoretical consideration and attempts to synthesize a model framework. Some background on RF propagation, GPS errors, and channel modelling is required before more fully defining goals for this research, which will be done in Chapter 4. However, the major objectives are listed here, based on availability of raw GPS data to be introduced in Chapter 4:

1. Reception of weak indoor signals with high-sensitivity techniques
2. Identification of multipath signals and sources
3. Characterization of receiver performance degradations indoors
4. Development of model to accurately replicate performance degradations

An empirical research campaign can potentially contribute very significantly to the final objective listed above. An improved understanding of GPS-indoor propagation gives direction for future research intended to develop and test complete channel models. In addition, even without a full model, better understanding of propagation conditions will allow development of better GPS receiver technologies and algorithms. Development and test of techniques for channel measurements using live GPS signals in difficult indoor environments is, in itself, a major necessary task for improving future modelling of the GPS-indoor channel since measurement of channel characteristics is currently difficult with GPS signals indoors.

1.4 Thesis Outline

This thesis consists of eight chapters. Chapter 1 has introduced the indoor positioning problem and the overall objective of the research. Chapter 2 discusses theoretical considerations for RF propagation and the major error effects encountered by indoor GPS receivers. Chapter 3 presents additional background material on GPS performance studies and channel modelling, with specific models relevant to indoor GPS discussed. Based on these existing approaches, the requirements for a novel channel model are presented in Chapter 4. The data sets for analysis are introduced, and the specific objectives and techniques for analysis of these data sets discussed.

Chapter 5 focuses on implementation and test of the high-sensitivity analysis techniques used for indoor channel measurement, and includes some theoretical review of high-sensitivity techniques and challenges. Chapter 6 presents results from analysis of indoor GPS data sets using a number of high-sensitivity techniques. Chapter 7 takes the results of these analyses and synthesizes a limited propagation model framework on which future work might expand. Finally, conclusions and recommendations for future work are presented in Chapter 8.

Chapter 2

Propagation Effects and GPS Errors

GPS errors are a result of a number of basic propagation effects that are common to any wireless RF system. This chapter reviews the fundamental propagation effects encountered in a GPS-indoor channel, and the resultant errors as seen by a receiver indoors.

2.1 Fundamental Propagation Mechanisms

Free Space Propagation The ideal propagation path consists of free space with no intervening medium. Power is lost only due to geometric spreading; received power is deterministically defined by the transmitted power, antenna gain and aperture, and propagation distance according to the Friis free-space equation (Rappaport et al., 1997),

$$P_r = \frac{P_t G_t G_r \lambda^2}{(4\pi)^2 d^2 L}, \tag{2.1}$$

where P_t and P_r are transmitted and received powers respectively, G_t and G_r the transmitter and receiver antenna gains, λ the wavelength, d the transmitter-receiver distance, and L the fractional system losses.

Free-space loss is the primary mechanism of power loss in the GPS system, accounting for approximately 182.4 dB to 184.4 dB of power loss between the satellite and an unobstructed receiver, depending on satellite elevation (Ray, 2003). Because free-space loss is included in the definition of nominal GPS power available

(-160 dBW), it is not a concern for most users. However, this mechanism is an important factor in determining the level of possible multipath effects. By Equation 2.1, power loss is proportional to the square of the distance between transmitter and receiver. Thus, an NLOS source in close proximity to a receiver has much greater effect than one a long distance away, assuming rays from the two are emitted with equal power.

Diffraction According to Huygens' Principle (Parsons, 2000), each point on a propagating wavefront is a point source of new spherical waves. This is the source of a propagating plane wave, which is the sum of the forward-travelling energy. In the presence of an obstruction, the spherical wavefronts expand into the blocked region, allowing some energy to propagate into an LOS blockage. Diffraction, as this is known, is an important propagation mechanism for the GPS indoor channel where LOS blockages are common.

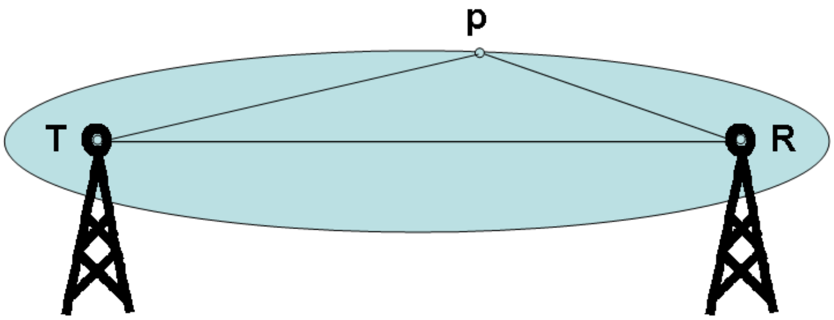

Figure 2.1: Fresnel Zone Geometry (2-D Representation)

Diffracted rays have power, phase, and polarization dependent on the specific situation. Diffraction causes some fading when obstructions are found within the first Fresnel zone between transmitter T and receiver R, even if the LOS ray is not blocked. The Fresnel zones are defined in 3-dimensional space by ellipsoids with the transmitter and receiver at the foci, and the surface defined as the points p where the excess path length $TpR - TR = n\lambda/2$, where n is an integer representing the Fresnel zone of interest (see Figure 2.1). If the first Fresnel zone is substantially free of obstructions, propagation is generally considered to be LOS. Losses due to diffraction begin to become significant as the first Fresnel zone is obstructed, and become severe when over half of that zone is blocked.

The radius of the Fresnel zone ellipsoid at a point between transmitter and receiver is approximately calculated as

$$r = \sqrt{\frac{n\lambda d_1 d_2}{d_1 + d_2}} \tag{2.2}$$

where d_1 and d_2 are the distance from transmitter and receiver respectively, and n is the integer representing the Fresnel zone of interest. In fact, this is an approximation valid only at a sufficient distance from the transmitter and receiver. This equation becomes invalid within several metres of the receiver. Near a GPS receiver, if the transmitter is considered infinitely distant, the first Fresnel zone radius is approximated as

$$r = \sqrt{\lambda(d_2 + \lambda/4)}. \tag{2.3}$$

On the satellite-to-ground GPS channel, most possible obstructions are near the receiver where the Fresnel zone radius is small. At the GPS L1 wavelength of approximately 0.19 m, the radius at 1 m distance is only about 0.44 m, increasing to 1.4 m at 10 m distance and about 4.4 m at 100 m away from the receiver. This implies that only the propagation medium within a small radius of the LOS path has any contribution to the diffracted rays observed indoors.

Reflection An RF wave incident on a regular surface has some of its energy transmitted into that surface and some reflected. The amount of energy transmitted and reflected depends on the smoothness of the surface, its electromagnetic characteristics at the frequency of interest, and the incident angle of the incoming wave (Rappaport et al., 1997).

In this thesis, reflection refers only to specular reflection. Diffuse reflection, or reflection from rough surfaces, will be categorized along with general scattering from small objects. Specular reflection is indicated in the situation where most of the radiation that is neither transmitted nor absorbed is re-emitted at an angle equal to that of the incident ray. The right-hand circularly polarized (RHCP) GPS signal often reverses polarization on specular reflection and actually becomes a form of elliptical polarization upon oblique reflection (Hoffman-Wellenhof et al., 2001). This is a major effect as most antennas are designed to receive only RHCP signals. The observed effect is a further attenuation of the signal in addition to that caused by absorption of the reflecting medium. In normal operational circumstances, this serves to mitigate the effects of multipath. For purposes of measuring and characterizing multipath, it limits the ability to detect and measure NLOS signals undergoing an odd number of reflections.

One more consideration relating to specular reflection is the nature of the point of reflection. While often considered an infinitesimal point source, Lavergnat & Sylvain (2000) state that a specular reflection originates from a finite area on the surface corresponding to the intersection of the reflecting surface and the cross-section of the first Fresnel zone at the reflector distance. If otherwise reflective surfaces are not regular over this entire area, much of the incident power is in fact scattered, rather than reflected. Thus, while large surfaces such as glass-sided buildings might effectively reflect GPS signals, smaller objects such as bus shelters or small windows might not.

Scattering Irregular reflectors and transmission media induce scattering of the incident ray in all directions, again with varying phase, power, and polarization effects (Rappaport et al., 1997). Generally, objects smaller than the wavelength of interest are effective random scatterers (Parsons, 2000), but other objects induce scattering as well depending on surface properties. Since scattering occurs in all directions, objects in any direction relative to the propagation path may be significant, although those objects that fall within the first Fresnel zone are of most concern. Due to the irregularity of this phenomenon, the sources and nature of scattered rays may change quickly and often. Signal amplitude, phase, and polarization may all be affected.

Shadowing and Blockage Shadowing can be taken to mean that the direct signal from transmitter to receiver is blocked (Rappaport et al., 1997), and only NLOS rays reach the receiver. In this thesis, such a condition is referred to as a "blockage." Shadowing shall refer to propagation through some medium which attenuates the signal, but does not significantly change its path. This is a significant effect indoors, since it can generally be assumed that even direct signals are shadowed by some building material.

Shadowing is, in fact, a combination of attenuation and scattering by the medium of propagation. Theoretically, the more uniform a medium, the less variation can be expected in the signal levels due to shadowing. Buildings present a range of uniform and non-uniform materials for propagation. A solid concrete wall is relatively uniform, whereas a wall composed of wood framing, electrical wiring, fasteners, and sheathing is not uniform. Signal effects due to buildings are thus expected to vary widely.

2.2 Signal Degradations in an RF Channel

2.2.1 Thermal Noise and Interference

Noise and interference degrade the performance of RF systems by obscuring the message signal. The nature of the noise must be modelled to determine how it may affect different types of systems. Relevant noise sources include in-receiver noise sources, external (ambient) noise, and external interference. Noise is often modelled as additive white Gaussian noise (AWGN), but this is only an approximation. More advanced noise modelling may be necessary depending on the application. Types of interference and their negative effects on GPS are reviewed herein.

Narrowband Interference

Narrowband interference is generally a man-made RF signal with some limited bandwidth, narrower than the signal of interest. It is largely rejected by GPS processing as the interfering signal is spread to a large bandwidth—or more accurately, to a line spectrum spread across a large bandwidth—thus making it appear as weak near-white noise. The spreading operation reduces the power of any remaining frequency line components by at least 18.3 dB (Parkinson & Spilker, 1996), with the average reduction closer to 30 dB. Thus, even if an interfering tone is found directly within a receiver's tracking bandwidth, there is at least 18.3 dB attenuation of such a signal.

GPS receivers indoors are subject to additional narrowband interference due to the various electronics often present. RF leakage from computers, wireless devices, etc., may fall within the GPS L1 band.

Wideband Interference and Thermal Noise

Interference over a wide portion of the bandwidth of interest is termed wideband interference. This may include man-made or other sources of interference, as well as thermal noise. This type of interference degrades GPS performance by burying the signal further below the ambient noise floor. Rejection of wideband effects is limited, particulary if the bandwidth of the interference source is comparable to the message bandwidth.

Sky and Ambient Noise

Parkinson & Spilker (1996) and Ray (2003) give thermal (sky) noise temperature, T_s, at the GPS L1 frequency as 100 K, corresponding to a noise density N_o of -208.6 dBW/Hz according to the relation

$$N_o = K_B \times T_s \tag{2.4}$$

where K_B is the Boltzman Constant with value $1.38 \times 10^{-23}\mathrm{W/(K \cdot Hz)}$. In fact, according to Pritchard (1997), at 1.5 GHz, sky noise temperature can range from approximately 2 K to 100 K, depending on elevation angle, but the larger value is taken as a standard herein, presumed to account for true sky noise as well as man-made diffuse interference. This noise is similar in nature to any wideband interference, but is a more fundamental source of noise and is well-modelled as AWGN. The level of sky noise varies with frequency and surroundings, however. It may be necessary to model different levels of noise depending on surroundings. An indoor environment likely has a different effective sky noise temperature due to blackbody radiation from the specific materials and devices (e.g. lights) surrounding a receiver.

2.2.2 Attenuation and Fading

Propagation by the various mechanisms—LOS, reflection, diffraction, scattering, and shadowing—results in power variations at a receiver. First, power on each of these paths is altered by fundamental characteristics of the propagation mechanism. This base attenuation is an effect observed on individual paths; shadowed signals experience an attenuation by the medium of transmission, and reflected and scattered signals experience absorption, polarization loss, and geometric spreading.

The second degradation is fading. Signals on the multiple propagation paths combine at any given point through vector addition of their respective voltages and phases. The result is constructive or destructive interference that causes signal amplitude changes as the individual component signals vary. These amplitude changes are referred to as fading.

Fading is an important characteristic of any RF channel because it defines the power levels necessary to ensure reception. In fact, a number of channel models have been developed specifically to describe fading. These will be discussed in more detail in Chapter 3.

2.2.3 Dispersion and Multipath

RF signals may undergo dispersion depending on the channel properties. A dispersive medium is one that induces different propagation effects depending on frequency (Orsak, 1997). For the GPS signal, the ionosphere is a dispersive medium which causes a varying amount of delay at each frequency (Lachapelle, 2002). Dispersion distorts received signal characteristics and can cause errors if the distortion causes intersymbol interference (ISI). A time-variant channel is also sometimes referred to as time-dispersive, in that it causes propagation effects that vary with time (Haykin, 2001).

In the GPS, the information transmitted is a timing signal with a period of approximately 977 ns. Any dispersion which significantly increases the width of this information symbol (chip) can potentially cause ISI which causes errors in receiving the signal. The multipath channel is therefore clearly dispersive as it induces effects that spread the received signal in time.

2.3 Doppler Effects Under Multipath Conditions

The Doppler effect induced by transmitter or receiver motion is well-known, as defined by the Doppler equation (Lachapelle, 2002),

$$\frac{f_r}{f_t} = \frac{1 - \frac{v}{c}\cos\theta}{\sqrt{1 - \frac{v^2}{c^2}}}, \tag{2.5}$$

where f_r and f_t are received and transmitted frequencies respectively, v is the velocity between transmitter and receiver at angle θ, and c is the speed of light. For static receivers, there is another potential source of Doppler effect under multipath conditions, induced by the changing length of NLOS paths. The level of this effect, referred to herein as *NLOS range-rate induced Doppler* (NRID), is derived below.

The observed Doppler is an indirect measure of the range rate of the satellite—the time rate of change of the satellite-receiver vector length. In static cases, the range rate is different on LOS paths as compared to NLOS paths. The magnitude of the Doppler effect can be calculated by determining the difference in range rate between the LOS and NLOS signals.

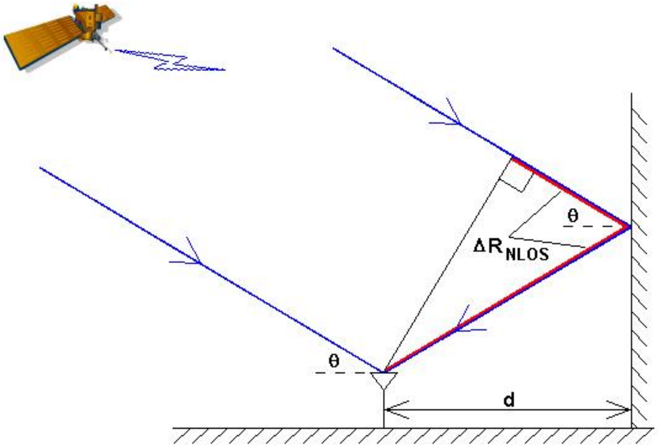

Figure 2.2: Excess Propagation Length on NLOS Paths

As seen in Figure 2.2, the excess path length ΔR_{NLOS} of a reflection depends on the distance d from reflector to receiver, measured as the shortest distance between the receiver and a plane tangent to the reflector, and the reflection angle θ, measured from the normal of the reflecting surface. Assuming the reflector and receiver are in close proximity relative to the satellite distance, the excess path length is defined as

$$\Delta R_{NLOS} = 2d\cos\theta. \tag{2.6}$$

As satellites move, the angle of incidence θ changes. If satellite motion is in a plane normal to the reflecting surface, the rate of change of θ can be up to approximately 0.5 degrees per minute for GPS satellites. Assuming d is constant, the rate of change of NLOS range error ΔR_{NLOS} is found as the derivative of Equation 2.6 with respect to time.

$$\frac{d\Delta R_{NLOS}}{dt} = -2d\sin\theta\frac{d\theta}{dt} \tag{2.7}$$

The value of $\frac{d}{dt}\Delta R_{NLOS}$ is now a function of three variables: d, θ, and $\frac{d\theta}{dt}$. The variables are not independent; they are correlated by the geometry of the environment. It would be desirable to develop a statistical distribution representing $\frac{d}{dt}\Delta R_{NLOS}$, but the underlying variables have yet to be characterized. Rather, some practical limits can be applied to the variable values to determine the range of NLOS range rates that may be encountered.

Equation 2.7 may increase without bound if d is unbounded. For the GPS satellite-to-ground channel, a reasonable bound for d will be taken as 1000 m. In general, most reflections are thought to originate closer to the receiver than 1000 m. The maximum value of $\frac{d\theta}{dt}$ is approximately 0.5°/minute, or 1.45×10^{-4} rad/s for the GPS satellite orbits. Given these maxima, allowing $\sin\theta$ to approach unity ($\theta = 90°$) gives a maximum reasonable value of NLOS range rate of 0.29 m/s, as calculated by Equation 2.7. Converting to a Doppler using the nominal L1 frequency of 1575.42 MHz gives an equivalent Doppler of 1.52 Hz.

The assumptions used to derive the 1.52 Hz limit for NRID are generous. Glancing reflections of almost 90° angle of incidence are rare on satellite-to-ground channels, and reflector distances of less than 1000 m are usually expected. Additionally, the distribution of the three defining parameters has not been characterized due to the complexity of indoor geometry. However, it seems reasonable to suggest that most reflections indoors would have d on the order of 20 m or less, although this could vary with building geometry. With that parameter, the maximum NRID is reduced to only 0.030 Hz, with average values somewhat lower due to distribution of the parameters. Strong, long-delay multipath components may still exist, of course, with larger NRID. The largest concern is the Doppler potentially caused by NLOS components from within the indoor environment itself, though.

2.4 GPS Availability Failures

2.4.1 Signal Obstructions

A complete blockage of a GPS signal obviously prevents reception of a direct signal by a receiver indoors. However, the definition of a blockage depends on the receiver attempting to measure the signal. Since receivers have different measurement thresholds, a complete blockage cannot be confirmed simply by the inability to detect a signal. Rather, it must be assumed that any medium introduces a finite attenuation, whether that value can be measured or not.

In many cases, the overall signal level at an indoor receiver is therefore defined by the level of obstruction affecting the direct signal. This may be a fairly constant level, or may vary with the propagation medium. It is this overall level of attenuation that is thought to prevent signal reception deep indoors, where any signal present would necessarily propagate through a number of different obstructive media.

2.4.2 Fading on GPS L1

In cases where relatively strong direct signals may be available, signal strength may still be degraded below tracking thresholds by fading. This is an effect of multipath interference with severity dependent on multipath conditions. Fading characteristics depend on several properties of the interfering component signals. The received signal's instantaneous power and the variations in power over time and space depend on wavelength, number of NLOS components, and the strength, phase, and polarization of those NLOS components.

The first property—wavelength—is intrinsic to the signal. The GPS L1 carrier wavelength is approximately 0.19 m. The strength, phase, and polarization of component signals in a multipath environment are a result of the environment and propagation mechanisms. The geometry, orientation, and electrical characteristics of the antenna's surroundings define the nature of the multipath components that contribute to fading.

Spatial Fading Characteristics at GPS L1

In a given environment, signal strength variations due to fading depend on the location within the environment. If all other elements of the system are stationary, the only source of relative phase change between LOS and NLOS signals is receiver movement within the environment. The changing phases result in changing interference patterns, and therefore signal strength.

The spatial characteristics of fading may be defined by average correlation distances, or the distance over which a strong or weak fade could be expected to hold for a moving receiver. Without knowledge of geometry, it can generally be thought that correlation distances are comparable to the wavelength of the signal of interest. For the GPS L1 signal, that is approximately 0.19 m. Correlation distances may be longer or shorter, however, depending on the geometry.

Different antenna types will observe different fading, even under identical multipath conditions, due to differing gain patterns and polarization. However, the short correlation distances of fades on the GPS L1 frequency should hold for any receiver.

Temporal Fading Characteristics at GPS L1

Signal strength changes over time depend on two factors: the changing multipath environment, and the receiver's motion within that environment.

Multipath in a static environment is expected to change slowly due to the GPS satellites' slow angular motion across the sky. However, rapid changes may also occur as the properties of NLOS sources shift suddenly. There is no clear evidence which sort of change dominates in an indoor environment, although Chapter 3 will discuss studies which indicate that slowly-changing conditions are supported by evidence.

The other source of temporal change, receiver motion, is best characterized by the velocity of the receiver. A quickly-moving receiver passes through high and low fades quickly in a static environment, giving short coherence times. Conversely, a slowly-moving receiver may experience longer fading coherence times.

2.5 GPS Accuracy Degradations

Absolute accuracy of GPS positioning is based on the accuracy of pseudoranges, the number of pseudoranges, and satellite constellation geometry. Bad geometry and limited signal availability are serious effects, but are well-understood in terms of their performance impact. Pseudorange measurement error induced by signal propagation effects is discussed in this section. Errors due to satellite position, atmospheric propagation, and clock errors are not discussed herein because these errors are common to both the outdoor and indoor channels, and have been extensively researched.

An indoor GPS receiver experiences pseudorange measurement errors if it fails to accurately estimate the time of arrival (TOA) of the LOS signal, generally due to the following factors:

1. Inaccurate estimate due to measurement noise
2. Distortion of the LOS correlation peak due to NLOS combination
3. Complete blockage of LOS signal, leading to acquisition of long-delay multipath signals or cross-correlation peaks

The third of these effects is not discussed in this thesis; long-delay multipath and cross-correlation are specifically avoided in the data analysis by focusing on reference LOS arrival times and designing measurement thresholds above cross-correlation levels. The nature and level of the remaining two effects are discussed separately here, but they always act in tandem on any received signal.

2.5.1 Measurement Error due to Noise

Due to fading and attenuation, indoor signals typically have lower signal-to-noise ratio (SNR) than under open-sky conditions. Equivalently, this can be seen as an increase in random noise and interference. Accurate measurement of a signal's TOA is hindered by the added noise with the level of degradation being receiver-dependent. Two factors affect accurate measurement: First, the C/A code correlation peak is distorted by the addition of noise regardless of the peak measurement technique used. Second, the code phase discriminators commonly used in GPS receivers have varying performance in the presence of noise.

A noise-affected correlation peak is shown in Figure 2.3. Note that the actual peak of the received function is moved away from the true LOS arrival time by the addition of noise, and that estimates of the TOA using two different discriminators

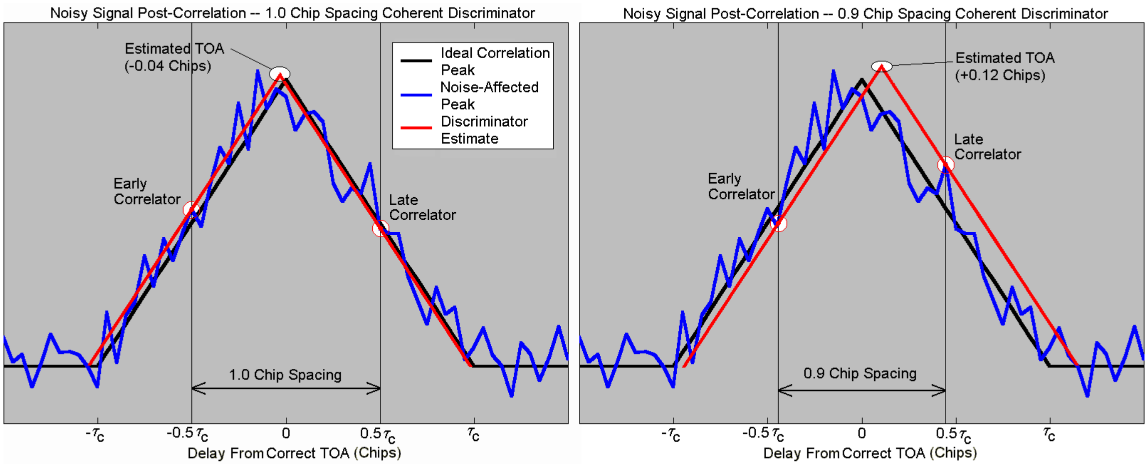

Figure 2.3: Noise-Distorted C/A Code Peaks with Coherent Discriminators

give significantly different values. This is only a sample of the error induced by noise, but the dependence on discriminator factors is clear.

The one-sigma value of noise-induced tracking error for a given noise level and discriminator can be determined as follows (Parkinson & Spilker, 1996):

$$\sigma_{tDLL} = \sqrt{\frac{4F_1 d^2 B_n}{C/N_o}\left(2(1-d) + \frac{4F_2 d}{TC/N_o}\right)}, \tag{2.8}$$

where σ_{tDLL} is one-sigma tracking error in chips, F_1 and F_2 are dimensionless discriminator factors, d is early-late correlator spacing, B_n is tracking loop noise bandwidth, C/N_o is carrier-to-noise density ratio, and T is predetection integration time.

The only receiver-independent factor in Equation 2.8 is carrier-to-noise density ratio. F_1, F_2, and d are discriminator parameters, B is a property of the DLL loop filter, and T is determined in various ways, but is always limited by receiver design and abilities. Therefore, the only characteristic representative of true propagation effects is C/N_o.

2.5.2 Measurement Error due to Multipath

Ignoring noise now for a moment, accurate pseudorange estimation is based on the assumption that the peak of the received C/A code correlation function can be found at the correct chip offset. CDMA PRN codes such as those used by GPS, namely the Gold codes (Parkinson & Spilker, 1996), are designed to have a level of multipath immunity inherent, but this is not a complete immunity. TOA measurement error is unlimited in cases where only an NLOS signal is received. Even in cases with LOS signals present, the correlation peak is easily distorted in the presence of multipath in one of two general ways:

1. Weak multipath arrivals within short delay of LOS TOA;
   Absolute correlation peak remains at correct TOA
2. Strong multipath arrivals with any delay relative to LOS TOA;
   Peak shifts later than correct TOA

The descriptors “strong” and “weak” refer to the relative strength of multipath after it has been received by an antenna. Most GPS antennas have a level of multipath immunity inherent. Low-elevation signals are typically ground reflections, and GPS antennas have gain patterns designed to reject these signals. Additionally, NLOS signals may have opposite polarization to LOS signals, depending on the nature of the reflection, and GPS antennas are designed to reject left-hand circularly polarized signals. With this in mind, the following discussion applies to multipath effects after antenna effects have been considered, and with the assumption that at least a weak LOS signal is available.

Correlation Peak Distortion

Correlation peak distortion introduced by multipath with known power, delay, and phase may be calculated as a linear sum of the peaks of all the components. In the presence of an LOS signal and $(n-1)$ NLOS components, the correlation peak has the form

$$R'_{C/A}(\tau) = \sum_{k=0}^{n} \alpha_k R_{C/A}(\tau - \tau_{dk}) cos(\phi_k - \phi_0), \tag{2.9}$$

where $R'_{C/A}$ is the multipath-distorted correlation peak, $R_{C/A}(\tau)$ is the autocorrelation function of the PRN of interest, α_k, τ_{dk}, and ϕ_k are the amplitude, delay, and phase of multipath component k, and ϕ_0 is the phase of the LOS signal (Ray, 2003). As mentioned, strong and weak multipath have different overall effects on the peak.

Weak Multipath If the LOS signal is received with greater power than any delayed multipath components, or combinations thereof, the maximum point of the correlation function remains at the correct TOA. The shape of the peak within some delay (depending on the multipath delays) of the LOS peak is, however, distorted. This is illustrated in Figure 2.4, showing a composite correlation function that is a sum of scaled, delayed functions that add linearly. Each component function has the general form of the C/A code autocorrelation peak, being triangular with a width of 2 chips. Clearly if the LOS signal is strong relative to received multipath, the maximum point of the composite correlation function must remain at the correct TOA.

Strong Multipath The peak of the correlation function is displaced in cases where the LOS signal is highly attenuated and/or strong multipath components are present. In the extreme, no LOS component exists and a specular reflection may be considered the first arrival by the receiver. The displacement of the peak follows directly from the weak multipath case, with the strong multipath simply taking the place of a strong LOS signal. The strong multipath need not be a single arrival, but may be composed of multiple arrivals constructively interfering. Figure 2.5 illustrates a case of two weaker multipath components combining to overcome the LOS signal and shift the peak of the correlation function.

Coherent Versus Non-Coherent Peak Distortion Figures 2.4 and 2.5 demonstrated correlation function effects observed in the energy domain, that is either the inphase or quadrature branch of a receiver. The summation of LOS and NLOS components in those cases is a linear operation. If non-coherent summation is used, additional complications are introduced.

First, if power is received on both inphase and quadrature channels without phase lock, a multipath component may appear weak in the inphase branch, but strong in the quadrature branch or vice versa, depending on the phase of the demodulating carrier. In such a case, the correlation peak position in the two branches may be different. However, if the absolute power of the LOS signal is stronger than NLOS components, the non-coherent addition of the I and Q branches results in a peak at the correct TOA, regardless of the peak location in either branch.

The second complication is that squaring a correlation function with multipath distortion results in a non-linear composite of the various components. The peak remains at the correct location, but the shape of the total peak is distorted non-linearly. This is a very significant problem for calculating the level of multipath error in the presence of a large number of multipath arrivals.

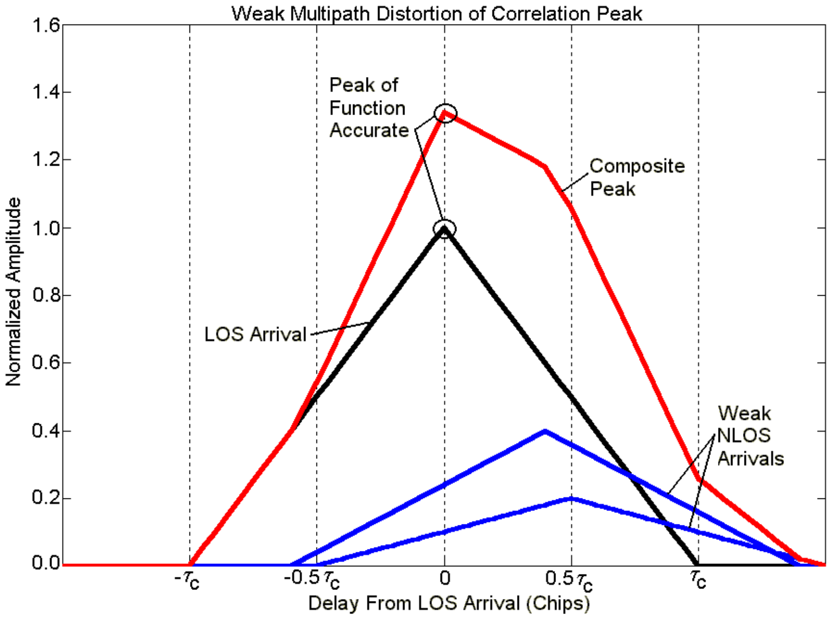

Figure 2.4: Correlation Peak Distortion by Weak Multipath

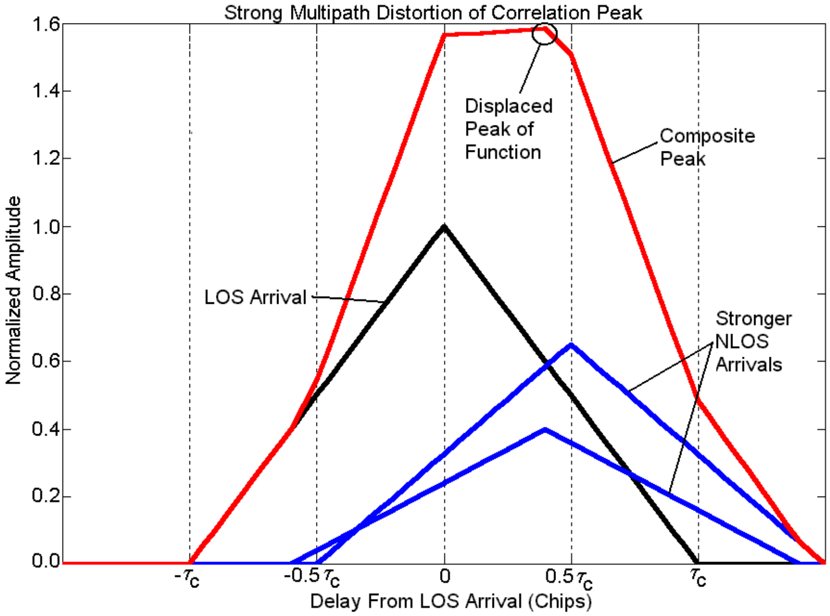

Figure 2.5: Correlation Peak Distortion by Strong Multipath

Quantifying Measurement Error from Multipath

A peak undergoing multipath distortion according to Equation 2.9 causes measurement errors that can be quantified if all component signals are known. A given discriminator relies on the assumption that the correlators measure values of the ideal autocorrelation function. The error induced by this peak distortion may therefore be determined by examining the effect of the distorted values of the early, prompt, and late correlators on the discriminator function of interest. Effects of the distortion on a correlator with some delay T_d are easily calculated. For example, the inphase early correlator, with delay $-T_d$ relative to the presumed TOA, has value

$$IE = \sum_{k=0}^{n} \alpha_k R_{C/A}(\tau - t_{dk} + T_d) \cos(\phi_k - \phi_0). \tag{2.10}$$

For standard discriminators, multipath susceptibility is measured with the multipath error envelope—the maximum possible level of error caused by some multipath with varying delay and a given relative power (Ray, 2003). For example, the ideal error envelopes of coherent discriminators with 1.0 chip and 0.2 chip E-L spacing in the presence of a single multipath with signal-to-multipath ratio (SMR) of 6 dB are given in Figure 2.6.

The error envelope characterization is only a simple representation of multipath susceptibility, however. The envelope is a representation of multipath error in the presence of only one NLOS component, assuming a LOS component is also received. Increasing the number of NLOS components introduces more variables, namely different permutations of delay and power, which may expand the error envelope. Also, any discriminator is susceptible to strong multipath, as discussed above. Due to the expected complexity of indoor environments, possible strong multipath, and the

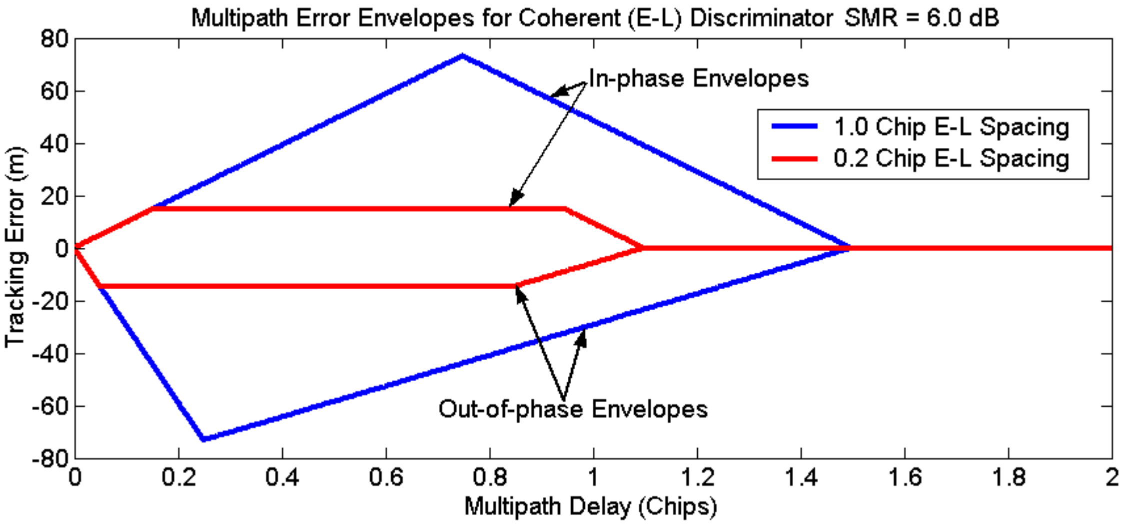

Figure 2.6: Example Multipath Error Envelopes of Coherent Discriminator

variety of discriminator techniques used, analytical methods of calculating multipath effects are not suggested for modelling. Rather, the nature of the peak distortion due to multipath must be examined.

Chapter 3

Indoor GPS Performance and Modelling

This chapter addresses the current state-of-the-art in indoor GPS positioning and related channel modelling research. It begins by discussing channel modelling techniques commonly used in communications systems today, and reviews several specific models discussing the potential for application in indoor GPS channel modelling. Following that, GPS-indoor performance and modelling studies conducted over the last several years are reviewed. The significant advances and limitations of that research are discussed. These limitations will be revisited in Chapter 4 to determine the best approach for novel indoor channel modelling research.

3.1 Channel Modelling Overview

3.1.1 Purpose

A channel is simply a system that relates some output to a known input. In the case of a wireless RF signal, the propagation channel is the system that transforms the transmitted (input) signal into the received (output) signal. The transformation is essentially some combination of the basic mechanisms discussed in Chapter 2. A channel model is a mathematical abstraction of the actual channel, usually intended to allow for the development and test of technologies that will function in the presence of non-ideal propagation. Thus, it can be said that a channel model is simply a means to predict and replicate errors that occur in real channels.

3.1.2 Modelling Approaches

Linear Time-Invariant (LTI) Channel Models

A common description for a channel is the impulse response $h(t)$ combined with additive noise $n(t)$ (Haykin, 2001). This is illustrated in Figure 3.1 with input and output represented by $x(t)$ and $y(t)$ respectively. The Fourier transform of the impulse response is known as the frequency response, or sometimes the transfer function, $H(j\omega)$. In fact, either the impulse response or frequency response is a complete description of a noiseless linear time-invariant (LTI) channel.

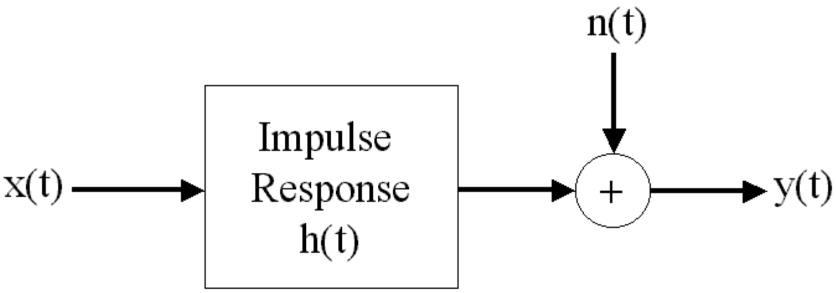

Figure 3.1: LTI Channel Impulse Response Representation

Real-world RF propagation channels are extremely complex and difficult to completely characterize, however. These channels are often time-varying, and therefore cannot be completely described by a linear time-invariant representation. Rather than attempt to completely describe a non-LTI channel with more complex models, RF engineers may choose to model only a subset of channel properties which are important to the application of interest. Such models are discussed below.

Large-Scale Fading Models

Power attenuation over large distances in a wireless RF system is described by large-scale fading models. Most of these models are intended for land-based communications systems in which propagation takes place near the earth's surface and power loss typically exceeds free-space loss. Some models referenced in the literature (Rappaport et al., 1997) include the log-distance path loss model, the Okumura model, the Hata model, and the Walfish and Bertoni model. The basis for these models—that propagation occurs near Earth's surface—is not particularly relevant to the satellite-to-ground GPS, for which propagation generally does not take place near the earth. Large-scale path loss in such systems as GPS is due to free-space loss, and is essentially constant. This type of large-scale model is therefore not under consideration for modelling the GPS-indoor channel.

A set of models for the indoor channel may also be considered large-scale because they model path loss throughout an indoor environment. Rappaport et al. (1997) discusses the Saleh and SIRCIM models. Saleh models the indoor-to-indoor channel assuming NLOS conditions, showing the effects of walls and office furniture on large-scale path loss (tens of metres). The SIRCIM model is a computerized model combining statistical distributions with geometric calculation. It is described as an "elaborate" model, that shows some success in modelling path loss in factory type environments. A GPS-indoor model will likely need to account for geometric effects like the SIRCIM model, but this is more closely related to geometric analytic models to be discussed later.

Small-Scale Fading Models

A set of models designed to account for true fading—that is, fading caused by multipath interference over short distances—are referred to as small-scale fading models (Rappaport et al., 1997). Pure fading models are often used to determine fade margins that will ensure reliable operation of communications systems. These are generally statistical (probabilistic) models based on certain theoretical assumptions about propagation. Since small-scale fading is also an important trait to model for GPS-indoor operation, some of the existing models will be reviewed in Section 3.2 with analysis of their potential for use in GPS propagation modelling. The statistical fading models reviewed in this thesis are designed for channels that are non-selective. The categorization of channels as selective or non-selective is discussed below.

Selective and Non-Selective Fading Channels The possible dependence of fading on frequency and time gives rise to a categorization of fading channels as frequency-selective, time-selective, or non-selective.

A frequency-selective channel "is characterized by a transfer function that varies in a more or less random fashion with frequency." (Smith, 1997). Amplitude and phase of the various frequency components are therefore more or less random at the output of the channel, giving rise to fading characteristics that depend largely on frequency. The frequency selective channel is characterized by a small *coherence bandwidth*, B_C, which is the band over which fading behaviour is highly correlated. Coherence bandwidth is inversely related to delay spread, to be discussed shortly.

A time-selective channel has a time-variant impulse response, leading to fading behaviour that depends on time. The parameter to describe time-selectivity is *co-*

herence time, T_C, or its inverse, Doppler spread.

According to Smith (1997), a channel cannot be simultaneously time- and frequency-selective, because this implies that transmitted bandwidth is both smaller (time-selective) and larger (frequency-selective) than the channel coherence bandwidth. A "simultaneous" measure of time- and frequency-selectivity is irrelevant, however, since time-selectivity occurs over some period. Therefore, effects of time- and frequency-selectivity may be observed on a single channel over time, such as is the case with a time-varying impulse response with large delay spread.

The only other possibility is a non-selective channel, which has fading behaviour that depends on neither time nor frequency. Thus, any signal transmitted over a non-selective channel has time-invariant fading behaviour, assuming its bandwidth is smaller than the channel's coherence bandwidth. A non-selective channel is also referred to as time-flat/frequency-flat, or simply flat-flat.

Delay and Doppler Spread Models

The parameters related to fading selectivity lead to delay and Doppler spread characteristics that describe a channel's time- and frequency-dispersion characteristics. Such characteristics are necessary to evaluate possible distortions of the signal or examine possible inter-symbol interference (ISI). Delay spread can be given as a single statistical delay parameter describing the expected temporal dispersion of a signal transmitted by a channel, or as a profile defining the range of delay spread characteristics. Doppler spread is the analogous description in the frequency domain.

As mentioned, delay and Doppler spread parameters are inversely related to coherence bandwidth and coherence time. A channel is often considered 'narrowband' if the transmitted bandwidth is less than the coherence bandwidth, and 'wideband' otherwise. The narrowband/wideband categorization must be taken into account when considering the possible modelling techniques suitable for the spread-spectrum GPS signal.

Analytic/Deterministic Models

Statistical modelling approaches are suitable for estimating fade margins and determining likely error rates in a wide variety of environments. These models cannot accurately predict signal behaviour in a given environment, however, without first determining appropriate parameters through testing. Statistical models are also weak in predicting instantaneous behaviour, instead focusing on long-term probabilities.

Analytic or deterministic models make use of well-known signal propagation behaviour to model a specific propagation channel. Generally, these models rely on simplified approximations of the physical propagation mechanisms (the cost of simplicity varies depending on the application). They are particularly suited to simulator applications where repeatability is necessary. Some analytic modelling approaches are reviewed in Section 3.4.

3.2 Small-Scale Fading Models

The two most commonly known statistical representations of fading are the Rician and Rayleigh probability density functions. Other small-scale models intended to overcome some of the limitations of Rician and Rayleigh distributions include Loo's distribution and a number of models combining Loo's, Rician, and Rayleigh distributions. The relevant models are described and discussed in this section.

3.2.1 Rician and Rayleigh Fading

The Rician distribution models a flat-flat channel for the situation in which a clear, strong LOS signal is available in the presence of some weaker, randomly-distributed multipath components. The envelope of a signal undergoing Rician fading is defined by Equation 3.1 below, where z is the amplitude of the envelope ($z \geq 0$).

$$f_{Rice}(z) = 2Kze^{-K(z^2+1)}I_o(2Kz) \tag{3.1}$$

$f_{Rice}(z)$ is the probability of signal level z (in volts), K is the 'Rice factor,' representing a ratio of LOS to multipath power, and I_o the modified Bessel function of the 0^{th} order (Goldhirsh & Vogel, 1998; Papoulis & Pillai, 2002). The Rayleigh distribution is a special case of the Rician distribution for which there is no LOS component present. Its envelope is defined as follows, again for the case $z \geq 0$:

$$f_{Rayleigh}(z) = 2\overline{K}ze^{-\overline{K}z^2}. \tag{3.2}$$

$\overline{K}$ in this case is similar to the Rician K. Although LOS power does not exist in this case, $\overline{K}$ represents a ratio of the reference power level—were there any LOS power—to the scattered multipath power. Thus, higher $\overline{K}$ yields a lower probability envelope.

Examples of the Rician and Rayleigh distributions are given in Figure 3.2. Note that as the Rician K and Rayleigh $\overline{K}$ decrease towards zero, they degenerate to identical distributions.

Applicability to Indoor GPS

The Rician model—and by extension, the Rayleigh model—are based on some key assumptions. For both models, a large number of NLOS components are presumed

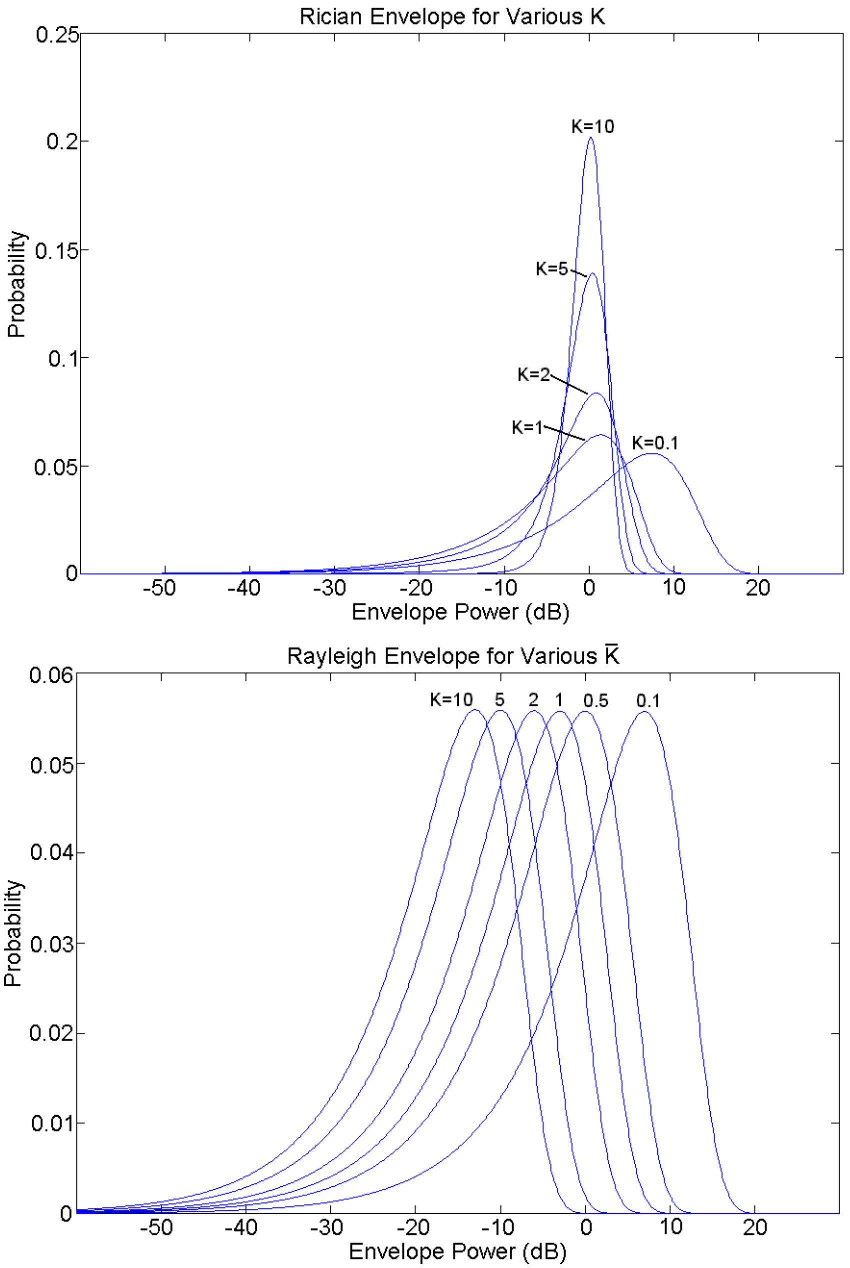

Figure 3.2: Rician and Rayleigh Power Probability Envelopes

to be received, with unknown amplitudes and random phase. By the central limit theorem (Walpole et al., 1998), these NLOS components are thought to combine to form a composite multipath contribution with normally distributed amplitude with some constant variance σ, and uniformly-distributed phase. This assumption should be valid for the spread-spectrum GPS signal regardless of frequency-selectivity as long as multiple NLOS components do exist and NLOS conditions are unchanging. If, on the other hand, indoor signals are composed of very few signal components, the conclusion reached via the central limit theorem is not valid. Additionally, if multipath conditions change quickly due to user or satellite motion, the variance of the normal distribution may vary significantly and quickly, thus requiring a more dynamic model than the standard Rician or Rayleigh models.

The second key assumption behind the Rician model is that LOS signal power is strong and constant. By the fundamental definition of LOS propagation, this assumption should be invalid for indoor GPS because LOS signals are rare. There may be some 'direct' signals visible, but these generally propagate through some building materials and should thus be considered shadowed. The distribution of shadowed signals is discussed next.

3.2.2 Lognormal Power Model for Shadowed Signals

Signals that propagate through some attenuating medium typically have a lognormal power distribution (Goldhirsh & Vogel, 1998). Again, the lognormal model is valid for a flat-flat channel, which is not necessarily a property of the GPS-indoor channel.

If the variable z represents signal amplitude, the lognormal distribution is given by

$$f_{Lognormal}(z) = \frac{8.686}{z\sqrt{2\pi}\sigma} e^{-\frac{(20\log(z)-\mu)^2}{2\sigma^2}}, \tag{3.3}$$

where σ and μ represent the standard deviation and mean of $20\log(z)$ respectively. The constant 8.686 is a scale factor resulting from the standard definition of a lognormal distribution being based on the natural logarithm, rather than the base-10 logarithm used in signal processing. While $20\log(z)$ has mean and standard deviation μ and σ, these are not, in fact, the corresponding parameters for the lognormal distribution itself. The parameters σ and μ obviously depend on the medium of propagation and possibly the motion of transmitter and receiver. Examples of the lognormal distribution with various parameters is presented in Figure 3.3. The rest of the models described herein include use of the lognormal distribution for shadowed signals.

It is unclear whether or not building materials cause the same power distribution as roadside tree shadowing, for which the lognormal distribution was originally intended. Building materials are more uniform than trees, presumably resulting in less variation. That simple difference could, of course, be accounted for by appropriate use of the standard deviation term σ in the lognormal distribution. For the GPS-indoor channel in particular, measurements have not confirmed the nature of the distribution induced by building materials because shadowing effects are indistinguishible from multipath fading, using existing receiver technology and standard GPS antennas. A study by Klukas et al. (2004) has examined effects of building materials at GPS frequencies, but drew no conclusions about the statistical distribution of shadowing.

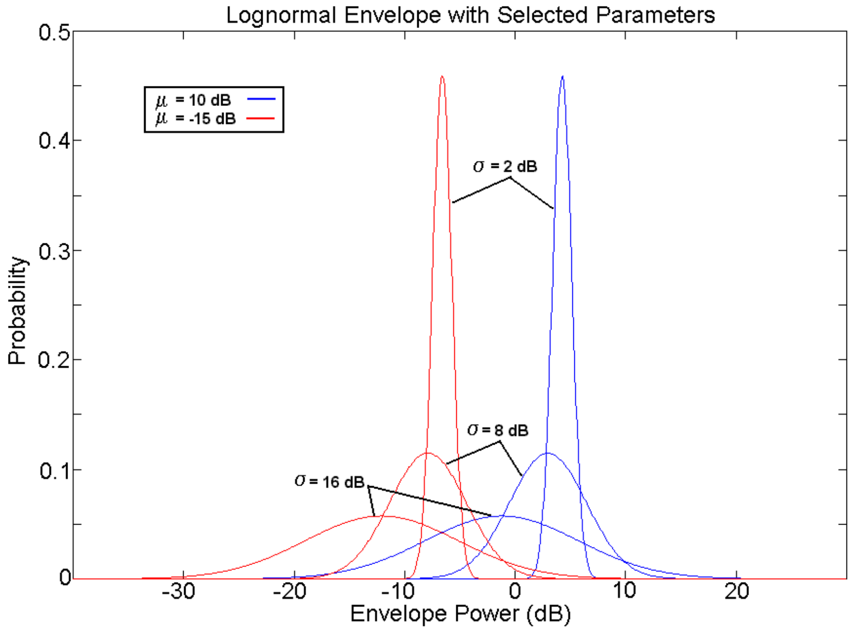

Figure 3.3: Lognormal Signal Power Envelope

3.2.3 Loo's Distribution

Loo (1985) has developed a statistical distribution combining the multipath characteristic of Rayleigh fading with the lognormal power distribution of the shadowed LOS signal. For a given LOS power, Loo's distribution has the conditional probability envelope of the Rician distribution. The overall Loo distribution is arrived at by integrating this conditional Rician probability over the lognormal distribution of the LOS (shadowed) signal.

$$f_{Loo}(v) = \frac{\sqrt{2}v\overline{K}}{\sigma\sqrt{\pi}} \int_0^\infty \frac{8.686}{z} exp\Big[- \frac{(20\log(z) - \mu)^2}{2\sigma^2} - \overline{K}(v^2 + z^2)\Big] I_o(2\overline{K}vz)dz \quad (3.4)$$

The PDF is expressed in terms of the probability of voltage v. The previously-used variable z is a component of the conditional Rician probability and the lognormal distribution, and is evaluated in the integration operation. The combined PDF requires three parameters: $\overline{K}$ representing the power of the random multipath components, and σ and μ representing the standard deviation and mean of the lognormally-distributed shadowed power.

As with the Rayleigh and Rician distribution, Loo's distribution is a description of the fading observed over a certain time or during movement within a fading environment. In fact, the parameter values described in Loo (1985) are based on certain classes of environments, with the shadowing defined as "frequent" or "infrequent" and "light" or "heavy." These terms represent an average fade state, and must be determined empirically for a specific environment.

Considering the application of Loo's PDF for indoor GPS fading, some improvement over the Rician model is possible because Loo accounts for a shadowed signal. However, the assumption of a constant Rayleigh distribution for multipath components remains, and is questionable due to the nature of the indoor environment. As mentioned previously, it is believed that the mean and variance of the multipath power envelope will change significantly indoors over time.

3.2.4 Combined Distributions

Karasawa Three-State Fade Model

Karasawa et al. (1995) (as cited in Goldhirsh & Vogel, 1998) developed a model consisting of a weighted distribution of Rayleigh, Rician, and Loo's functions. The form of the model is

$$f_{Karasawa}(v) = Cf_{Rice}(v) + Sf_{Loo}(v) + Bf_{Rayleigh}(v), \tag{3.5}$$

where C, S, and B are weighting factors representing the probability of encountering clear, shadowed, and blocked propagation states. The model is most applicable to a receiver in motion within a varied environment, where it is likely to encounter clear, shadowed, and blocked propagation states within a given time. The weighting approach may also be applicable to stationary receivers in the case where the transmitter is in motion, as with static GPS receivers.

This three-state model ostensibly accounts for various propagation conditions, ranging from blocked to open-sky, which would seem advantageous for the heterogeneous surroundings encountered by indoor GPS. A single environment might have surrounding media that cause blockages, shadowing, or allow LOS propagation. However, the signal from a single satellite likely pierces a more constant propagation medium over time, which is best represented as *either* clear, shadowed, or blocked, but not a weighted combination of all three. Evaluation of this model for modelling GPS fading is discussed in Section 3.6.

Urban Three-State Fade Model (UTSFM)

Akturan & Vogel (1997) modified the Karasawa model specifically for Urban conditions; instead of representing the blocked state with the Rayleigh distribution, Loo's distribution was used. The resultant PDF is

$$f_{UTSFM}(v) = C(\alpha) f_{Rice}(v) + S(\alpha) f_{Loo}(v) + B(\alpha) f_{Loo}(v), \tag{3.6}$$

where the weight parameters are now dependent on satellite elevation angle α. The replacement of Rayleigh with Loo's distribution is based on the premise that in urban environments, a blocked signal is likely to still undergo significant specular reflection in addition to lower-power scattering and diffraction. The likely result is one or two dominant reflections combining with lower-power multipath, which is better described by Loo's distribution.

Theoretically, the ability of this three-state model to represent GPS fading is similar to that of the Karasawa model. Questions remain about the method of representing fading with a weighted combination of several states. An examination of this model for GPS indoor modelling is also presented in Section 3.6.

3.2.5 State Transition Models

Lutz et al. (1991) describe an approach in which it is assumed that during unshadowed conditions, the signal has a Rician distribution, while during shadowed conditions it has a Rayleigh distribution with the mean scattered power being lognormally distributed. The lognormal modulation of the Rayleigh power follows from the assumption that in shadowed conditions, the LOS signal is scattered in such a way as to cause Rayleigh fading, but the scattered power still varies lognormally depending on the propagation medium.

The overall probability distribution of Lutz et al. (1991) is developed by determining a probability of each state—shadowed and unshadowed—and the nature of the transitions between each state, which are modelled as a Markov model by the authors. While this model depends on transitions between good and bad states, the modelling of those transitions actually results in a single 'shadowing factor' S that describes the transitions. The probability distribution is given as

$$f_{Lutz}(P) = (1-S)f_{Rice}(P) + S\int_0^\infty f_{Rayleigh}(P|\overline{K})f_{\overline{K}}(\overline{K})d\overline{K}, \tag{3.7}$$

where $f_{Lutz}(P)$ is probability of received power P, S is the shadowing factor, $\overline{K}$ is the

Rayleigh average power constant, and $f_{\overline{K}}(\overline{K})$ represents the probability distribution of the Rayleigh constant, which is modelled as lognormally distributed with mean μ and standard deviation σ.

Other similar models making use of the Rayleigh and lognormal distributions have been developed. All of these models show good correspondence to measured data after using empirical regression to develop the parameters. The parameters are in no way generic, however, nor do they offer a means to model GPS in specific environments without first gathering empirical data to set parameters.

Although state transition models are based on a more realistic categorization of signals as being either shadowed or unshadowed, rather than some average value, the use of a statistical model to define the transition between states results in the same problem: the model remains a purely statistical estimate with parameters that vary with every environment. The approach is promising for indoor GPS, though, because the inhomogeneity of building materials might be conducive to using a state transition approach.

3.3 Path Delay Spread Models

Specific models of delay and Doppler spread are limited in the literature. The parameters are commonly used to describe individual channels, but no general delay or Doppler parameters are available for certain classes of environment. The generality of the existing parameters is demonstrated in Haykin (2001) which states that in a mobile radio environment, *typical* delay and Doppler spreads are 20 μs and 40-80 Hz. A pair of studies relevant to indoor GPS have been reviewed, showing the development of delay spread parameters with a high-bandwidth channel sounder. These studies do not provide a basis on which to conclude that indoor GPS delay spread is comparable, however.

Pérez-Fontan et al. (2004) conducted a measurement campaign to characterize the power delay profile (PDP) of the satellite-to-indoor channel, simulating satellite signals from an aerial platform. The measurements were conducted in only one building, which limits the generality of the results. Root mean square (RMS) delay spreads on the order of 25-200 ns were measured, corresponding to delays of approximately 8-70 m. The distinction between indoor and outdoor reflections is unclear from those delay spreads. A similar measurement campaign by Steingass & Lehner (2003) outdoors yielded delay spread statistics for the outdoor channel in urban, suburban, and rural environments. No general model was developed, but a strong dependence on elevation angle was shown for the delay spread.

The most pertinent information to be drawn from these studies may be related to the observed indoor delay spreads of 25-200 ns. These spreads correspond to fading coherence bandwidths of between 5 MHz and 40 MHz, which is larger than the bandwidth of the majority of GPS C/A code power. It might therefore be reasonable to treat the GPS signal as narrowband, operating in a flat-flat channel over short periods.

3.4 Analytic/Deterministic Models

3.4.1 Geometric Scattering from Single Source

If an obstruction causing NLOS propagation is presumed to scatter a received signal isotropically, the resultant effects can be calculated using a geometric model and vector addition of LOS and NLOS arrivals. Goldhirsh & Vogel (1998) describes a model based on this approach. In addition to geometric parameters, the situation description must include methods to determine LOS and NLOS field strength and antenna characteristics; the model describes the scattering source by its radar cross-section and computes field strength on that basis. Simulation using this model shows a good correspondence with field fading data under kinematic conditions, which demonstrates the value of geometric models in creating time-series of data under simple, easily-definable circumstances.

3.4.2 Geometric Reflection

A specular reflection may also be simulated geometrically. The nature of the reflection may be determined by computing a surface's reflectivity from electromagnetic characteristics, or using other means as necessary. An example of this type of model is implemented in the Spirent GSS 6560 GNSS simulator (Lachapelle et al., 2004). Reflections are generated based on simulated semi-infinite surfaces within the simulator, with power determined by the user rather than material properties. The Spirent implementation accounts for transmitter motion by geometrically varying the path length of reflections. The use of a variable-delay geometric reflection model has been shown to be able to accurately re-create the stochastic nature of fading effects observed in field multipath environments. These re-creations were obtained while using only three to five NLOS sources.

Pérez-Fontan et al. (2004) demonstrated a similar geometric model for generation of reflections and diffractions. While not accounting for transmitter motion, that model used the electromagnetic properties of simulated surfaces to determine strength and phase of NLOS signals. Reasonable power delay profiles were simulated using that approach, indicating that a geometric approach is valid. The analytic calculation of signal propagation is apparently computationally intensive, however. Pérez-Fontan et al. (2004) simulated a larger number of rays than Lachapelle et al. (2004) in order to replicate field measurements, with the total number of NLOS rays in the range of 10 to 20.

3.4.3 3-D Geometric Scattering from Multiple Sources

An analysis by Vishakantaiah & Vogel (1989) uses a randomly-distributed set of scatterers to compute signal effects geometrically. While the scattering sources are not deterministically placed, the geometric solution to the problem provides insight into the nature of multipath. Sources were distributed throughout a wide range from the receiver, from 30 m to 2000 m, and it was found that only scattering sources within close proximity of the receiver had a significant effect on fading. This analysis also draws conclusions about the nature of multipath effects based on antenna gain pattern. It is clear that antenna filtering of NLOS signals reduces their impact, and must be accounted for when determining appropriate GPS-indoor models.

3.4.4 Advantages and Drawbacks of Analytical Techniques

Analytical techniques require a tradeoff between accuracy and complexity. For example, the single-scatterer model is geometrically simple and accurate, but uses an approximation of isotropic scattering. Goldhirsh & Vogel (1998) note that this approximation is not supported by field data—scattering is more likely to be non-isotropic. To achieve greater accuracy, a more realistic description of the scatterer is required, which increases complexity.

One must determine what aspects of the channel are most important, and therefore deserving of the most complexity. The models of Spirent and Pérez-Fontan et al. (2004) use a similar geometric approach to modelling multipath, but with different points of complexity. Spirent's model uses complex techniques to model satellite motion, whereas that of Pérez-Fontan et al. focuses more effort on realistically simulating surface properties and number of multipath components. As a result, Spirent's model realistically simulates the time-domain variation of fading, whereas that of Pérez-Fontan et al. provides an accurate delay spread.

3.5 Studies of Indoor GPS Performance

The availability and performance of GPS indoors have been researched extensively with standard, high-sensitivity, and assisted GPS receivers. It is impossible to pinpoint when GPS was first tested indoors, although it was likely during initial system development. Some more recent studies of GPS indoor performance are reviewed here.

Stand-Alone GPS Performance

High-sensitivity receiver development since 2000 (e.g. Chansarkar & Garin, 2000) has yielded receivers capable of tracking signal levels well below nominal levels in real-time. MacGougan et al. (2002) demonstrated the operation of the SiRF high-sensitivity receiver indoors, most notably demonstrating an ability to track multiple satellites to levels at least 9 to 10 dB below that which standard receivers can track, and 25 dB below nominal levels. In a garage environment, availability of a solution with the SiRF receiver was greater than 99%, with horizontal position-domain errors near 10 m RMS observed. Further similar tests by Lachapelle et al. (2004) in a North American residence show similar solution availability of greater than 98% with position errors of approximately 17 m RMS horizontally. These tests have not demonstrated the ability to acquire signals indoors using high-sensitivity techniques. Outdoor acquisition was required in these tests to initialize the receivers before indoor operation. In each of these tests, the indoor signals experienced fades exceeding the HS receiver's ability to track.

While results as discussed above are promising, difficulties in signal acquisition indoors and tracking failures commonly observed make stand-alone HSGPS an unreliable solution for indoor positioning. Thus, in recent years, more focus has been on testing augmentations and hybrid systems that provide better performance.

Augmentations for Indoor GPS

Assisted GPS (A-GPS) is seen as one solution to providing E-911 service to wireless handsets. Thus, many studies have examined performance improvements possible by providing assistance such as navigation data and timing information. The current focus of these studies is on optimizing A-GPS algorithms, using laboratory tests as in Karunanayake et al. (2004). A-GPS offers improvements over stand-alone methods and may provide sufficient accuracy for E-911 under certain conditions. These tests are not comprehensive, however; the demonstrated performance is not available in all indoor environments. A-GPS cannot prevent performance degradation by short-delay multipath, which is thought to be common indoors.

As further example of the integration of GPS with other technologies, Petovello et al. (2003) examined the utility of using HSGPS to provide velocity information to indoor positioning technologies based on inertial navigation systems (INS). In these types of systems, overall GPS performance indoors is not assessed, but rather the ability to derive useful information from GPS to aid in navigation is examined. As would be expected, the benefits of using GPS to assist in hybrid systems depend on the accuracy of GPS measurements. These are, of course, still degraded by indoor environments and in need of further characterization.

A more radical approach to augmenting GPS positioning indoors is to use GPS repeaters or pseudolites (pseudo-satellites), as in Caratori et al. (2003). By providing a set of strong GPS-like signals indoors, a modified GPS receiver with standard sensitivity levels may compute its position within the well-defined indoor environment. This method still suffers from multipath, however, which is a major problem with any GPS implementation. Therefore, while the suggested method overcomes the availability problem, characterization of multipath characteristics indoors is clearly required for accurate positioning.

Combatting Problems of Weak Signal Measurement

Problems introduced by using high-sensitivity techniques for indoor positioning include excessive time-to-first-fix (TTFF) and incorrect tracking due to cross-correlation. For stand-alone HSGPS, Mattos (2003) has suggested methods of acquisition to prevent cross-correlation acquisitions. These methods offer greater reliability and availability for indoor GPS operation, but do not address the fact that indoor signals are generally NLOS. Weak signal tracking is only an effective indoor technique if the correct signal is being tracked. A-GPS is seen as the best means to overcome long TTFF, and it also provides some immunity from acquisition of long-delay multipath peaks or cross-correlations. As mentioned, however, A-GPS is still susceptible to short-delay multipath.

Lachapelle et al. (2003b) address reliability of the position solution obtained indoors. Methods such as height-fixing, statistical testing of residuals, and fault detection and exclusion (FDE) are discussed, with experimental results indicating that FDE methods are still in need of development for indoor use. Partly because of low signal levels, signals necessary to position determination may be excluded as erroneous when, in fact, only a low SNR causes the error.

Overall, accuracy and availability of GPS indoors remains insufficient to meet the requirements of critical location applications. In many cases, position accuracy does meet requirements, but availability and reliability are questionable. A-GPS and other augmentations can improve availability and accuracy, but the fundamental issue of propagation errors—primarily NLOS effects—remains an unmodelled source of error indoors.

3.6 Studies of the GPS-Indoor Channel

Very few researchers have attempted to develop channel models specifically for the GPS-indoor channel. A few studies are reviewed in this section in which researchers have attempted to use live GPS signals in real environments to characterize the propagation channel. The results show little significant progress when compared to the channel models already discussed.

An early test of HS indoor GPS measurement capabilities is described in Peterson et al. (1997), in which the authors used strong reference data to augment indoor processing capabilities and conduct coherent integrations of up to 160 ms. The goal of the tests was purely to measure GPS signals indoors and test the ability to measure pseudorange. The reported results show extremely heavy signal power reduction, in excess of 60 dB from the LOS signal. Insufficient data are analyzed to actually characterize indoor fading, but the existence of deep fades and their impact on indoor signals was observed. Spread of the correlation function in the time domain was thought to indicate likely multipath spread in this study. Interestingly, it is not clear how fades in excess of 60 dB could have been measured in this study using coherent integration times of only 160 ms. This question will be further explored in Chapter 8 after the results of this thesis research are presented.

Ma et al. (2001) and Klukas et al. (2003) have evaluated the Karasawa model and Urban Three-State Fade Model (UTSFM) as applied to GPS signals in difficult environments using standard and high-sensitivity GPS receivers. Data sets gathered in several environments over a period of hours, including indoors, were effectively matched to several theoretical fading distributions based on the UTSFM, comprising

Rician and Loo's PDFs. The results of these studies seem to have been taken by later researchers to indicate that the individual propagation paths, whether they be LOS, reflections, diffractions, or diffuse scatterings, each behave according to one of these distributions. Specifically, that LOS signals experience Rician fading, that reflected or scattered signals experience Rayleigh fading, and that shadowed signals experience Loo's fading. In fact, this conclusion seems to be the basis for the application of Rayleigh and Rician models in the Spirent GSS 6560 simulator.

The valid conclusion to be drawn from the study by Ma et al. (2001). is that over a long period of time, the distribution of signal fading appears to have Rayleigh, Rician, and Loo's components dependent on the nature of the presumed LOS propagation path. One cannot draw conclusions about the nature of the individual signal components that combine to create that distribution. Therefore, simulation of individual rays with such distributions is not a valid approach for replicating realistic propagation conditions.

Haddrell & Pratt (2001) examined indoor GPS signal strength varying with time. Signal fades with coherence times on the order of hundreds of seconds and levels between 15 dB and 40 dB were observed using a Parthus Technologies high-sensitivity receiver. The authors concluded that these characteristics for a stationary receiver correspond to the model of multiple NLOS paths combining at the receiver with slowly-changing phase relationships. The overall distribution of the fading levels was not examined, so no conclusions are drawn relating to the Karasawa examination by Ma et al. (2001) or the UTSFM examination by Klukas et al. (2003). By characterizing the nature of fading as a result of slowly-changing NLOS arrivals, the study supports an investigation intent on identifying sources of multipath and characterizing them independently.

Lachapelle et al. (2003a, 2003b, and 2004) all include some analysis of indoor propagation channels through pierce-point analysis. These studies group received GPS signals according to their presumed line-of-sight pierce point within the environment, for example through a window or a concrete wall. The statistical distributions of fading and pseudorange error (thought to represent NLOS propagation error), as measured by a SiRF HS receiver, are examined and correlated with respect to the surroundings. The pierce-point method has been successful in identifying environmental characteristics affecting signal properties. The environments of (2003a) and (2003b) show a strong correlation between the location of the signal and the pseudorange error and fading. In the residential location, an inverse correlation between signal strength and satellite elevation was observed which conflicts with what would be expected. While no new models were developed by these researchers, the analysis method shows potential to relate fading to environmental characteristics. These studies also clearly show the need to develop models based on specific environments found indoors, rather than generic elevation-based models which may be appropriate for outdoor use.

Aiga et al. (2003) have similarly attempted to correlate GPS received signal levels with the nature of the indoor environment. They note the strong correspondence between GPS signal strength and both the distance from and angle towards an external wall containing a window. While this is not a surprising result, that signal strength degrades further into buildings, it supports the method of pierce-point analysis.

Klukas et al. (2004) have used GPS pseudolites to characterize the transmission characteristics of various materials on the GPS L1 signal. Since most signals received indoors propagate through some building material, this study is particularly relevant. Materials ranging from plywood to Gyprock (wallboard) were examined in terms of transmission loss (attenuation) and induced pseudorange and carrier phase error. The range of effects is considerable, ranging from 0.5 dB for a double plywood wall to 23 dB for a 25 cm cinder block wall. The nature of reflections from each of these surfaces was not studied. The implied result of Ma et al. (2001) was that shadowed signals should have a fade distribution according to the Loo's PDF, over a long period of time. In this 2004 study, the attenuation measured does not exhibit much distribution over a short period, indicating a possible flaw in the application of the UTSFM to indoor propagation models as in the GSS 6560 simulator.

Based on the shortcomings of models and techniques used to date, the characteristics of a novel model are defined in the following chapter. An approach and methodology to develop this novel model are subsequently defined, leading into research results beginning in Chapter 5.

Chapter 4

Novel Model Development: Requirements, Objectives, and Approach

The major RF propagation mechanisms acting on the GPS-indoor channel have been reviewed in Chapter 2, and the two major causes of GPS ranging errors have been discussed. Chapter 3 reviewed studies of GPS performance in signal-degraded environments, and presented several models commonly used to model propagation conditions. While most models are based on theoretical propagation effects, their limited ability to model the effects that lead to GPS errors is a severe drawback.

This chapter identifies the requirements for a novel GPS indoor channel model that will overcome the limitations of existing models and discusses methods to develop such a model. Section 4.1 lists the desired characteristics of a suitable model. With these requirements in mind, the overall objectives of this thesis research are then discussed. The research approach has been partly defined by the model requirements and partly by the availability of unique raw data related to a cooperative research effort undertaken in the PLAN (Position, Location, and Navigation) group at the University of Calgary. The available data sets are introduced in Section 4.3. Specific objectives for analysis of the raw data are defined in Section 4.4.

4.1 Model Performance Requirements

To be used for GPS receiver evaluation or other related tasks, a GPS-indoor channel model must have several key characteristics. A suitable model must

- accurately model effects that contribute to GPS performance degradations,
- have a basis on physical reality of signal propagation,
- be repeatable, and
- be configurable based on desired test conditions.

Existing models do not meet some or all of these requirements. Statistical fading models fail to account for temporal characteristics of fading, and do not account for NLOS range errors at all. These models also need to have their parameters determined in advance based on environmental characteristics, which are typically complex and inhomogeneous. Statistical modelling of NLOS path errors is limited to the delay spread function, which can be used to stochastically describe delays of multipath propagation. The delay spread is, however, expected to vary widely within an environment depending on satellite elevation and azimuth. No single model can be expected to accurately describe NLOS path errors at all points.

Analytical models based on geometry have not proven to have a strong theoretical foundation on actual propagation behaviour and have difficulty modelling fading and range errors simultaneously. It seems, therefore, that a novel model must be tailored specifically to account for GPS error effects, based on observed behaviour in real environments. With this in mind, objectives are defined that will allow the measurement of these signal effects and the resultant GPS performance degradations.

4.2 Model Development Objectives and Approach

It is not the intent of this research to develop a comprehensive model immediately suitable for use in testing receivers in simulated indoor environments. Rather, two general objectives are targeted. The primary objective is to empirically examine the GPS-indoor channel to develop a more thorough understanding of the effects causing receiver performance degradation and malfunction. It is hoped that this knowledge will suggest novel modelling techniques that will meet the requirements discussed above. A second objective is to develop a novel way of approaching the modelling task that is more suitable for the unique demands of simulating GPS signals than existing communications channel models. Regardless of the outcomes of the analyses of the specific data, the techniques used may be evaluated and improvements suggested for future modelling.

4.2.1 Channel Measurement Approach

The remainder of this thesis focuses on detailed analyses of GPS signals gathered indoors to extract and characterize channel characteristics. This section briefly describes the analysis approach, based on a post-mission analysis of raw indoor data.

A limiting factor in previous indoor channel analyses has been the use of off-the-shelf HS receivers to measure signal characteristics. These receivers are designed to work in real-time, which limits the ability to provide external assistance. A-GPS is designed to overcome this limitation, but is still under development and test. Another limitation is that real-time receivers only output processed data, rather than raw signals. The measurements are therefore dependent on the specific correlation techniques or RF characteristics of the receiver. This research was intended to find better channel measurement techniques starting with raw data.

The measurement approach decided upon was determined by the timely availability of a pair of data sets provided by Nokia Mobile Telephones Ltd. as part of a cooperative research effort with the PLAN group. These data sets consist of raw, high-bandwidth, indoor GPS L1 data along with simultaneous reference data. This thesis focuses primarily on analysis of these raw GPS L1 signals gathered in a pair of indoor environments.

All analysis is based on static receivers. While it is understood that most applications of personal positioning will use handheld receivers, propagation effects can be analyzed with static receivers with techniques that are not available for analyzing dynamic receivers yet. It is believed that the use of static techniques can be largely extended to dynamic applications. The possible extensions are discussed as part of the evaluation of results. It should be noted that this analysis approach is somewhat similar to the approach described in Peterson et al. (1997), in which the authors used long integrations to measure weak indoor signals. There are substantial differences in technique, however, and results. A comparison of results will follow in Chapter 8.

4.3 Overview of Nokia Data Sets

The data sets provided by Nokia were gathered with Nokia's proprietary *Digitizer* technology, which is an implementation of an RF front end and analog-to-digital converter. The Digitizer employs direct downconversion to a pseudo-baseband frequency of -1875 Hz. The important parameters of the Digitizer are given in Table 4.1.

Digitizer Parameters	
Front End Bandwidth	$\geq$ 10 MHz
Direct Downconversion IF	-1875 Hz
Baseband Bandwidth	4 MHz
Sampling Rate	9.885 MHz
Sampling Precision	3-bit (I & Q)

Table 4.1: Digitizer Data Parameters

The data were gathered in two indoor environments, referred to as 'Tube' and 'Terraario,' on Nokia's premises in Tampere, Finland. Data gathering took place on September 10, 2003 (11:53–12:00 UTC) using a stationary HP 58504A GPS antenna. The Terraario rover location is on the top floor of a four-storey building, several metres from any external walls. The Tube rover location is within an elevated walkway between two buildings, and is enclosed primarily with glass walls on the north and south sides (see Figures 4.1–4.4). For each test, a receiver located on the roof of the building gathered synchronous data for reference purposes. The location of the reference antenna has been provided with estimated accuracy of about 5 m in the WGS-84 datum. Although precise rover antenna positions are not known, Nokia has confirmed that the reference-rover antenna separation is less than approximately 30 m. An external Datum ET-6000 ovenized crystal oscillator was used as a frequency reference for both reference and rover Digitizers. During the tests, 11 SVs were visible above the horizon. Details of these SVs are listed in Table 4.2 for both data sets. Figures 4.2 and 4.3 show locations of the 11 SVs visible with reference to the building. The line for each satellite in these figures represents the cosine of the elevation angle to emphasize the horizontal geometry of the GPS constellation.

	Tube Data Set			Terraario Data Set		
PRN	Elev. (°)	Azi. (°)	Doppler (Hz)	Elev. (°)	Azi. (°)	Doppler (Hz)
3	17.8	32.2	-1034	17.2	30.3	-1224
8	77.1	126.0	-265	75.7	117.9	-443
10	43.7	230.5	-2106	41.9	228.4	-2276
15	8.7	4.8	2141	9.7	3.1	1970
17	13.0	275.8	-2484	11.5	274.2	-2614
21	17.1	320.8	-448	16.7	318.7	-650
26	30.2	291.9	3121	32.5	291.9	3015
27	48.7	88.4	-1959	46.6	88.3	-2070
28	36.2	172.2	2997	38.5	171.5	2882
29	51.6	283.2	2043	53.7	282.1	1912
31	23.1	67.1	1096	23.7	64.8	889

Table 4.2: SVs Visible Above Horizon

Figure 4.1: Tube Walkway from Exterior and Interior

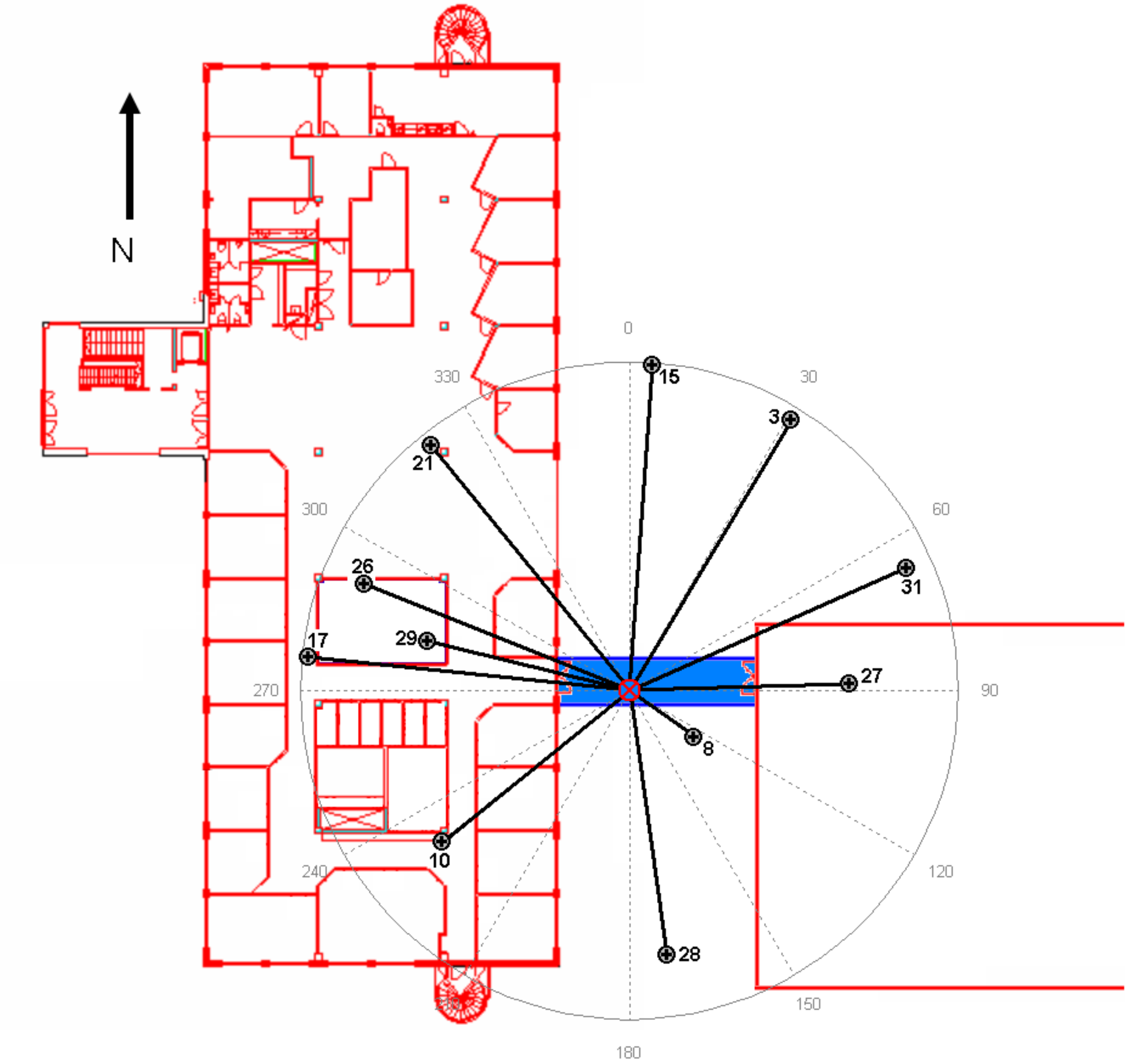

Figure 4.2: Schematic View of Tube Environment Showing SVs Visible

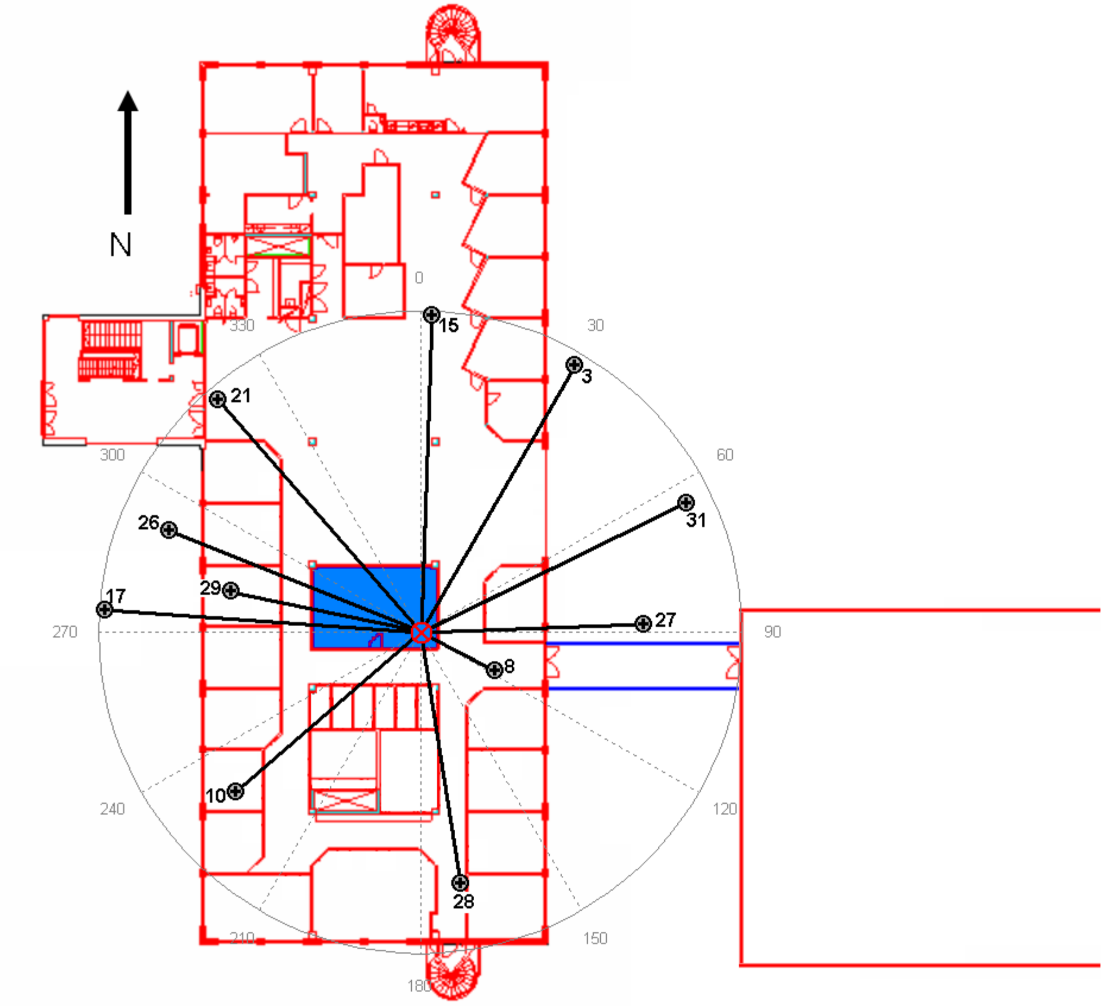

Figure 4.3: Schematic View of Terraario Environment Showing SVs Visible

Figure 4.4: Terraario Rover Location

4.4 Specific Goals for Data Analysis

Working with high-bandwidth raw GPS data in a post-processing mode offers the possibility to implement extreme high-sensitivity receiver techniques to measure signals not previously detectable. In addition, the elimination of real-time processing constraints allows for high-resolution analysis of signal characteristics that would be impossible in real-time. Some specific research objectives to take advantage of the available data have been set accordingly.

4.4.1 Objective 1: High-Sensitivity Implementation

The preliminary goal in working with Nokia's data sets was implementation of software tools capable of receiving signals in both indoor environments and generating the necessary outputs for further analyses. No specific target was set for the level of high-sensitivity gain to be achieved. Rather, the goal was to explore the limits of high-sensitivity processing with these specific data sets.

4.4.2 Objective 2: Visualization of Signals in High Resolution

Analysis of the spread-spectrum GPS signal must take place almost exclusively after de-spreading. The signal is too weak to analyze independently before it is separated from other signals sharing the channel and increased above the noise floor by the correlation process. Thus, visualization of signals post-correlation was identified as the best option for extracting channel characteristics. To facilitate accurate channel measurements, the goal of measuring the GPS correlation function in the highest possible resolution in both code- and frequency-offset domains was set.

4.4.3 Objective 3: Identification of Multipath Signals and Effects

The implementation of a high-resolution, high-sensitivity GPS correlation tool offers potential for several analyses designed to identify and characterize multipath signals and other GPS-indoor channel effects.

3a: Multipath Separation in Doppler Frequency

High-sensitivity processing reduces the bandwidth of a signal component, whether LOS or NLOS, to a fraction of a hertz. This is seen as a potential tool for separating LOS and NLOS signals which may have different Doppler shifts due to channel effects.

3b: Multipath Resolution in Code Offset

The GPS C/A code correlation function has known characteristics under LOS and multipath conditions. High-resolution measurement of the correlation function is seen as a possible means to identify and separate LOS and NLOS components that combine to form a distorted correlation peak.

3c: Characterization of Multipath Impact on Performance

The large-scale effects of multipath, as discussed in Chapter 2, include GPS position accuracy degradation due to NLOS ranging errors and low SNR, and reduction in availability. A characterization of these effects is required in combination with the small-scale analysis of multipath characteristics to accurately generate a model that links propagation effects to GPS performance.

4.4.4 Objective 4: Novel Model Synthesis

Although limited data are to be analyzed, channel characteristics should be identified that are suitable for incorporation into a comprehensive channel model based on analysis results. The novel raw data analysis approach will allow comparison of observed characteristics with models already in existence, and suggestions for improvements that should be incorporated in a future, comprehensive model.

Chapter 5

High-Sensitivity Implementation and Test

5.1 HSGPS Theory and Challenges

5.1.1 HSGPS Overview

Standard Processing Limits

The processing gain used to extract a GPS signal from noise and co-channel interference is a function of the initial signal bandwidth and of the integration time used to correlate the signal. If the raw signal is represented at baseband, the theoretical processing gain achieved with a certain integration length is

$$G = 2BT, \tag{5.1}$$

if B is the single-sided bandwidth of the signal at baseband and T is integration time. A more detailed derivation of processing gain is presented in Appendix A (Section A.3). Under normal circumstances, integration time is limited by two factors.

The first limitation of standard processing is the 20 ms period of the navigation message. The modulo-2 addition of the GPS C/A code with navigation data introduces a 180° phase shift in the BPSK-modulated carrier at every navigation bit transition which effectively negates the positive effect of signal integration across a bit transition. While a bit transition does not occur *every* 20 ms, there is potential for a transition. Thus, coherent integrations longer than 20 ms are not possible without *a priori* knowledge of navigation data.

The second limitation is due to frequency mismatch between the local receiver clock and the incoming signal. Frequency error attenuates received power according to a sinc-squared function (Parkinson & Spilker, 1996), to be henceforth referred to as a 'power rolloff function.' The first null width of the power rolloff function is determined by the integration time T according to the relation $f_{null} = 1/T$. This relation essentially describes the fact that a 1 Hz error over 1 second causes a 2π phase change between the incoming signal and the local carrier, negating all energy received. A frequency error of approximately 44% of the Doppler power rolloff function first null width attenuates the signal by 3 dB, as illustrated in Figure 5.1.

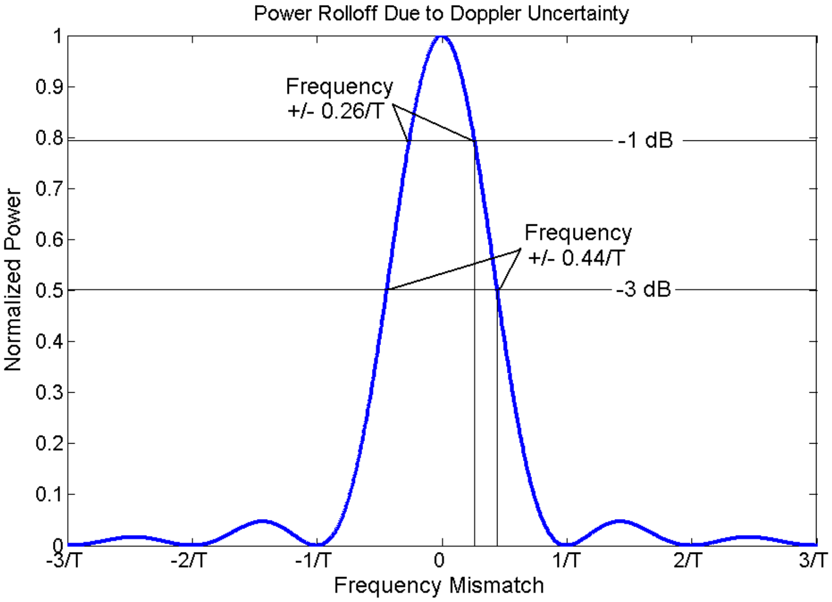

Figure 5.1: Power Attenuation due to Doppler Error

HSGPS Techniques

High-sensitivity GPS is any technique that increases processing gain beyond standard levels to receive and measure weak signals. Typical HSGPS implementations rely on non-coherent integration over periods longer than 20 ms. Non-coherent integration does not require precise Doppler modelling, as coherent integration times do not exceed 20 ms.

Recent developments of assisted-GPS have enabled the use of long coherent integrations by providing the navigation message, timing information, almanac, and approximate position through alternate communications channels. This assistance allows integrations longer than 20 ms, and may improve receiver timing to lessen the limitations caused by Doppler mismatch. Current timing accuracy is sufficient to increase integration times to hundreds of milliseconds, but not yet past 1 second and beyond (Karunanayake et al., 2004).

Challenges of Long Coherent Integration

The primary limitation on coherent integration time remains Doppler frequency mismatch. When not tracking—as during acquisition or within a coherent integration—the frequency prediction must be accurate to better than 2 Hz as integration periods increase past 500 ms in order to receive the signal. Extreme integration times of several seconds require correspondingly higher accuracy. For example, a long integration of 10 s demands prediction accuracy to better than 0.1 Hz over the course of 10 s. Ideally, the prediction should be accurate to a small fraction of the power rolloff width to receive a significant amount of power during an acquisition.

Doppler prediction of this accuracy is impossible in dynamic applications (without predictable dynamics, at least), and requires precise position, timing, and ephemeris information even in static conditions. External factors may also make prediction of that accuracy level impossible, as discussed in the following section.

5.1.2 Limiting Factors of High-Sensitivity Processing Gain

Long integration may not provide the gain theoretically predicted by Equation 5.1 for a number of reasons, most of which relate to frequency errors in the demodulation process. We categorize these errors into signal and receiver classes. Signal errors are those which would exist regardless of the receiver technology or algorithms. Receiver errors are those related to the equipment or algorithms used.

Signal Errors:

- Signal phase noise (e.g. due to ionospheric scintillation)
- Power fluctuations during integration (fading)
- Unmodelled Doppler sources (multipath, random atmospheric effects, high-frequency orbital errors)

Receiver/Algorithm Errors:

- Receiver clock stability / noise
- Additional noise sources (e.g. quantization noise)
- Receiver bandwidth
- Limited Doppler model accuracy
- Power measurement technique errors

The signal errors listed include two sources of frequency error and the effects of fading. These cannot be easily mitigated with receiver techniques. Receiver and algorithm errors include two sources of frequency error, the receiver clock and the Doppler model accuracy, and two effects relating to measured power. These sources will be addressed as appropriate when discussing results of power measurement tests in Section 5.5.

5.2 Software Implementation

The software developed for this thesis is primarily designed for high-sensitivity signal acquisition and measurement. To measure the code offset and Doppler frequency of each signal present in the raw data, the software is designed to use a configurable search window allowing arbitrary code and frequency resolution. This allows characterization of signal distortion caused by multipath or other propagation effects. Doppler prediction techniques, discussed in Section 5.4, are used to enable extremely long integrations.

5.2.1 Architecture

The primary analysis software is implemented in C++, using various support files in ASCII text and the PLAN group's internal matrix (.mtx) format. The software, currently referred to as *CorrTool*, is a stand-alone program created partly with the use of routines and methods developed for GNSS_SoftRx™, the PLAN group's software GPS receiver (Ma et al., 2004). Outputs are files representing power and energy in a user-configurable code-frequency search space. The input-output operational

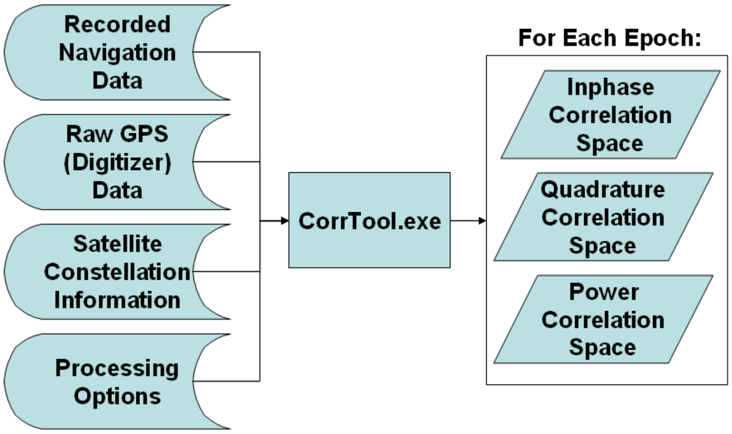

Figure 5.2: Correlation Tool Top Level Execution

diagram is given in Figure 5.2.

The high-sensitivity correlation operation is done sample-by-sample, updating code phase, Doppler, and navigation data as necessary for each sample. This yields slow operation but allows for the precise Doppler and code phase tracking necessary for HSGPS. The techniques used to extract navigation data from the reference signals are discussed in Section 5.3. The Doppler modelling technique used by the program is discussed in Section 5.4. A detailed description of CorrTool program flow and descriptions of the input files are given in Appendix B.

5.2.2 Outputs and Post-Processing Analysis

CorrTool outputs 3 matrix files for each code-frequency search space at each epoch: two files contain energy data for each of the inphase and quadrature channels, and the third is total power from both channels. An example of inphase energy output is shown in Figure 5.3, in which a slightly distorted triangular correlation peak is clearly seen. The code and frequency resolution and domain of the search space may be arbitrarily determined to optimize the analysis for whatever purpose is necessary. The sample shown here is from a 20 ms integration of the reference data (PRN 15) and has resolution of 0.1 chips and 5 Hz.

Post-processing analysis, required to obtain most results presented in Chapter 6, is conducted with Matlab and supplementary C++ programs including a least-squares position calculation tool developed specifically for operation with CorrTool output. The least-squares tool is based directly on GNSS_SoftRx™(Ma et al., 2004).

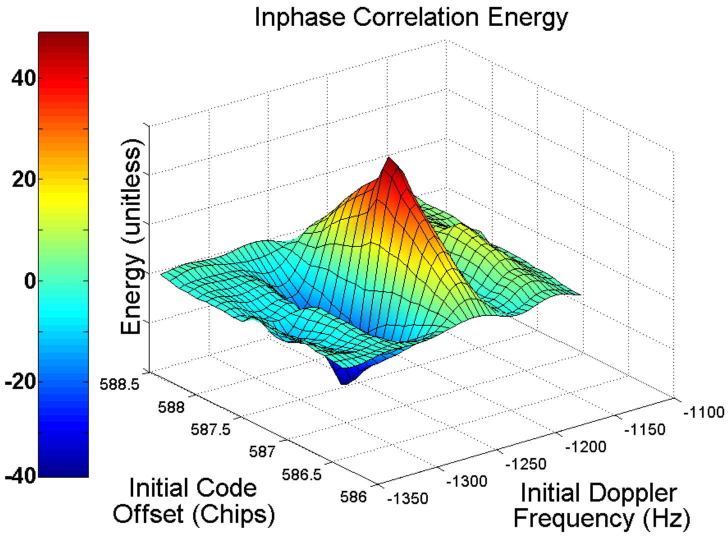

Figure 5.3: Visualization of Correlation Output (Inphase)

5.3 Reference Navigation Data Extraction

5.3.1 Implementation

Navigation data has been extracted from reference data sets by conducting 1 ms integrations synchronized with the C/A code word throughout the data set and detecting 180° phase changes. CorrTool uses a frequency-locked loop for carrier removal, rather than a phase-locked loop. This technique causes an inherent phase change between 1 ms integration periods, as the local oscillator phase resets to zero at the beginning of each millisecond. However, these phase changes were compensated for before detecting bit transitions. The SNR of each PRN was sufficient to conduct this procedure with only 1 ms integration, without introducing any significant errors.

With this short integration time, small errors in Doppler frequency are not critical to measuring phase in each millisecond. Since this procedure was done before the precise Doppler modelling described in Section 5.4, only a linear Doppler model was used to account for C/A code Doppler to maintain code word synchronization. After extracting the entire navigation message, subframe synchronization was performed by searching for the 8-bit message preamble (or its inverse) at intervals of 300 bits (ICD200C, 2000). The GPS time of week was decoded at the beginning of each subframe, providing an absolute time stamp for the data set and partially verifying the navigation bit stream.

The decoded navigation data was confirmed correct with two tests. The successful decoding of a reasonable GPS time of week (TOW) and other information in the first word of each subframe confirmed that portion of the data. The full navigation data stream was then tested and confirmed correct by an alternate method discussed in Appendix C.

5.3.2 Applicability to Rover Data Sets

Since navigation data was measured and extracted using the reference data, the resultant bit stream is synchronized with a specific epoch, rather than a specific chip or code word. As such, the use of navigation data wipe during signal analysis may tend to bias code offset measurements towards the reference TOA; at any code offset different than the reference TOA, power is slightly attenuated because navigation transitions are not synchronous with code word boundaries. This is particularly the case with multipath arrivals, whose code offset may be delayed by a significant fraction of a chip. However, time delays on the order of 2 chips or less introduce bit synchronization errors that are only a tiny fraction of the total integration time, assuming a relatively long integration. The resultant bias towards the reference TOA is negligible compared with effects of noise, interference, and multipath.

5.4 Doppler Modelling

This section analyzes the sources of Doppler effect encountered by an indoor receiver, their magnitude, and possible techniques to model these effects for prediction to enable long coherent integrations.

The major sources of Doppler for a *stationary* receiver include satellite orbital motion, satellite clock drift, atmospheric propagation effects, receiver clock drift, and multipath. Each of these potential sources is discussed below in Sections 5.4.1–5.4.4.

5.4.1 Satellite-Induced Doppler Effects

Satellite orbital motion alone can cause up to about 5 kHz of Doppler shift depending on satellite dynamics relative to the receiver location. In addition, satellite clock drift affects the frequency actually emitted from the GPS satellite, causing a further apparent Doppler effect. Clearly, these effects must be defined and predicted to implement long coherent integrations.

The best continuous, deterministic description of SV dynamics is the broadcast ephemeris consisting of 16 geometric and timing parameters. In addition, satellite clock corrections are provided in the broadcast navigation data. Calculations using the broadcast ephemeris give satellite-user range accuracy to within about 2.1 m (Parkinson & Spilker, 1996), allowing the calculation of Doppler as observed at a given location.

While the position accuracy figure mentioned above is reported in the literature, the accuracy of instantaneous radial velocity of SVs derived from the ephemeris is not widely reported. To test the accuracy, a comparison of Dopplers derived from broadcast ephemerides and clock parameters and post-mission precise ephemerides (available from IGS (2005)) has been conducted for the period during which the Nokia data sets were gathered. The mean Doppler error over a set of 30-second intervals for each SV is presented in Table 5.1.

The 30 second average does not represent Doppler perturbations within the 30 second periods, but the observed values are taken as representative. The maximum error is 0.0114 Hz, calculated for PRN 26 during the latter half of the Tube data set. The RMS error and standard deviation of all values in the table are 0.0062 Hz and 0.0031 Hz. Given these statistics, it is unlikely that the actual Doppler varied from that predicted using the broadcast ephemeris by more than 0.0114 Hz, and rarely by more than 0.0100 Hz. For most PRNs, the change in Doppler error between the first and second halves of the data sets—a 30 second interval—is less than 0.0050 Hz. It seems reasonable to assume that higher-frequency effects which would impact coherent integration would be at a lower level. Long coherent integrations upwards of 10 s should be largely unaffected, although the error in Doppler due to a broadcast

Broadcast Ephemeris Doppler Error (Hz)

	Approx Tube Epoch		Approx Terraario Epoch	
PRN	GPS Time 301980-302910	GPS Time 302910-302940	GPS Time 302280-302310	GPS Time 302310-302340
3	0.0048	0.0052	0.0020	0.0076
8	0.0022	-0.0001	-0.0004	0.0029
10	-0.0035	-0.0035	-0.0092	-0.0100
15	0.0087	0.0061	0.0089	0.0100
17	0.0046	0.0057	0.0044	0.0104
21	-0.0015	-0.0006	0.0063	0.0036
26	0.0091	0.0114	0.0095	0.0055
27	-0.0024	-0.0083	0.0010	-0.0051
28	-0.0036	-0.0045	-0.0056	-0.0041
29	-0.0010	-0.0043	-0.0035	-0.0031
31	0.0073	0.0094	0.0058	0.0086

Table 5.1: Broadcast Ephemeris Doppler Prediction Error

ephemeris inaccuracy may show up as a fairly constant bias of up to 0.01 Hz.

The full ephemeris and clock corrections were not used in the HS software because of limitations in processing speed. Rather, a simpler approximation was chosen using a polynomial approximation fitted to the broadcast ephemeris. The derivation of that approximation is discussed below.

An approximation of an SV orbit with high Doppler dynamics is examined in Appendix D to determine the necessary polynomial degree to adequately represent the Doppler. Calculations show Doppler dynamics that are significant to the second order over 60 s, and to the third order over a period of minutes. The major results of that analysis are presented in Figure 5.4 and in Tables 5.2 and 5.3.

Based on those conclusions, it is determined that only a second-order polynomial is necessary to adequately represent Doppler dynamics over a few tens of seconds.

Additionally, the dynamics of the clock drift are nearly linear over a few tens of seconds, and can therefore be adequately incorporated into a second-order model. The form of the polynomial is given as

$$\dot{\phi}(t) = \dot{\phi}(0) + \ddot{\phi}_o t + \frac{1}{2} J_d t^2 \tag{5.2}$$

where $\dot{\phi}(t)$ is the Doppler at time t, $\ddot{\phi}_o$ is the initial Doppler drift, due to the acceleration acting on the satellite-observer vector, and J_d is the constant Doppler jerk, due to the jerk acting on the satellite-observer vector. While 'jerk' is normally associated with a third-order effect, it appears as a second-order parameter in Equation 5.2 because the Doppler itself is a derivative of position.

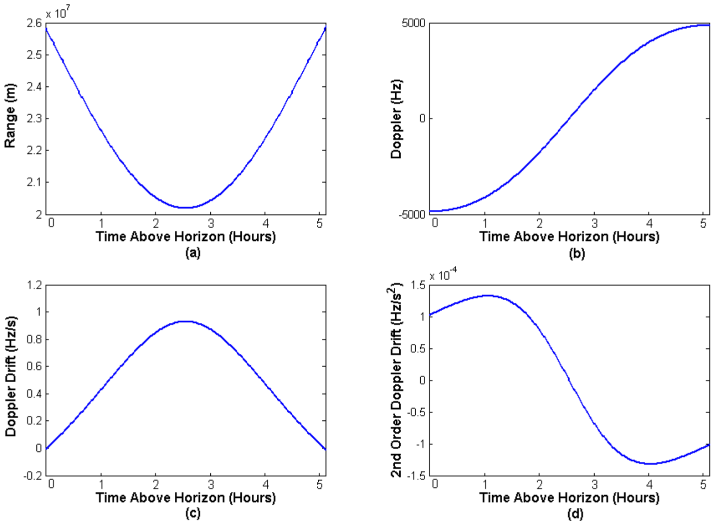

Figure 5.4: SV Range, Doppler, and Drift under worst case orbit

Doppler Parameter Estimation and Evaluation

The model parameters are determined by fitting a second-order polynomial to a number of points derived directly from the broadcast ephemeris and clock data. For

T(s)	2nd Order Doppler Contribution (Hz)
0.1	6.5×10^{-7}
1.0	6.5×10^{-5}
5.0	1.625×10^{-3}
10.0	6.5×10^{-3}
50.0	1.625×10^{-1}

Table 5.2: Maximum Contribution of 2nd-Order Effects

T (s)	3rd Order Doppler Contribution (Hz)	T (min)	3rd Order Doppler Contribution (Hz)
1.0	7.17×10^{-9}	1.0	1.55×10^{-3}
5.0	8.96×10^{-7}	2.0	1.24×10^{-2}
10.0	7.17×10^{-6}	5.0	1.94×10^{-1}
60.0	1.55×10^{-3}	10.0	1.55

Table 5.3: Maximum Contribution of 3rd-Order Effects

each PRN in each data set, the Doppler was first calculated at times 0, 20, 40, and 60 s after the start of the data set. The Matlab *polyfit* function was then used to find a 2nd-order polynomial least-squares fit to the calculated points. The use of four points allows one degree of freedom in determining the polynomial coefficients. Thus, the quality of the fit can be represented by the residuals of the least-squares estimate. In all cases, residuals indicate less than 1×10^{-4} Hz error in the polynomial fit. Some resultant polynomial coefficients are presented in Table 5.4 for a representative sample of PRNs.

Further to evaluation by least-squares residuals, the quality of fit of the polynomial model to the broadcast ephemeris was examined at 5 second intervals for a pair of PRNs, one with a high estimated jerk parameter and one with a low jerk. The

PRN	$\dot{\phi}_o$ (Hz)	$\ddot{\phi}_o$ (Hz/s)	J_d(Hz/s^2) $\times 10^5$
3	-1033.836	-0.640411	4.026
8	-264.650	-0.597159	15.116
15	2141.441	-0.558431	-8.863
17	-2483.780	-0.450218	10.767
21	-448.423	-0.676747	2.684

Table 5.4: Sample Polynomial Doppler Model Parameters (Tube Data Set)

Doppler predicted by the broadcast ephemeris and that predicted by the polynomial at 5 second intervals for Tube PRN 21 and Terraario PRN 17 show a maximum model fit error of approximately 2.6×10^{-4} Hz, with average values below 1.0×10^{-4} Hz. This error is significantly smaller than other errors and will not significantly degrade coherent integrations of up to 20 s or more.

Implementation of Model in Software

For each PRN, the three parameters of the polynomial model are stored in an “info” file that is accessed during processing to actually implement the Doppler prediction. An example of such an info file is given in Appendix B.

5.4.2 Receiver Clock Errors

An error in the receiver clock frequency manifests as a measured Doppler effect. Also, any phase noise in the clock signal makes the Doppler appear to change rapidly. The estimated stability of the receiver clock provides a statistical estimate of the effect, but not a deterministic one.

Receiver clock stability depends on the external oscillator parameters and the frequency synthesizer used within the Digitizer. The implementation of the Digitizer frequency synthesizer is unknown, but direct RF downconversion is used, meaning a single LO with frequency near 1575.42 MHz is synthesized. We can assume that phase noise on the 1575.42 MHz output is at least equal to that on the reference oscillator, and likely higher, depending on the implementation. Long-term (aging) and short-term (Allan variance) stability can generally be calculated at the output frequency, using the parameters of the input oscillator. Peterson et al. (1995) states that such stability errors are multiplied by the same factor as the frequency, allowing stability calculation using 1575.42 MHz as the reference frequency.

Aging Rate	5×10^{-10} / day
Phase Noise	
1 Hz	-94 dBc/Hz
10 Hz	-115 dBc/Hz
100 Hz	-136 dBc/Hz
1 kHz	-144 dBc/Hz
Stability (Allan Deviation)	
1 s	3×10^{-11}
10 s	2×10^{-11}
100 s	4×10^{-11}

Table 5.5: Symmetricom ET-6000 Parameters

The external oscillator used with the Digitizer was a Datum ET-6000 OCXO. It was used to provide an external 10.0 MHz clock signal to the digitizer. Clock parameters for a Symmetricom (merged with Datum) ET-6000 OCXO are listed in Table 5.5. Over the course of each one-minute data set, the change in frequency due to aging is negligible, being on the order of 3.5×10^{-7} ppm, or 5.5×10^{-4} Hz at 1575.42 MHz. Short-term stability is more of a concern, however. At 1575.42 MHz, the one-sigma frequency error due to Allan variance (stability) is expected to be between 0.032 Hz (10 s duration) and 0.063 Hz (100 s duration).

The most significant effect limiting coherent integrations is determined to be the short-term stability of the receiver clock. Over 10 s, the one-sigma deviation of 0.032 Hz is a significant fraction of the first-null width of the power rolloff null of 0.1 Hz resulting from a 10 s integration. Integrations of this length should still be possible, but an apparent clock drift during the integration will manifest as a blurring of the frequency power rolloff function. Beyond 10 s, as durations increase toward 100 s, the stability of the clock decreases while the frequency stability requirements increase. By 20 s, the first-null frequency of 0.05 Hz is nearly as narrow as the frequency uncertainty, eliminating the possible reception of signals over this duration and beyond with the Datum ET-6000 oscillator.

5.4.3 Atmospheric Effects

Atmospheric propagation causes Doppler effects by advancing or delaying the carrier relative to the free-space case. Carrier phase advance caused by the ionosphere ranges from 1 m to about 50 m in extreme cases (Parkinson & Spilker, 1996). The magnitude of the carrier phase advance changes due to two effects: changing ionospheric conditions over time, and the changing elevation angle of the satellite. The troposphere contributes to carrier phase error as well, but it changes slowly and predictably over time and induces very little Doppler error (Parkinson & Spilker, 1996).

The Doppler induced by ionospheric changes may be calculated as

$$\Delta f = [(1.34 \times 10^{-7})/f]\frac{d}{dt}\text{TEC (in Hz)} \tag{5.3}$$

where TEC is total electron content, measured in electrons per square metre (Parkinson & Spilker, 1996). A TEC unit, TECU, represents 10^{16} electrons per square metre of ionospheric cross-section. The Doppler impact of the ionosphere can be calculated if changes in ionospheric TEC can be defined.

Changing Satellite Elevation Angle

As satellite elevation changes, the LOS path from receiver to SV pierces a changing amount of the ionosphere. While this layer is often modelled as an infinitesimally thin shell, the change in TEC can be by a factor of three or more. A mapping function, $M(E)$, is used to convert observed *slant TEC* (STEC)—the TEC observed through a non-vertical path—to a *vertical TEC* (VTEC) equivalent using the elevation angle E of the pierce point, as in Equation 5.4. The inverse of that mapping function may be used to predict the changing TEC as a function of SV elevation angle, assuming a constant ionosphere.

$$\text{VTEC} = M(E) \times \text{STEC} \tag{5.4}$$

A mapping function $M(E)$, has the form (El-Gizawy & Skone, 2002),

$$M(E) = \sqrt{1 - \left(\frac{R_E}{R_E + h}\right)^2 \cos^2 E}, \tag{5.5}$$

where E is the elevation angle, R_E is the radius of Earth, and h is the height of the ionosphere, given as a single number to represent a thin shell. The inverse of the mapping function, using $R_E = 6300$ km and $h = 350$ km, is plotted in Figure 5.5 showing the relative change in TEC due to elevation angle. The maximum rate of TEC change occurs at an elevation of 13.3°, and has value ±0.06/degree. This means that the phase delay may change by 6% for each degree of elevation change. Assuming a maximum phase delay of 50 m, and a rate of elevation change of 0.5°/minute, phase may change due to this effect by 1.5 m/minute, corresponding to a Doppler shift of 0.13 Hz at the L1 nominal frequency. However, more normal values of ionospheric delay are less than 10 m, yielding a Doppler effect of only 0.026 Hz. Additionally, most SVs change elevation by less than 0.5° per minute, further reducing the potential Doppler by some factor. In the observed data sets, the maximum elevation change rate is approximately 0.45°/minute, with other SVs showing lower rates of change.

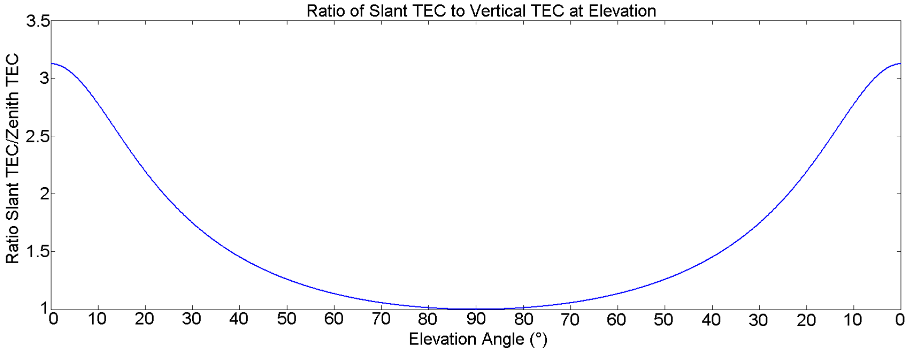

Figure 5.5: Inverse TEC Mapping Function

This Doppler effect can be modelled to some extent, if the absolute ionospheric delay is known. However, since it is thought that the induced Doppler will generally be less than 0.1 Hz, and that it is a fairly constant value over short periods, the effect will not be modelled for coherent integrations. The good stability of this Doppler should result in no negative effects on long coherent integrations, despite a bias similar to that caused by SV orbital prediction error. The potential effect of 0.1 Hz will necessitate, however, a large enough search window to account for the effect described. Although unlikely, the potential for Doppler exceeding 0.13 Hz cannot be discounted either, without knowledge of absolute ionospheric delay.

Changing Ionospheric Conditions

Daily (diurnal) changes in the electron content of the ionosphere, as well as rapid fluctuations known as scintillation, may cause additional Doppler effects. Typically, rates of TEC fluctuation due to these changes are below 0.005 TECU/s, which corresponds to 0.00425 Hz Doppler, except in exceptionally active circumstances (El-Gizawy & Skone, 2002). The Doppler due to SV motion tends to obscure these effects.

A review of ionospheric conditions near Finland has been conducted to check for possible significant Doppler effects. A global ionospheric activity index, K_p, had a value of between 3 and 5 at the time of data gathering, indicating moderate global ionospheric activity. A local estimate of between 3 and 4 was also made at Belsk, Poland (N69°, E40°)—the nearest local estimate to Tampere, Finland—for that date and time (GEO; NOAA). While this index does not translate directly to likely TEC gradients, the indication of moderate activity during data gathering makes it possible that ionospheric-induced Doppler effects could have exceeded 0.00425 Hz, but not likely to have exceeded 0.01 Hz (El-Gizawy & Skone, 2002).

These random ionospheric Doppler effects cannot be modelled effectively. Any effect induced by the ionosphere is therefore one of the effects to be measured in the data. However, ionospheric scintillation is expected to be insignificant for integration periods of up to 10 s except in exceptionally active periods.

5.4.4 Multipath

Doppler effects on NLOS paths have been discussed in Chapter 2. The combination of LOS and NLOS rays with different Doppler frequencies affects the measured frequency through combination of the sinc-squared power rolloff functions. The magnitude of these Doppler effects will be a function of the surrounding reflective surfaces and their relative motion. A realistic multipath Doppler limit of 0.03 Hz has been estimated in Chapter 2 for a static GPS receiver in a static environment. This is not a significant effect if a strong LOS signal is present, but may cause errors in measured Doppler if strong multipath is present. Under such conditions, a Doppler error of 0.03 Hz could severely affect long integrations, especially under changing multipath conditions. As an unpredictable effect, any multipath error will cause a Doppler effect that cannot be modelled, but must be measured from data.

5.4.5 Summary

Of the possible Doppler sources, only satellite orbital motion and clock errors are modelled deterministically. The polynomial used to model these two sources is thought to be accurate to within 0.01 Hz due to the level of error inherent in the broadcast ephemeris position. The remaining effects caused by receiver clock errors, atmospheric effects, and multipath will therefore contribute to measured Doppler error. The magnitude of Doppler induced by all of the contributing factors is listed:

SV Orbit / Clock:	Accuracy of polynomial: 1×10^{-4} Hz
	Error in ephemeris-based predictions: 0.01 Hz
Receiver clock:	0.032 Hz (1σ Allan deviation, 10 s period)
	5.5×10^{-4} Hz (Long-term aging; 60 s)
Atmospheric:	Extreme bias of up to 0.13 Hz possible
	Likely less than 0.1 Hz bias
	Low-level random effect less than 0.01 Hz
Multipath:	Varies depending on multipath strength and geometry
	Less than 0.03 Hz; Likely significantly lower

Based on the above, the most severe overall Doppler source is likely to be due to atmospheric delay. That effect should not impact coherent integrations greatly, however, because it remains relatively constant during short periods. The most severe limitation to long coherent integration is likely to be Digitizer frequency errors, primarily due to the short-term stability of only 0.032 Hz. A major implication of this fact is that the smaller Doppler effects due to multipath, random atmospheric errors, and any other minor effects will be obscured by the larger error of the receiver clock.

5.5 Test of HS Processing with Raw Reference Data

5.5.1 Approach and Objective

The performance of the HS analysis tool operating on Nokia's data sets is analyzed in this section. The reference data are tested to determine the longest integration that can reasonably be conducted on Digitizer data, and the resultant gain compared with that predicted theoretically. The main results are conclusions regarding the stability of the Digitizer data itself, based on an evaluation of the likely contributors to the integration limits.

5.5.2 Reference Signal Analysis

Method

The list of PRNs visible at the reference locations was given in Table 4.2. From that list, four PRNs received at the reference antenna for the Tube data set were analyzed representing a range of elevation and Doppler conditions: High-elevation PRN 8, low-elevation PRN 15 (ascending), low-elevation PRN 3 (descending), and low-elevation PRN 17 (descending). A set of integrations ranging from 100 ms to 20 000 ms in various increments were conducted for each PRN, with the power rolloff in the Doppler offset domain examined for each integration time. Using the 100 ms integration as a reference, the measured peak power was compared with that predicted theoretically (linear gain) and the point where actual power begins to diverge from that predicted theoretically was identified. Additionally, distortion of the power rolloff function has been analyzed to determine the likely cause of the limit on integration time.

Analysis Results

For PRN 8, the high-elevation satellite, the power measured at the peak code phase offset for a range of initial Doppler frequencies is shown in Figure 5.6 for integration times from 100 ms through 20 000 ms in various increments. For each power function, the corresponding theoretical sinc-squared rolloff characteristic is shown.

This theoretical function is located at the frequency predicted by the orbital Doppler model, with amplitude normalized using the linear gain equation from a basis of the 100 ms integration peak power.

For each integration time, the difference between the predicted Doppler frequency and the peak measured frequency is listed, along with the level of attenuation compared with the theoretical power. These statistics are tabulated for all PRNs analyzed in Table 5.6. The Doppler rolloff characteristics for PRNs 3, 15, and 17 are not shown because they are all very similar to PRN 8. Note that Doppler errors are shown with a variable number of significant digits due to different measurement precision used in each case.

Evaluation

For all PRNs, divergence of the theoretical from the measured power is clear as integration times exceed 10 000 ms. In addition, the nature of the measured peak becomes distorted in a manner as shown for PRN 8 in Figure 5.6. Considering the different Doppler frequencies, and the individually-derived Doppler model parameters, it is likely that the common distortion and gain falloff are caused by a common error.

Note that for all PRNs, there is some small Doppler error measured for integration times above 10 000 ms. Of note, the error for PRNs 3, 8, and 15 is positive, whereas that for PRN 17 is negative. Since PRNs 3 and 17 are both descending, any Doppler bias introduced by the ionosphere should have the same sign for those two PRNs. The opposite signs indicate that the bias is not only ionospheric. Examining only the integration times from 10-20 s, it should be noted that the measured

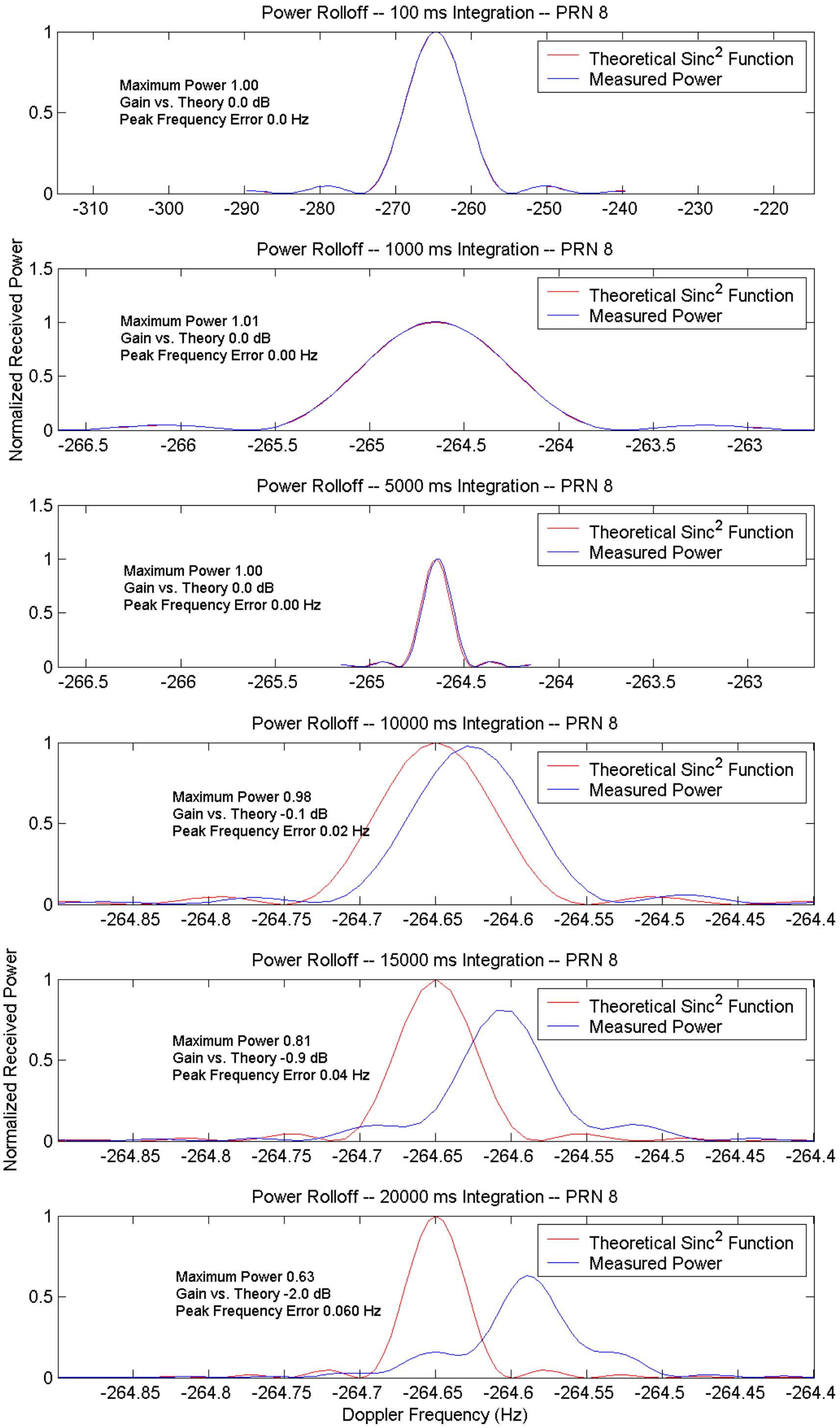

Figure 5.6: Received Power in Doppler Spectrum: Tube Reference PRN 8

Power Rolloff Characteristics for Long Integrations			
PRN	Integration Time (ms)	Doppler Error (Hz)	Gain vs. Theoretical (dB)
3	100	0.0	0.0
	1000	0.00	0.0
	5000	0.02	-0.4
	10000	0.02	-0.7
	15000	0.04	-1.4
	20000	0.060	-2.6
8	100	0.0	0.0
	1000	0.00	0.0
	5000	0.00	0.0
	10000	0.02	-0.1
	15000	0.04	-0.9
	20000	0.060	-2.0
15	100	0.0	0.0
	1000	0.05	-0.4
	5000	0.06	-0.3
	10000	0.07	-0.5
	15000	0.09	-1.1
	20000	0.105	-2.3
17	100	0.0	0.0
	1000	-0.15	-0.1
	5000	-0.12	0.0
	10000	-0.10	0.3
	15000	-0.09	-0.1
	20000	-0.070	-1.4

Table 5.6: Measured Doppler Rolloff Parameters with Increasing Integration Time

Doppler error for all PRNs is seen to increase by approximately 0.02 Hz for each five-second increase in integration time, regardless of the actual direction of the bias. This similarity, combined with the distortion at durations over 10 s, almost certainly indicates that the receiver clock is drifting during the integration. In fact, this postulate is supported by the theoretical stability of the clock as discussed in Section 5.4, which should support integrations of up to only about 10 s.

The actual value of the Doppler bias is possibly a result of some combination of Doppler-inducing effects, although none of those identified except for the ionosphere are thought to cause effects as large as 0.15 Hz. A base frequency error in the receiver clock is a possibility, but this is not directly supported by the values in Table 5.6 which do not show a consistent trend. Nonetheless, it is clear that the limiting factor in long integrations for a stationary Digitizer is common to all PRNs and must therefore be the clock stability limitation. Clock error has the effect of masking any of the more minor Doppler effects, including random atmospheric effects and multipath-induced Doppler. Unfortunately, therefore, only large-scale Doppler errors in the rover data, on the order of 0.1 Hz or larger, may be observed with the high-sensitivity analysis technique.

Maximum Gain

Each signal evaluated shows significant power loss at 15 and 20 s integration times compared with that expected from the standard gain equation. However, the measured power on each PRN is within 1 dB of that predicted theoretically up to 10 s integration time. Based on these analyses, an integration limit of 10 s will be used—a period for which it is believed that minimal distortion is caused by receiver errors.

From the standard gain equation $G = 2BT$, using B=4 MHz and T=10 s, the maximum achievable gain is 79 dB. Most reference signals are detectable with greater than 10 dB SNR after as little as 1 ms integration, which corresponds to only 39 dB processing gain. The more powerful reference signals are significantly higher than 10 dB after 1 ms. It should therefore be possible to measure fades 40 dB or more below reference levels.

Applicability of Results

The integration limit of 10 s derived above is applicable only under specific conditions. First and foremost, the receiver must be stationary for these limits to apply. A moving receiver experiences additional Doppler effects that are not accounted for in the Doppler modelling completed for this data. The 10 s limit is likely a result of the external oscillator stability. Thus, the use of any other oscillator will necessitate a re-visitation of this evaluation.

Finally, the ambient conditions of multipath, atmospheric effects, interference, and thermal noise are all specific to the data examined. Tests in other situations may experience different effects. For example, data gathered during an ionospheric storm may experience severe Doppler shifts that would limit integration times to less than 10 s. To generalize these results, more data gathered under various conditions would have to be measured and analyzed.

Chapter 6

Extraction of Channel Characteristics from Raw GPS Data

This chapter presents the results of raw data analysis work done as part of a cooperative research venture between the University of Calgary PLAN group and Nokia. Several individual analyses are reported, with discussion of the potential significance of the results.

6.1 Noise Floor Analysis

The first characteristic of the raw data sets analyzed is the level of noise and interference at the reference, Terraario rover, and Tube rover locations. On the assumption that noise is fairly constant at each receiver throughout the course of the data sets, this analysis develops a power threshold that ensures an accurate measurement even in the presence of noise.

6.1.1 Approach and Assumptions

All analysis is to take place post-correlation, examining either energy or power. Thus, a statistical description of the noise post-correlation is required. Standard C/N_o estimation techniques used in real-time GPS receivers may use noise statistics, as described in Parkinson & Spilker (1996), to estimate noise. As measurements are made at various stages of accumulation, statistics for narrowband power (NBP) and wideband power (WBP) are measured and compared to theoretical distributions. This research, on the other hand, uses a single statistical representation of noise determined post-mission because real-time operation is not required.

Noise Assumptions

It is assumed herein that the GPS signal is received in bandlimited AWGN, and that the power spectral density (PSD) of the noise—sometimes given as $N_o/2$, but referred to as N_o herein—is greater than the PSD of the sum of the GPS signals in the centre of the band. The power of the GPS signals is low enough that the overall noise + interference (N+I) is not appreciably different from AWGN alone, so the sum of these signals plus noise is considered simply a bandlimited AWGN process. Parkinson & Spilker (1996) provides a relationship between the level of co-channel interference and effective noise level as

$$N_{oeq} = N_o + \frac{2}{3}(M-1)P_s/f_c, \tag{6.1}$$

where the equivalent noise level at the centre of the spectrum is the ambient noise, N_o, plus a factor dependent on the number, M, and power, P_s of the interfering signals, and the spreading chip frequency, f_c. Assuming, for example, a very low noise level of -206 dBW/Hz and 10 strong GPS signals with level -157 dBW, Equation 6.1 gives a noise equivalent level of -204 dBW/Hz. The co-channel interference level is usually lower than this because of a lower number of satellites visible, higher noise level, and GPS signal attenuation, largely due to the antenna gain pattern. To determine the base level of N+I, it is reasonable to treat the total interference process as an AWGN process based on the relative insignificance of the co-channel interference under normal circumstances. The statistical nature of AWGN in the correlation process is discussed in the following sections.

6.1.2 Description of Noise Statistics

While the typical GPS receiver does Doppler demodulation prior to the correlation process, the statistical nature of noise is equivalent regardless of the order of operations because each of demodulation and accumulation is a linear process. The statistical nature of noise is derived below under those assumptions.

Statistics of AWGN in the Correlation Process

Accumulation & Correlation A sum of n uncorrelated samples of a Gaussian random variable (RV) with mean $\mu_G = 0$ and variance $\sigma_G^2 = v$ is a Gaussian random variable with mean $\mu = 0$ and variance $\sigma^2 = nv$ (Walpole et al., 1998). The assumption of uncorrelated samples in the time domain is not necessarily met when the Gaussian RV is bandlimited, but over a sufficiently large number of samples, the result is statistically equivalent. Thus, the output of AWGN accumulation is a zero-mean Gaussian RV with variance nv when there is no signal present. Correlation with an incorrect C/A code does not alter the nature of this output.

The integration operation over T seconds acts as a sinc-squared shaped filter with main lobe width of $2/T$ Hz (Parkinson & Spilker, 1996). This has a noise equivalent (rectangular equivalent) bandwidth of $1/T$ Hz. Therefore, while the variance of the resultant (accumulated) RV is increased by n during accumulation, its bandwidth is simultaneously decreased.

Doppler Demodulation The input to the demodulator, which is output from the accumulator, is a zero-mean Gaussian RV with noise equivalent bandwidth of

1/T Hz, which is less than the potential Doppler bandwidth. Mixing with a sinusoid in the time domain increases the bandwidth of the noise process, but reduces its amplitude by $1/\sqrt{2}$ and variance by 1/2.

The output noise process in the energy domain is a Gaussian RV with mean $\mu_G = 0$ and variance $\sigma_G^2 = nv/2$. The RV may be scaled by a factor of $1/\sqrt{n}$, which scales the variance by $1/n$. This eliminates the dependence of the output variance on accumulation time. If the scaled outputs of two correlators (accumulated and demodulated) are squared and added, as in the case of inphase and quadrature components, the result is a RV with gamma distribution, defined by parameters $\alpha = 1$ and $\beta = 2\sigma_G^2$. The mean of the gamma distribution is $\mu = \alpha\beta = v$ and its variance is $\sigma^2 = \alpha\beta^2 = v^2$ (since $\alpha = 1$). With the given parameters, the gamma distribution reduces to the exponential distribution as follows:

$$\begin{aligned} f_y(y) &= \frac{1}{2\sigma_G^2} \mathrm{e}^{\frac{-y}{2\sigma_G^2}}, y \geq 0 \\ &= 0, \text{ otherwise.} \end{aligned} \tag{6.2}$$

Statistics of AWGN + Desired Signal in the Correlation Process

In the presence of a desired GPS signal, the accumulation operation results in a sinusoidal signal plus noise. The mean is approximately zero, with absolute variance dependent on signal amplitude. Demodulation converts the sinusoidal signal to a constant level, giving a Gaussian RV with some non-zero mean $\mu_G = m$ and the same variance as observed in the AWGN case, $\sigma_G^2 = nv$. Scaling by $1/\sqrt{n}$ gives a mean $\mu_G = m/\sqrt{n}$ and variance $\sigma_G^2 = v$. Squaring and adding the I and Q energy signals to obtain power yields a scaled noncentral chi-squared distribution with two degrees of freedom and non-centrality parameter $\lambda = 2(\mu_G/\sigma_G)^2 = 2m^2/nv^2$ (Lee &

Miller, 1998). The distribution is given below.

$$\begin{aligned} f_y(y) &= \frac{(\alpha/\sigma^2\lambda)^{(N-2)/4}}{2\sigma^2}\exp\left(-0.5(\frac{\alpha}{\sigma^2}+\lambda)\right)I_{\frac{N}{2}-1}\left(\sqrt{\frac{\lambda\alpha}{\sigma^2}}\right), y \geq 0, \qquad (6.3) \\ &= 0, \text{otherwise} \end{aligned}$$

The mean and variance of the distribution are given in Equations 6.4 and 6.5 respectively (Weisstein, 2005).

$$\begin{aligned} \mu &= (2+\lambda)\sigma_G^2 \\ &= 2v + 2m^2/(nv) \qquad (6.4) \\ \sigma^2 &= 4(1+\lambda)(\sigma_G^2)^2 \\ &= 4v^2 + 8m^2/n \qquad (6.5) \end{aligned}$$

6.1.3 Data Analysis

The probability distributions likely to be output from the receiver operation have been defined for cases in which a desired GPS signal is present or absent. The raw data are now analyzed and the probability distributions observed and compared with the theoretical distributions. The distributions should be sufficient for any integration period, as the level is scaled in the software depending on integration time to maintain a constant reference.

Measurements

Power was first measured throughout the data sets using a single correlator and a non-existent PRN for cross-correlation, specifically PRN 19 which was not a part of the GPS constellation in September, 2003. The demodulating frequency used was 0 Hz, which is more than 250 Hz removed from the nearest signal present in the data (PRN 8). All of the signals should therefore remain widely spread across the frequency domain and the resultant distribution should be approximately the gamma distribution of Equation 6.2. Integration periods of 1 ms, 5 ms, and 20 ms were tested using this method to ensure consistency, providing 60 000, 12 000, and 3 000 samples respectively from the 60-second data sets.

Following that, the single correlator was moved to a location known to contain significant signal power—that of PRN 8. The signal was received with the correct PRN code, adjusting for Doppler during the test, and the power distribution once again measured, but this time using only a single integration period of 1 ms. The results of the signal-present test were compared with those from signal-absent conditions and appropriate noise distributions selected.

For reference, raw probability distributions from these measurements are presented in Appendix E. Fitting of measured probability distributions to theoretical ones was done using a least-squares fit to the scaled noncentral chi-squared distribution with two degrees of freedom (Equation 6.3). This is the most general case of the theoretical distribution for signal-present and signal-absent cases. Since it is assumed that the power distribution results from two identical, uncorrelated Gaussian energy distributions, the fitted power distribution implies the nature of the source Gaussian distributions.

Probability Distributions

Tube and Terraario Reference Distributions Time-series representations of measured power are shown in Figures E.1–E.4 for the Tube reference data set using various integration times. The figures also include probability distributions of the power measurements, and the best-fit noncentral chi-squared distributions for each distribution. Equivalent data from the Terraario reference data set are presented in Figures E.5–E.8.

The fit of the Tube reference measurements to theoretical distributions for the 5 ms and 20 ms noise measurements have Gaussian source means of 0.40 and 1.00, compared to 0.10 for the 1 ms case. This indicates likely cross-correlation power that increases with integration time. The 1 ms integrations for a non-existent PRN and for PRN 8 show similar Gaussian source variance, 3.95 and 3.85. These values will be used along with data from the Terraario reference data set to determine a reference noise distribution.

The Terraario noise data shows more consistent statistics between 1 ms, 5 ms, and 20 ms integration times. This is a good indication that the scaling method successfully accounts for increasing noise with integration time. Due to the less robust fit with the smaller sample sets (5 ms and 20 ms), we will consider the 1 ms noise and 1 ms PRN 8 statistics to develop a noise floor. The former sample has Gaussian source variance of 3.75, and the latter Gaussian source variance of 3.90.

The mean Gaussian source variance implied by the four reference 1 ms distributions considered is 3.86. The scaled chi-squared distribution that results from squaring two zero-mean Gaussian processes with variance 3.86 has mean and standard deviation of 7.73. Based on that scaled chi-squared distribution, the 99% noise power level is 35.45, and the 95% level is 23.03, based on the cumulative density function (CDF) in the first panel of Figure 6.1.

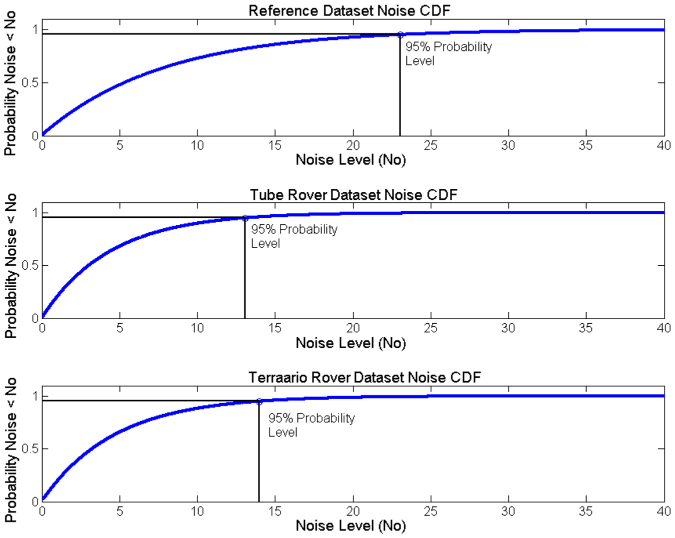

Figure 6.1: CDFs of Reference, Tube Rover, Terraario Rover Noise Levels

Tube Rover Distribution Time-series representations of measured power are shown in Figures E.9–E.12 for the Tube rover data set using various integration times.

Noise power statistics are similar for all integration periods in the Tube rover data set. The distribution of PRN 8 power is seen to decrease during the data set, skewing its statistics somewhat. The distribution observed for the 1 ms noise integration is consistent, and it seems reasonable to use the Gaussian variance of 2.20 as a noise floor for this data set.

The scaled chi-squared distribution that results from squaring two zero-mean Gaussian processes with variance 2.20 has mean and standard deviation of 4.40. Based on that scaled chi-squared distribution, the 99% noise power level is 20.18, and the 95% level is 13.08 as calculated from the CDF in the second panel of Figure 6.1.

Terraario Rover Distribution Time-series representations of measured power and the best-fit noncentral chi-squared distributions for each are shown in Figures E.13-E.16 for the Terraario rover data set.

Noise power statistics are again similar for all integration periods in the Terraario rover data set. The Gaussian variance determined from the measurement of PRN 8 power is slightly lower than the other three measurements, but is still consistent. The most robust fit, from the 1 ms noise integration is therefore used to define a noise floor, with Gaussian variance of 2.35 on each channel.

The scaled chi-squared distribution that results from squaring two zero-mean Gaussian processes with variance 2.35 has mean and standard deviation of 4.70. Based on that scaled chi-squared distribution, the 99% noise power level is 21.55, and the 95% level is 13.98 as calculated from the CDF in the third panel of of Figure 6.1.

6.1.4 Definition of Valid Power Level Thresholds

With the noise distributions given, power measurements cannot be considered valid for low levels as random noise contributes a significant amount to the measurement. For purposes of this research, we choose to set a threshold level of SNR for which 95% of power measurements are accurate to better than 1 dB. Noise power is positive, but can be received in such a way to reduce signal power. A reduction of signal power by the 95% noise level constitutes the worst case for the threshold criterion defined above, and will be considered to determine signal measurement thresholds.

Reference Data Sets

The 95% noise power level for reference data sets is 23.03, with a mean of 7.73. The SNR level for which a measurement error of 23.03 represents less than 1 dB error is determined: A -1 dB error occurs when error is -20.6% of the noiseless value. For an error of 23.03, this corresponds to a noiseless value of approximately 112 units. We therefore set the minimum valid power measurement as 112 units, which corresponds to an SNR of 11.6 dB on a mean noise of 7.73 units. If measured SNR is greater than or equal to 11.6 dB, the measurement is accurate to 1 dB with 95% confidence. In fact, this value of 11.6 dB is the minimum -1 dB threshold for any scaled chi-squared noise distribution, so it applies to both of the rover data sets as well. In those cases, the numerical levels corresponding to 11.6 dB are determined given their average noise levels.

Tube Rover Data Set

The 95% noise power level for the Tube rover data set is 13.08 units, with mean noise power of 4.40 units. To achieve a minimum SNR of 11.6 dB with 95% confidence, the numerical threshold with a 13.08 unit noise level is 63.6.

Terraario Rover Data Set

The 95% noise power level for the Terraario rover data set is 13.98 units, with mean noise power of 4.70 units. To achieve a minimum SNR of 11.6 dB with 95% confidence, the numerical threshold with a 13.98 unit noise level is 68.0.

6.2 Indoor Fading: Preliminary Analysis

The reference and rover data sets are processed to obtain estimates of the overall C/N_o drop induced by each indoor environment. The goal is to approximately characterize these effects and determine PRNs and epochs which are suitable for more detailed analyses.

6.2.1 Gain Computations and C/N_o–SNR Relationship

For purposes of this analysis, processing gain is calculated using an RF front-end 2-sided bandwidth of 8 MHz, or a single-sided pseudo-baseband width of 4.0 MHz. The standard gain equation, $G = 2BT$, is used to compute the SNR gain through processing. Initial SNR is estimated using the gain equation and the measured post-correlation SNR.

Carrier-to-noise-density ratio is related to initial SNR by the front-end bandwidth. In effect, due to lowpass filtering with corner frequency around 4.0 MHz, the RF front end bandwidth is limited to 8.0 MHz, although the front end filters are in fact wider. The relationship in logarithmic terms is simply $C/N_o = SNR + B$. Using $B = 8.0$ MHz, the difference between C/N_o and SNR is 69 dB.

The C/N_o calculated using the above method is that of the digital signal input to receiver processing. It includes things such as RF receiver noise and quantization noise. RF noise cannot be accounted for without knowledge of the receiver implementation, but the effect of quantization noise can be estimated. The digitizer uses 3-bit quantization, using 7 levels. The signal input to the analog-to-digital converter (ADC) is approximated as a white Gaussian process, for which it is assumed that automatic gain control is used to maintain the signal at an optimal level for quantization. Parkinson & Spilker (1996) relates output SNR degradation to quantizer levels in the case of Gaussian noise with some variance σ_G. The measured variance of the raw signal from the digitizer is approximately 2.5, with steps of 1 unit. If that value is presumed to be approximately the analog signal variance, Parkinson & Spilker (1996) (p. 740) gives the degradation resulting as approximately 0.25 dB if the desired signal level (buried in noise) is ±0.25. The actual degradation is likely to be near this value for signals from the digitizer. Without detailed knowledge of the digitizer's implementation, however, it seems imprudent to add further adjustments to measured results. We therefore report the C/N_o calculated using the two-stage adjustment above as the actual value.

Fading is calculated simply as a difference between reference and rover C/N_o. While this does not account for differing gain and noise levels on the reference and rover, it does represent a comparison of the most important parameter of GPS signal power, being the C/N_o. Ability to track and receive signals depends on strength relative to noise and interference, rather than absolute strength.

6.2.2 Tube Data Set Preliminary Fading Analysis

Reference C/N_o Measurement

The reference data set power has been measured with 200 ms coherent integration times, corresponding to 62 dB processing gain according to the standard equation. At each epoch, the search space used was ±0.1 chips wide, in increments of 0.02 chips, by ±0.02 Hz in increments of 0.01 Hz. In all cases, the measured code phase fell within the ±0.1 chip limits, indicating reception of the peak power in the code offset domain. In the Doppler offset domain, however, the measured peak power reached the maximum tested error of 0.02 Hz from the predicted frequency during most of the test. In fact, this Doppler test domain was chosen badly, and this error was to be expected given the observed clock instability and other bias sources. A further test was conducted to evaluate the possible power measurement error caused by the Doppler error. A test with only 1 code offset—the presumed code offset—and a Doppler search space of ±0.3 Hz in 0.15 Hz increments was conducted to evaluate the effect. In most cases, Doppler error measured with this coarser resolution was less than 0.3 Hz. In some instances, however, the measured Doppler again reached the maximum tested Doppler of ±0.3 Hz from the presumed Doppler. In these cases, however, measured power was virtually identical to that measured with the initial test, despite a frequency difference of up to 0.28 Hz. Differences in measured power were less than 0.02 dB between the two.

A 200 ms integration time gives a first-null power rolloff width of 5 Hz. In this case, the 1 dB attenuation point in the power rolloff function occurs at approximately ±1.31 Hz from the actual frequency. If absolute error is larger than 1.31 Hz, a change of 0.28 Hz should cause a significant change in power measurement. A decrease in error from +2 Hz to +1.72 Hz, for example, causes over 0.65 dB increase in power. Therefore, the small level of change is taken to indicate that the predicted Doppler frequency is sufficiently accurate to represent actual SNR to within 1 dB, as long as the absolute measurement is greater than the 11.6 dB threshold discussed earlier. Reference C/N_o measured with this technique is shown in Figures 6.2–6.3.

Rover C/N_o Measurement

For all PRNs, an initial integration period of 1000 ms has been used. This corresponds to 69 dB processing gain. To account for larger possible fluctuations in received code offset and frequency, a coarser search space has been used than was used for the reference data sets. Code offsets of ±0.5 chips with resolution of 0.05 chips were tested, in only 3 Doppler bins with offsets of 0 Hz and ±0.3 Hz. Only one instance of the maximum code offset error of 0.5 chips was measured, indicating that most power measurements are valid estimates of peak power. Several instances of 0.3 Hz frequency error were measured. These instances were subsequently examined with a higher-resolution search involving frequencies of ±1 Hz in 0.1 Hz resolution. In all but one case, the initially-measured frequency offset was determined to be accurate to within 0.15 Hz. With 1000 ms integration time, 0.15 Hz represents a power attenuation of 15% of the power rolloff width. This corresponds to less than 1 dB attenuation. We therefore consider the measured rover power accurate in cases where SNR exceeds the 11.6 dB threshold. Rover C/N_o measured with 1000 ms integration time is presented in Figures 6.2–6.3 along with the reference and fading data. Fading statistics are presented in Table 6.1.

Discussion: Tube Preliminary Fading

The fading measured on the Tube data set is in no way a general case. First, with only 60 s of data, long-term fading characteristics are not measurable. Also, due to the long integration time used to receive the rover data, only 60 independent samples are available from each satellite. Being aware of those limitations, however, some interesting characteristics are observed in the data. A reasonable dependence

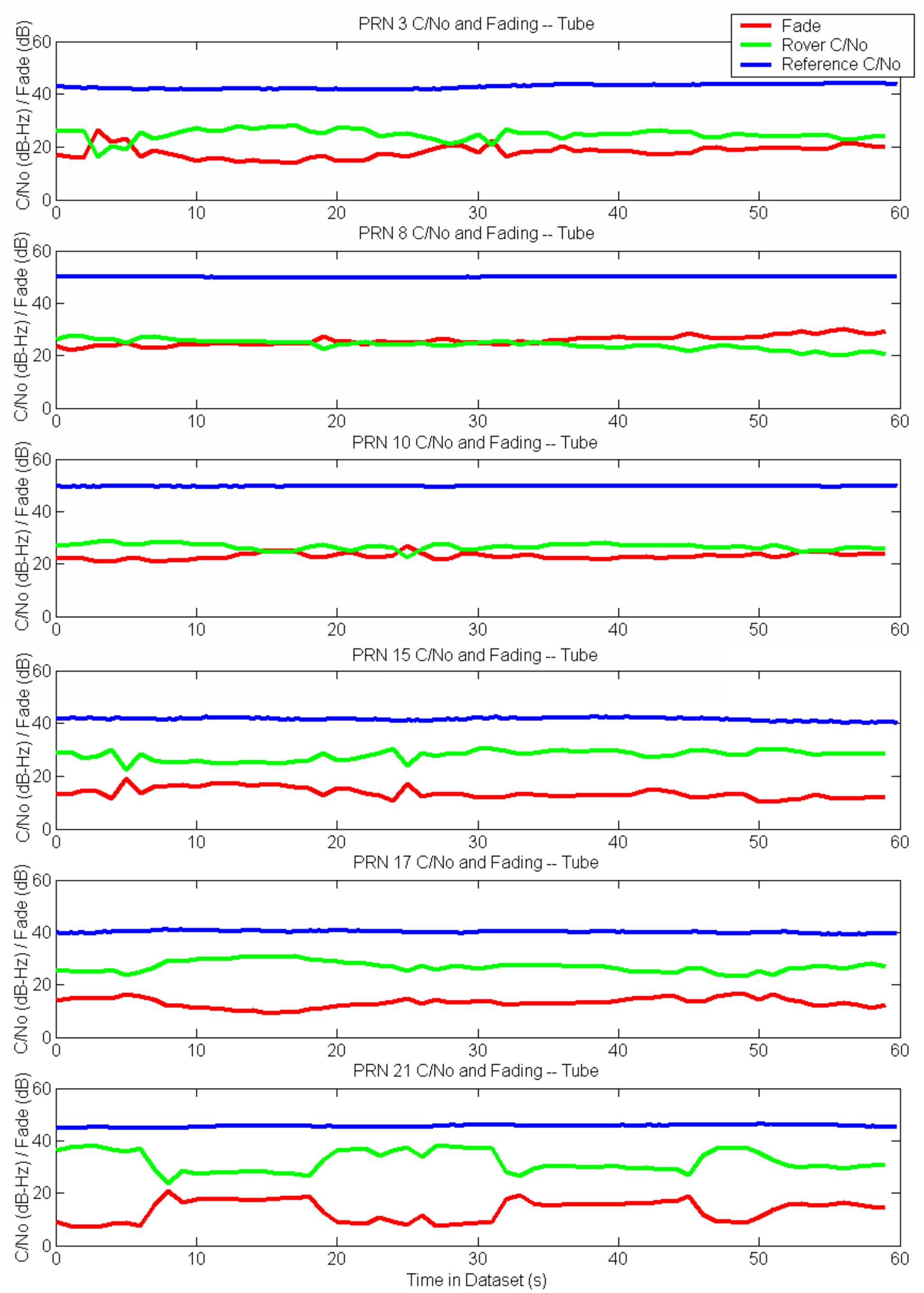

Figure 6.2: C/N_o and Fading: Tube Data Set PRNs 3–21

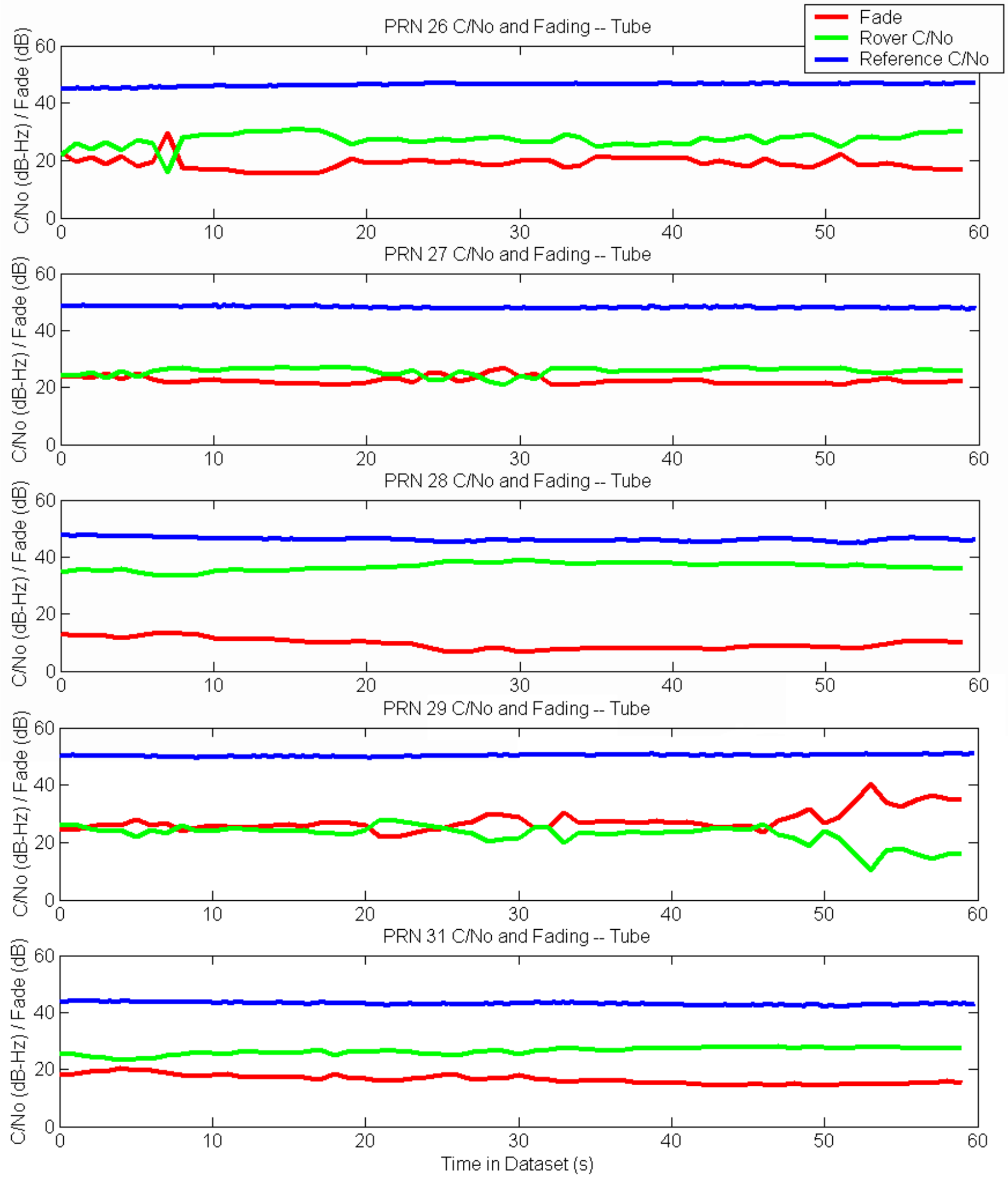

Figure 6.3: C/N_o and Fading: Tube Data Set PRNs 26–31

PRN	Max	Min	Mean	Std Dev
3	26.2	14.1	18.1	2.4
8	30.1	22.3	25.8	1.9
10	27.0	20.7	23.0	1.2
15	19.3	10.2	13.7	2.0
17	16.6	9.3	13.2	1.8
21	20.9	7.1	13.4	4.1
26	29.7	15.3	19.1	2.3
27	27.0	20.8	22.5	1.3
28	13.4	6.8	9.5	1.9
29	40.3	21.8	27.5	3.6
31	20.4	14.3	16.6	1.6
Overall mean fade: 18.4 dB				

Table 6.1: Fade Statistics for Tube Data Set

of fading on the propagation path can be seen in the data, as highlighted in Figure 6.4. Most visibly, high-elevation satellites experience higher mean fades. As before, satellite elevation is represented in Figures 6.4 and 6.7 by length of the line, which has been defined as the cosine of the elevation angle.

Low Fade Satellites Several signals were received with mean fade below 15 dB, specifically PRNs 15, 17, 21, and 28. For each of these PRNs, the maximum fade level was also relatively low, at approximately 20 dB or less. Referring to Figure 6.4, PRNs 15 and 28 were received from the north and south respectively, with low or moderate elevation (8.7° and 36.2°), which would allow a direct path through the outer glass walls of the Tube. Conversely, PRNs 17 and 21—both low elevation satellites at 13.0° and 17.1°—had their direct paths from the west obstructed by the main building. One hypothesis for the strong signals in these cases is that specular reflections from the eastern building reached the antenna. Notably, the signal strength of PRN 21

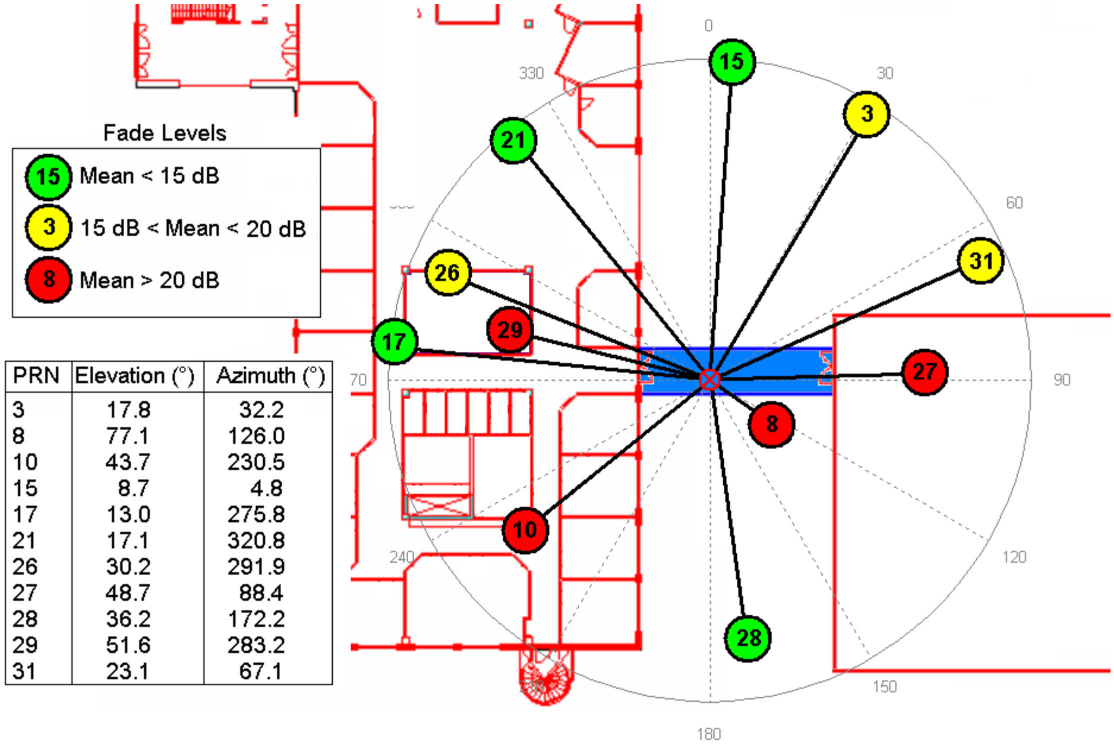

PRN	Elevation (°)	Azimuth (°)
3	17.8	32.2
8	77.1	126.0
10	43.7	230.5
15	8.7	4.8
17	13.0	275.8
21	17.1	320.8
26	30.2	291.9
27	48.7	88.4
28	36.2	172.2
29	51.6	283.2
31	23.1	67.1

Figure 6.4: Tube Mean Fade by Satellite Elevation & Azimuth

shows a strong periodicity of approximately 12–15 s. The fade alternates between low levels and moderate to high levels with this period. The possible causes will be investigated in further analyses.

Moderate Fade Satellites Three signals were received with mean fades from 15 dB to 20 dB, specifically PRNs 3, 26, and 31. The direct propagation path of PRN 3 is substantially similar to those of PRNs 15 and 28, but its fade statistics are noticeably higher than the former two PRNs. As seen in Table 6.1, the standard deviation of PRN 3 is slightly higher, indicating a more variable signal. Further tests may shed light on the possible causes for the differences between PRN 3 and PRNs 15 and 28.

PRNs 26 and 31 both have moderately low elevation (30.2° and 23.1°), but significantly different statistics. While both signals have mean fade between 15 and 20 dB, the maximum fade of PRN 26 reaches nearly 30 dB, whereas that of PRN 31 reaches only 20 dB. The difference in signal strength variability is demonstrated by the different variances of the two signals. The major difference between the two signal paths appears to be the proximity to the buildings in the east and west. PRN 26 is apparently blocked by the western building, whereas PRN 31 may not be blocked. High rate fading analysis and other tests may provide an evaluation of this.

High Fade Satellites The remaining four signals from PRNs 8, 10, 27, and 29 were received with mean fade levels exceeding 22.5 dB, and minimum fades in excess of 20 dB. These are all moderate- to high-elevation satellites, ranging from 43.7° to 77.1°. Due to their elevation and azimuth, it appears likely that the signals from PRNs 8, 27, and 29 all have a direct propagation path through the ceiling of the Tube, which is not made of glass. The exact composition is unknown, but in other structures a metal roof has been shown to cause high fades on high elevation satellites (Lachapelle et al., 2003a). If these signals are, in fact, propagating directly through the ceiling of the Tube, they should show minimal multipath degradation but significant attenuation.

All Satellites—General Characteristics Fading in the Tube environment averages 18.4 dB, with levels ranging from 6.8 dB to greater than 40 dB, depending on the satellite. The range of values is not indicative of a statistical variation over time, however, but of the differences between various propagation paths. To model this type of fading statistically, a number of models would be required to account for the geometric nature of the complex environment. This is not practically feasible given the level of detail required and the temporal variations that may occur.

Since all signals propagate through some building material, the fade metric shown includes both attenuation and multipath fading. Over 60 s, fading measured at 1 Hz shows little variability regardless of the mean level. Fades are correlated to within a few dB over the entire data set, except for the unusual behaviour of PRN 21. If a large component of the total fade is due to multipath interference, this may indicate that the multipath does not change significantly over 60 s and fading coherence times are long. An alternative explanation is that most of the total fade is due to attenuation, with higher-frequency multipath fading not observable due to the time averaging effect of integration. These alternatives will be explored in further analyses.

6.2.3 Terraario Data Set Preliminary Fading Analysis

Reference Power Measurement

Power for the Terraario reference data set has been measured with 200 ms coherent integration times using an identical search technique as described earlier. The same type of frequency errors were observed in the initial search as were discussed in the Tube reference data set. A further test with Doppler search space of ±0.3 Hz indicated that the frequency errors were minimal, resulting in no significant power measurement error.

Rover Power Measurement

The rover data gathered in the Terraario environment is much weaker than that from the Tube environment analyzed previously. A preliminary attempt at power measurement using 1000 ms integrations yielded some valid detections above the 11.6 dB threshold, but in the majority of epochs the power was too low to be considered an accurate measurement.

To achieve a higher percentage of valid measurements, integration time was then increased to 5000 ms, providing an additional 7 dB of processing gain. The first-null frequency rolloff with this integration time is only 0.20 Hz. A search space of ±0.75 chips in 0.15 chip increments and ±0.60 Hz in 0.15 Hz increments was used to detect power above the threshold. The large increments were used to ensure detection with reasonable processing time, but do provide some power measurement error. The maximum frequency error is 0.075 Hz in this scheme, corresponding to approximately 38% of the power rolloff null. The attenuation with that level of error is up to 2.1 dB. Thus, while the additional integration time provides 7 dB gain, the actual gain realized may be as low as 4.9 dB. Unfortunately the cost of processing time was too severe to attempt higher resolution.

SNRs resulting from 5000 ms integrations are above the SNR threshold with greater frequency than the 1000 ms results. Signals remain below the threshold, however, for certain PRNs throughout the data set and for other PRNs during some portions of the data set. The C/N_o and fading for each PRN using the 5000 ms integration time are presented in Figures 6.5 and 6.6. Rover C/N_o and fading are represented by bar plots to emphasize the fact that the measurements are averages of a long segment of data.

The maximum, minimum, and mean fade levels are presented in Table 6.2 for those epochs during which a signal was detected above the threshold. Since a lack of detection likely indicates a higher fade level, these statistics are not completely representative of the environments. An availability measure is also provided, being the percent of epochs during which signal was detected.

PRN	Max (dB)	Min (dB)	Mean (dB)	Availability (%)
3	37.9	28.6	33.6	83.3
8	46.0	39.5	43.6	75.0
10	N/A	N/A	N/A	0.0
15	34.2	34.2	34.2	8.3
17	34.8	34.8	34.8	8.3
21	N/A	N/A	N/A	0.0
26	38.9	34.1	36.3	100.0
27	42.3	33.9	36.6	83.3
28	41.4	36.2	38.7	100.0
29	45.0	38.8	42.6	83.3
31	35.4	31.8	33.5	100.0

Table 6.2: Fade Statistics for Terraario Data Set

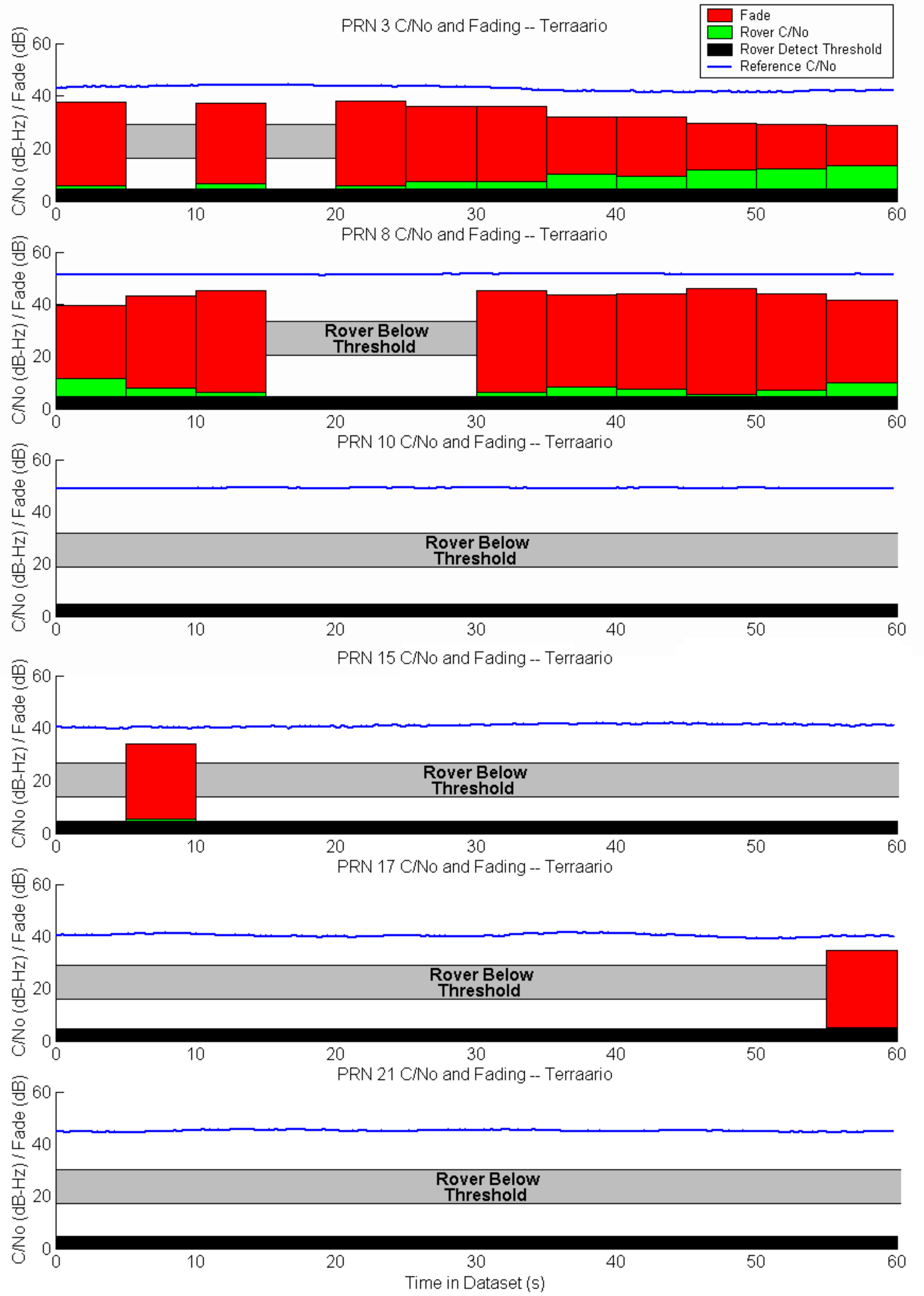

Figure 6.5: C/N_o and Fading: Terraario Data Set PRNs 3–21

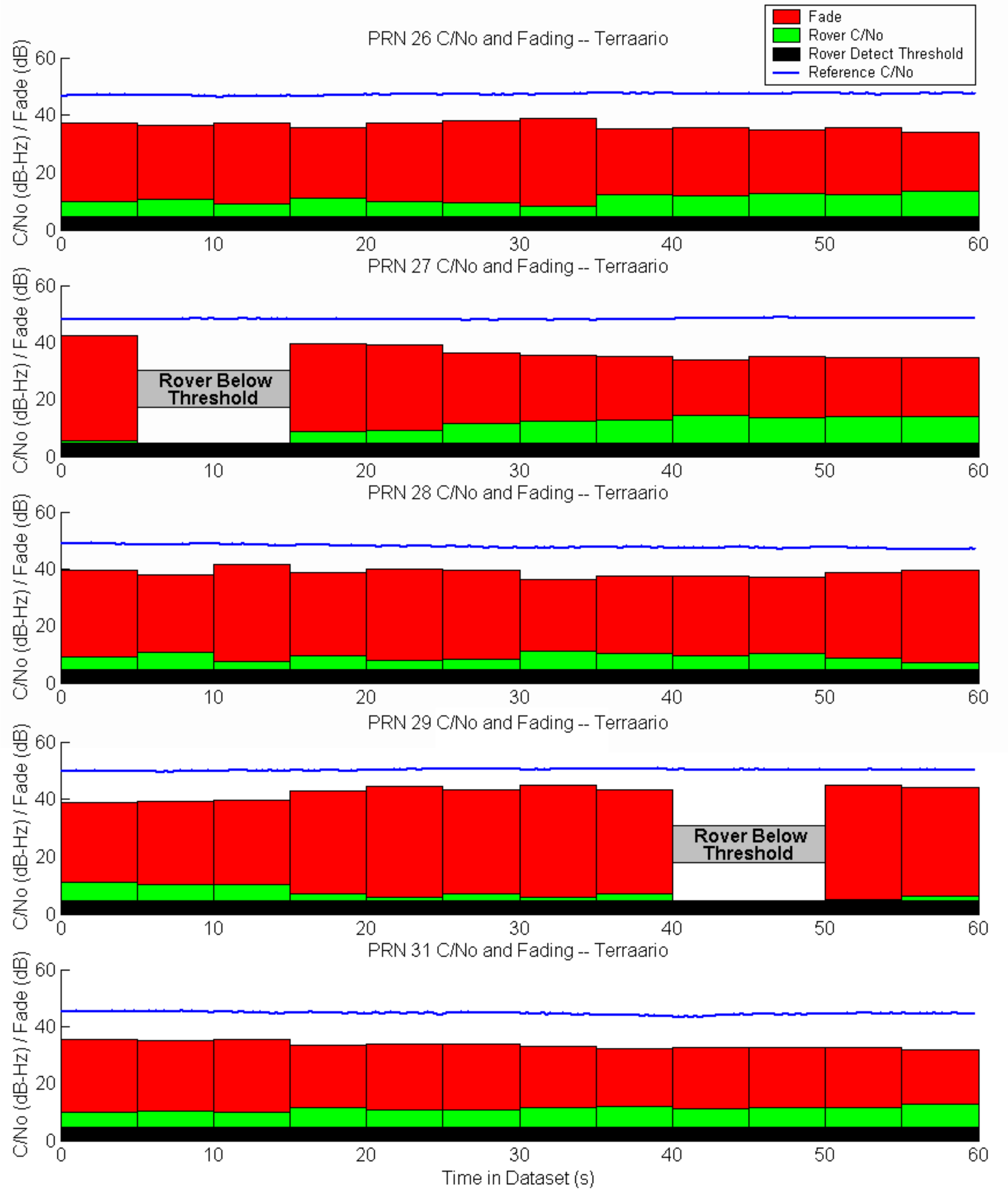

Figure 6.6: C/N_o and Fading: Terraario Data Set PRNs 26–31

Discussion: Terraario Preliminary Fading

Fading observed deep inside a building is much deeper than that observed in the fairly open Tube environment. In this case, results are even more limited than in the Tube case. Each 60 s data set provides only 12 independent fading samples for each PRN, with several missed detections even when using a 5000 ms integration time. These limited fading characteristics are discussed in the following paragraphs and presented in Figure 6.7.

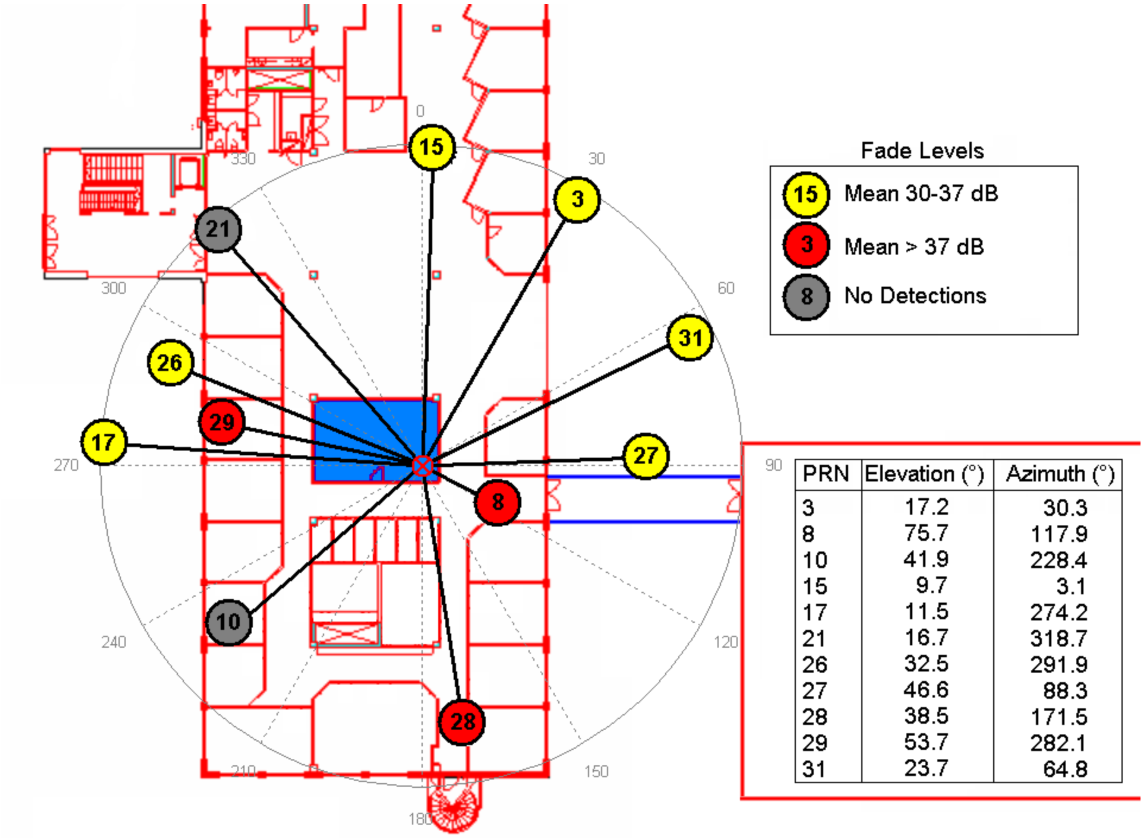

PRN	Elevation (°)	Azimuth (°)
3	17.2	30.3
8	75.7	117.9
10	41.9	228.4
15	9.7	3.1
17	11.5	274.2
21	16.7	318.7
26	32.5	291.9
27	46.6	88.3
28	38.5	171.5
29	53.7	282.1
31	23.7	64.8

Figure 6.7: Terraario Mean Fade by Satellite Elevation & Azimuth

Missed Detection and Low Availability Signals Signals from PRNs 10 and 21 were not detected above the required SNR threshold in the Terraario environment. Using 5000 ms integration, the detection threshold of 11.6 dB SNR translates to a C/N_o detection threshold of approximately 4.6 dB-Hz. Given that these PRNs have reference signals stronger than 45 dB-Hz, this implies that the signals undergo fades larger than 40 dB. In fact, it appears that some signal has been detected below the defined threshold for each of these PRNs, but the level cannot be determined with sufficient accuracy to report results.

PRNs 15 and 17 each have only one valid fading measurement, both of approximately 34 dB. These PRNs have the lowest reference power levels of only 40–42 dB-Hz. Combined with the detection threshold of 4.6 dB-Hz, the maximum fade that can be validly measured in this case is approximately 37 dB. This is a fundamental limitation of the HS processing technique. Those signals with the weakest reference power are likely to experience high fades. However, the ability to measure high fades is also most limited by the weak reference power.

High Availability Signals The remaining seven signals were received above the detection threshold during at least 75% of the epochs of test. The lowest average fades occur for PRNs 3 and 31, with mean levels of approximately 33.6 and maxima below 38 dB, for epochs with detected signals. These low-elevation satellites are both in the east-northeast direction, with their direct propagation paths presumed to pass through the eastern wall of the building and a glass wall of the Terraario meeting room.

The next higher fades of approximately 36.5 dB are observed for PRNs 26 and

27. These are mid-elevation satellites in the west and east respectively. Observed from the Terraario antenna, the direct propagation path from these satellites would appear to pass through the roof of the building at a fairly low angle.

The highest measured fades are on the signals of PRNs 8, 28, and 29. PRN 28 has mean fade of 38.7 dB, while PRNs 8 and 29 have mean fades near 43 dB. Interestingly, as before, the highest-elevation satellites—PRNs 8 and 29—suffer from the highest average fading. Two possible explanations are considered. First, it may be the case that a mechanical room on the roof of the building causes significant signal disruptions for those signals which are of high enough elevation to pass through that room. A second explanation involves the measurement technique. Because PRNs 8 and 29 have the highest reference C/N_o, they have the ability to tolerate the largest fades before rover signals drop below the detection threshold. Thus, while larger fades are not measured on other PRNs, they are observed on these high-elevation signals. This does not appear to be the cause of the high fades, however. The availability of signals from PRNs 8 and 29 is 75% and 83% respectively. It is likely, therefore, that fades exceeding the large measurement threshold occurred. Meanwhile, PRNs 3, 26, 27, 28, and 31 all have similar or higher availability ranging from 83% to 100%, meaning that most fades occurring on these PRNs were within their smaller measurement threshold.

All Satellites—General Characteristics Mean fade of detected signals in the Terraario environment is 37.6 dB. Missed detections indicate higher fades, giving an overall mean fade greater than 37.6 dB. As with the Tube data set, the fade levels observed vary significantly depending on the satellite. A significant amount of the total fade is believed to be due to building attenuation, with some contribution from multipath interference. The level of each contribution cannot be determined from the fading data.

Time-domain variability of the signal strength on any given satellite is more pronounced in the Terraario environment. For example, the average strength of PRN 3 increases consistently, reaching a power level almost 10 dB higher at the end of the data set than at the beginning. Other PRNs have similar long-term changes. Conversely, some PRNs show almost no variability of signal strength over 60 s. PRN 31, for example, shows less than 4 dB difference between its maximum and minimum powers. The long averaging from using 5 s integration completely obscures any fading effects with higher frequencies.

6.2.4 Evaluation of Fading Results

While the limited amount of data does not lend itself to drawing general conclusions, a significant correlation has been observed between satellite azimuth and elevation and signal fading. The factor correlating these two elements is more than likely the geometry and composition of the surroundings, as has been observed in past research.

Fading analysis of a limited data set does not provide sufficient information to determine and separate the effects of environmental attenuation from those of multipath interference. With large amounts of data, attenuation effects may be observed as a bias in fading. This technique has been used with commercial high-sensitivity receivers in the PLAN group (Lachapelle et al., 2003b). However, it is not suitable for use in environments such as the Terraario meeting room because such low signals can not often be detected by commercial receivers.

High-sensitivity signal processing obscures high-frequency fading effects. If such effects exist, they must be detected by other means. Due to extremely weak signal levels, none of the Terraario data can be analyzed with integrations shorter than 1 s, and some of the data requires more than 5 s integration. The stronger Tube data may be analyzed with shorter integration periods. That approach is presented in Section 6.4. More detailed analyses of certain signals will be conducted in following sections, including examination of their characteristics in the correlation code-frequency search space.

6.3 Position and Measured Range Errors

High-sensitivity techniques have successfully detected signals from all PRNs in the Tube environment, and for a large fraction of the available PRNs and epochs in the Terraario data set. For a static receiver, advanced techniques can thus be used to detect weak signals and partially combat the availability degradation caused by the indoor propagation channel.

The errors which affect GPS positioning performance are well-known, and have been discussed in Chapter 2. Therefore, observing the nature of GPS performance degradations using various integration times and discriminator techniques provides information on the most significant types of signal error effects being caused by the GPS-indoor channel. Specifically, it should be possible to determine whether performance is degraded primarily due to low SNR or due to NLOS distortion of the correlation function.

6.3.1 Analysis Techniques

The post-mission analysis tool allows measurement of the C/A code correlation peak with arbitrarily small resolution. If desired, the actual peak of the distorted, noise-affected function may be detected directly (with some error only due to measurement resolution), rather than using standard code phase discriminators. Analyses to evaluate the indoor channel effects will take advantage of this fact.

1) Least-Squares Position Estimation with Peak Detection

Pseudoranges are measured with direct peak detection using various integration periods. A standard least-squares adjustment algorithm is used to determine position epoch-by-epoch. Position measurements and residuals are evaluated for correspondence to SNR and satellite position, and the performance statistics discussed.

2) Least-Squares Position Estimation with Non-Coherent Discriminator

Correlation peaks are measured at early, prompt, and late discriminator locations with various chip spacing, and the code phase estimated using a standard non-coherent discriminator. The least-squares adjustment is again used to estimate position, and results compared with the positions obtained with direct peak detection.

3) Estimated Pseudorange Error Evaluation

Precise rover positions are not known, but may be constrained to estimated positions. Using estimated truth positions, the errors in pseudorange measurements at each epoch are calculated after removal of receiver clock effects. These measurements provide an estimate of how much overall impact the indoor propagation channel has on the C/A code correlation peak position and shape. These are *estimated* pseudorange errors for two reasons: First, the truth position used to calculate geometric ranges is only estimated. This causes an inherent bias on any EPE, but it is a constant bias throughout the period of test. Second, the true receiver clock at any epoch cannot be precisely determined. The clock is therefore constrained to a certain value, introducing a possible constant bias as well as a time-varying effect depending on the stability of the clock. The level of this effect is discussed prior to presentation of EPE results.

6.3.2 Reference Position Estimation with Peak Detection

Reference positions calculated with epoch-by-epoch least-squares adjustment are presented in this section for both the Tube and Terraario reference data sets. A single method of code phase measurement, direct peak detection from 200 ms integration, has been used; this method provides excellent position results, sufficient to estimate an average truth position and provide a basis for comparison with both rover data sets. A modified Hopfield tropospheric adjustment has been applied to pseudoranges using average daily high temperature and humidity for Tampere in September (Hoffman-Wellenhof et al., 2001). Other than this adjustment, no corrections were used. The coordinates (0,0) in Figure 6.8 represent the reference antenna position provided by Nokia. Clock estimates shown in Figures 6.9 and 6.10 are expressed in metres with the mean value removed.

The two reference data sets show a position bias about 2 m east, 4 m south, and 9.5 m up from the given antenna position; these errors are within the specifications for L1 C/A code range error as defined in the GPS standard positioning service performance standard (USDoD, 2001) when accounting for dilution of precision (DOP)

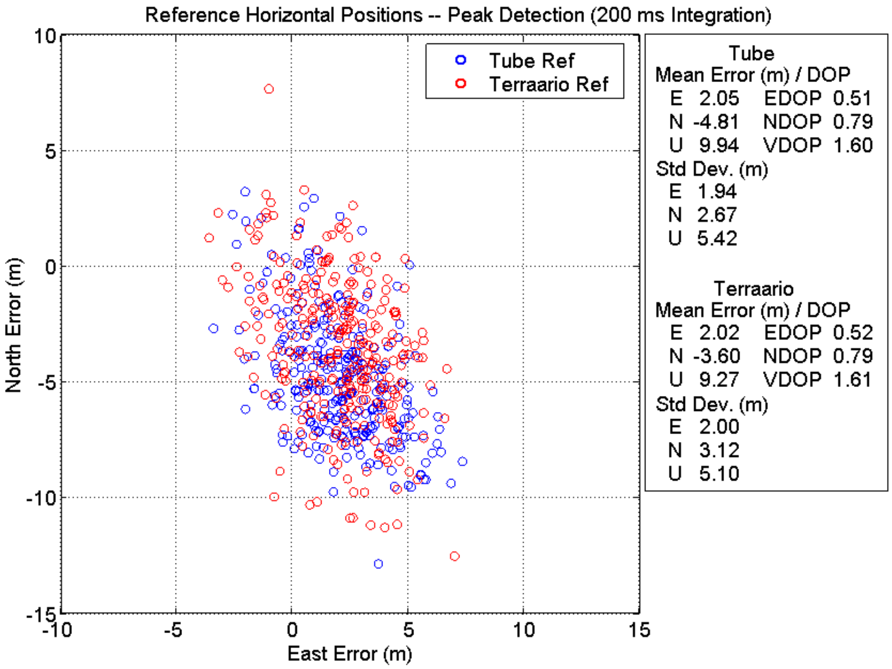

Figure 6.8: Reference Horizontal Positions

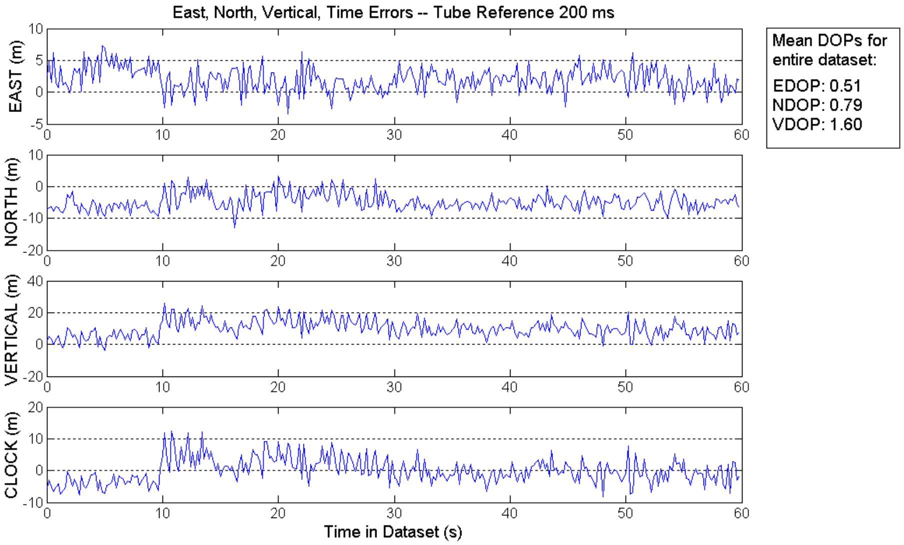

Figure 6.9: Tube Reference Error Time Series

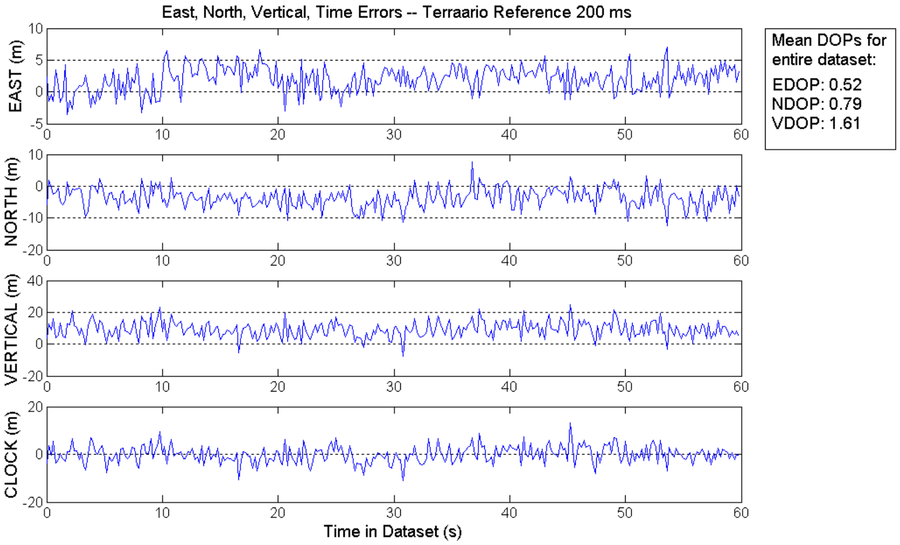

Figure 6.10: Terraario Reference Error Time Series

levels. Additionally, the antenna position is known with only about 5 m accuracy, and other propagation conditions such as atmospheric effects and orbital errors are not accounted for in the solutions. The source of the bias is not important for further analyses.

Time series data for the Tube reference data set shows a jump in position error in all four dimensions at about 10 s. The cause of this is unknown. As expected with GPS geometry, horizontal errors are significantly smaller than vertical errors. Clock errors are similarly worse than horizontal errors, but are not as bad as vertical ones.

6.3.3 Tube Rover Position Estimation

Position results for two integration periods using three different code phase estimation techniques are presented in Figures 6.11 and 6.12. Integration periods of 1000 ms and 200 ms are compared, with code phase estimation by direct peak detection and non-coherent discriminators with 0.1 chip and 0.5 chip spacing. Because the rover truth position is unknown, east and north coordinates are shown as 'errors' relative to the given reference antenna position. Vertical and clock errors are shown in the time series data of Figures 6.13–6.14, and are noticeably worse than the horizontal errors to approximately the same degree as the reference vertical and clock errors were worse than the horizontal.

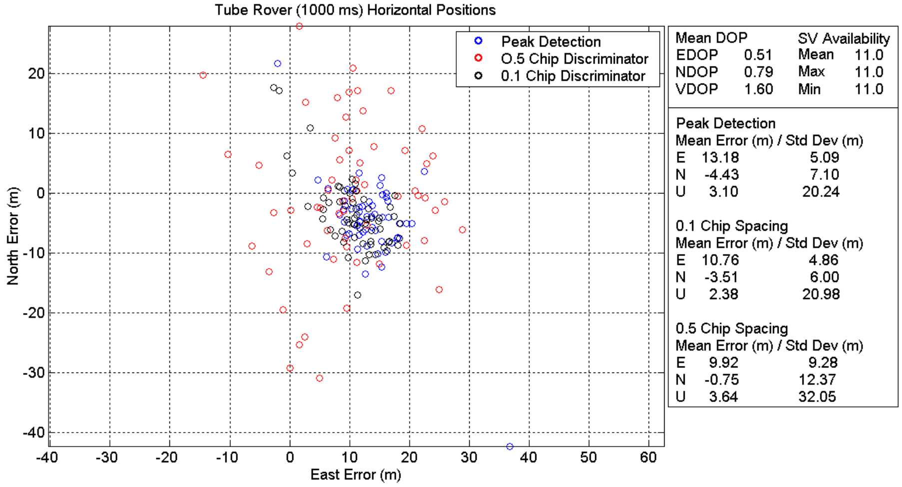

Figure 6.11: Tube Rover Horizontal Positions—1000 ms Integration

Comparison of standard deviation statistics shows significant improvement when using direct peak detection as opposed to a 0.5 chip-spacing non-coherent discriminator. On the other hand, position estimated using a 0.1 chip-spacing discriminator gives approximately the same performance as direct peak detection. While the 0.1 chip discriminator has not been applied to the 200 ms data, the relationship between the 0.5 chip positions and those estimated by peak detection is similar to the 1000 ms data. The major drawbacks of using a narrower correlator spacing include increased sensitivity to dynamics, and larger bandwidth requirement. In real-time

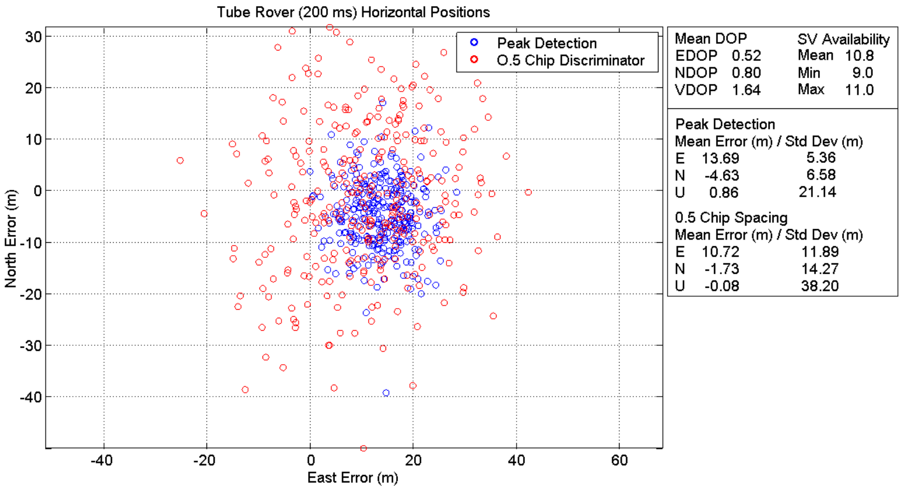

Figure 6.12: Tube Rover Horizontal Positions—200 ms Integration

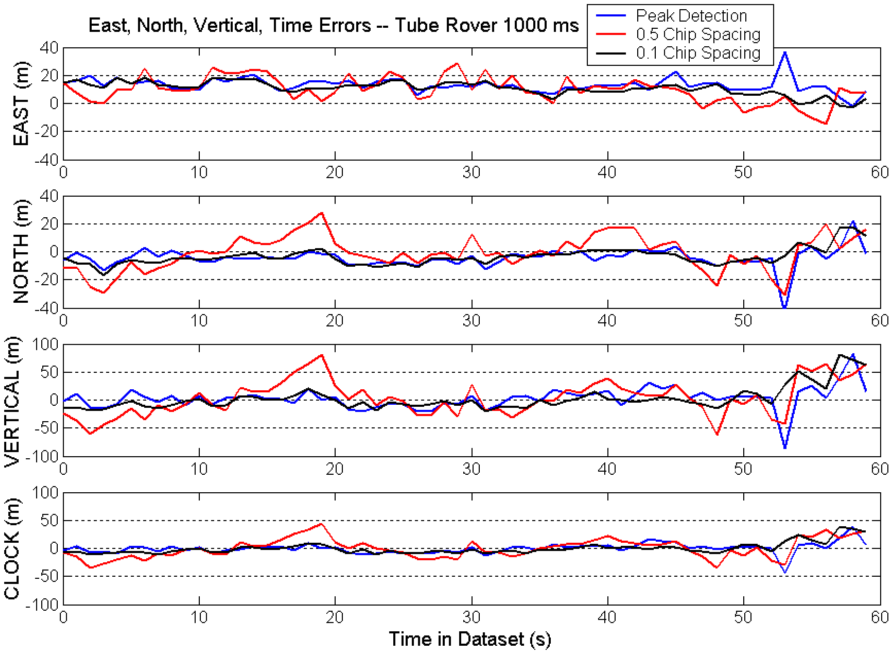

Figure 6.13: Tube Rover Time Series Position Errors—1000 ms Integration

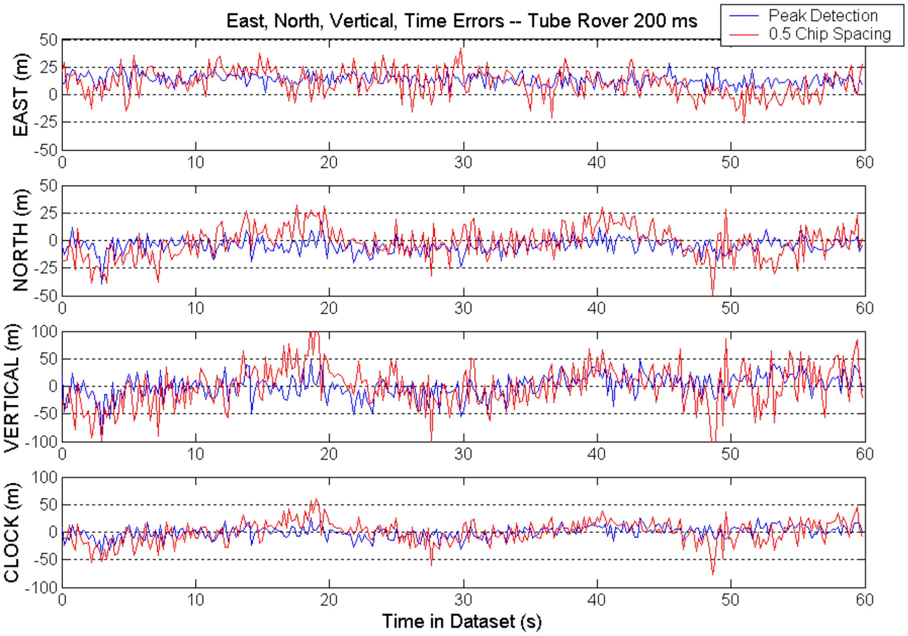

Figure 6.14: Tube Rover Time Series Position Errors—200 ms Integration

applications, these would be serious factors limiting accuracy.

Interestingly, position error statistics using direct peak detection are very similar for both 1000 ms and 200 ms integration times, despite approximately 7 dB difference in SNR. Meanwhile, the results using a 0.5 chip discriminator have somewhat higher standard deviation for the lower-SNR signals. This is seen in the time series data as both higher maximum errors and faster variations in the 200 ms data as opposed to the 1000 ms data. The overall trends remain the same regardless of integration time, however. The most notable exception is the large error in the 1000 ms integration at time 53 s (peak detection) that is not present in the shorter period. This most likely indicates a PRN measured with a large error for some undetermined reason. In fact, further results examining estimated pseudorange error will show significant errors at that epoch for both PRNs 10 and 29, likely yielding the large position error.

The good performance of the peak detection method for both integration times, and the degraded performance using a standard 0.5 chip discriminator may indicate that much of the position degradation in this environment is caused by distorted correlation functions, rather than simply the low SNR of the signal. Low SNR can be mitigated with long integrations. NLOS peak distortion is typically only mitigated by technologies such as the narrow correlator spacing or antenna technologies.

6.3.4 Terraario Rover Position Estimation

Horizontal position results for the Terraario rover data set measured with 5000 ms integration are plotted in Figure 6.15. The non-coherent discriminator was designed with 0.45 chip spacing, rather than the 0.5 chip spacing used previously. This is a result of using several correlators spaced by 0.15 chips, rather than 0.05 chips as in the Tube data set, in order to measure signals with reasonable processing times. Fading data was not presented for the initial 1000 ms power measurement because of the low availability of signals above detection threshold. However, the horizontal positions calculated from the available data have been calculated and are presented in Figure 6.16 for comparison with the results from the 5000 ms case.

Position results from the Terraario rover case for 5000 ms and 1000 ms cases provide a good contrast of position results as a function of integration time. The most important difference evident is satellite availability, represented by DOP values. Of the 20 epochs for which a position was available in the 1000 ms case, average EDOP was similar to the EDOP of the 5000 ms integrations, being less than 1 on average. However, average NDOP and VDOP measured with lower satellite availability were 4.16 and 7.50 respectively, which are approximately 4 and 3 times worse than these

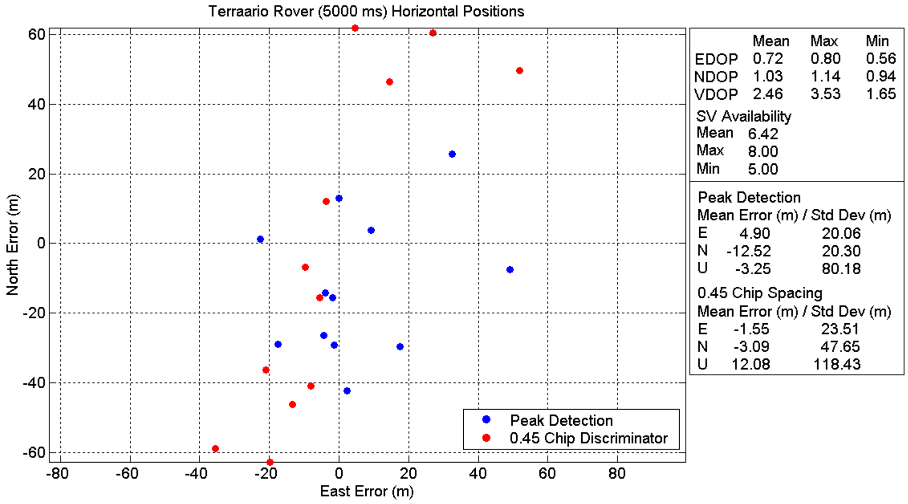

Figure 6.15: Terraario Rover Horizontal Positions—5000 ms Integration

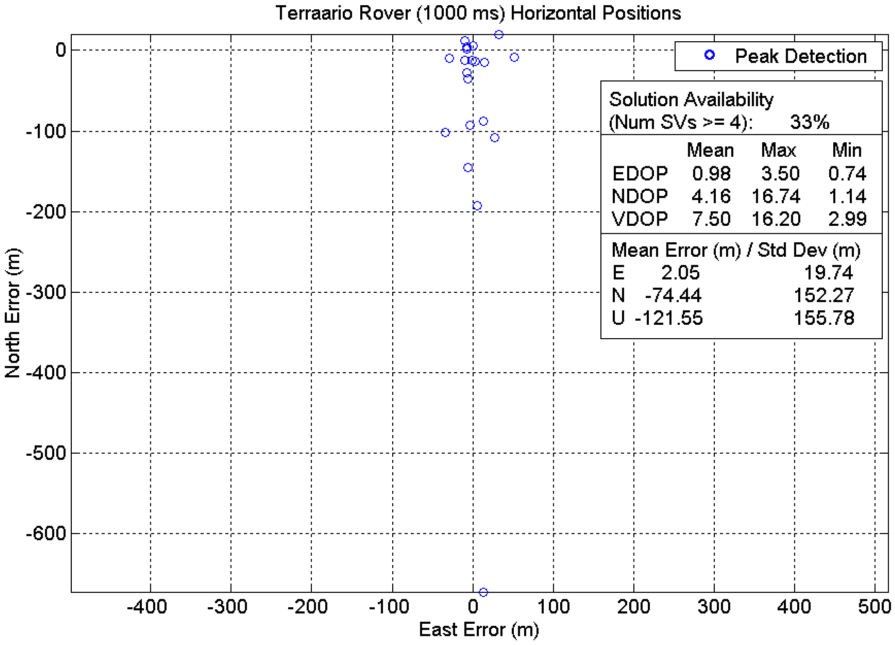

Figure 6.16: Terraario Rover Horizontal Positions—1000 ms Integration

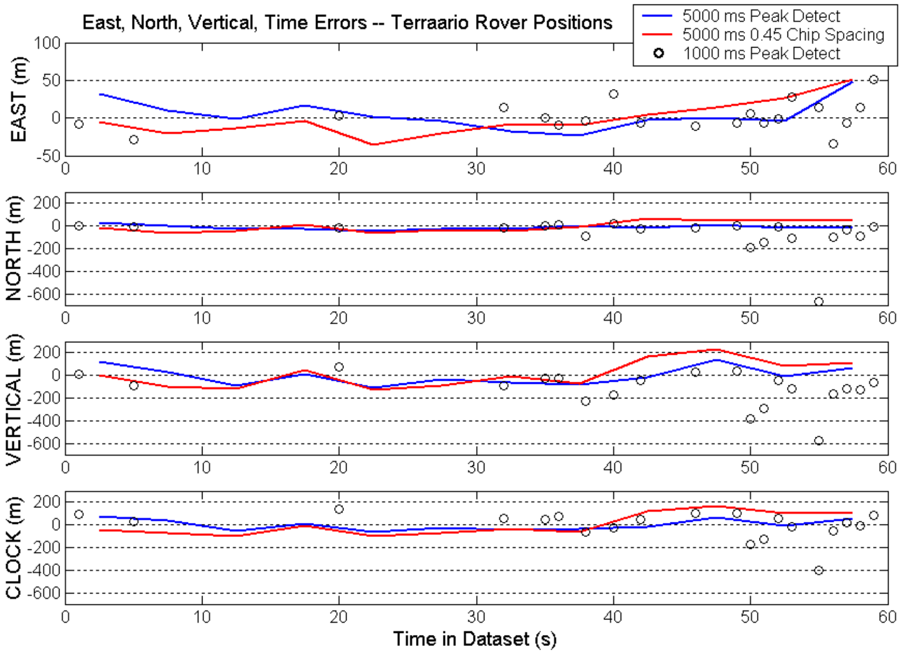

Figure 6.17: Terraario Rover Time Series Position Errors

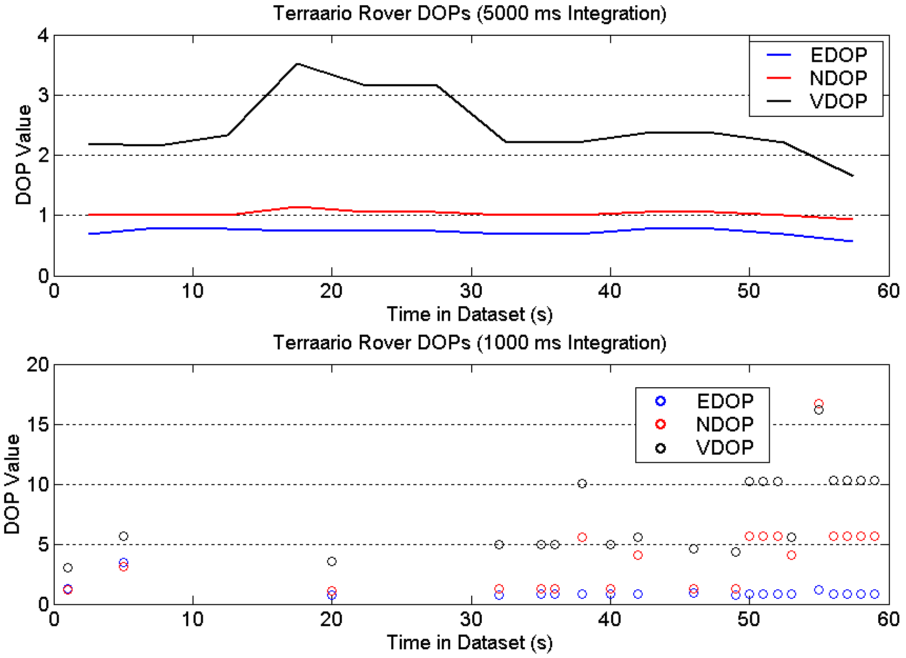

Figure 6.18: Terraario Rover DOPs vs. Time

values in the 5000 ms case. Maximum NDOP and VDOP both exceeded 16.0 in the 1000 ms case, which is a significant degradation compared to maximum NDOP of 1.14 and VDOP of 3.53 in the 5000 ms case. These degradations are clear in the time series plots of Figure 6.17 when compared with the DOPs of Figure 6.18.

The overall position statistics are significantly worse in the lower-SNR case. Comparing the results from the peak detection method for both integration times, the standard deviation of the position errors is significantly worse in the case of shorter integration. East standard deviation is approximately the same in both cases, with north standard deviation approximately 7.5 times worse and vertical standard deviation approximately 2 times worse in the shorter integration case. Also, the mean position in the east direction is approximately the same in both cases, with the means in the north and vertical directions significantly different. Based on the similar performance in the east direction, and highly degraded performance in north and vertical directions, it seems that the majority of position-domain performance degradation in the Terraario environment is due to satellite availability and geometry, rather than signal degradations causing pseudorange measurement error. The estimated pseudorange errors will be examined further in the following section.

6.3.5 Estimated Pseudorange Error (EPE)

EPE Calculation

Pseudoranges are measured as the difference between GPS time of week when the signal was transmitted and receiver time when the signal is received. The pseudorange P in metres is found as

$$P = c \cdot (t_{rx} - TOW_{tx}) \tag{6.6}$$

where c is the speed of light, t_{rx} is receiver time at reception, and TOW_{tx} is measured GPS time of week. The pseudorange consists of three main elements: geometric range, clock error, and propagation errors.

$$P = \rho + (c \cdot dt) + \epsilon \tag{6.7}$$

where ρ is geometric range, dt is clock error, and ϵ represents all other errors, including noise, atmospheric errors, measurement errors, and multipath.

Receiver clock error is common to signals from all SV measurements at a given epoch. If true position is known, ρ may be determined for all SVs. Thus, by rearranging Equation 6.7 and constraining position, propagation and measurement errors are isolated:

$$\epsilon = P - \rho - (c \cdot dt). \tag{6.8}$$

Clock error dt cannot be precisely determined, however. Least-squares adjustment causes certain biases to be absorbed in the clock parameter including some multipath and atmospheric errors. The precision of the clock estimate over time is therefore determined both by the precision of the measurements and the stability of the clock itself. If it is assumed that true receiver clock errors are small compared to other errors (ϵ), the changes of ϵ over time on a given PRN may be observed by setting dt to a constant value. Comparisons between PRNs are not representative of the differing pseudorange errors because the clock absorbs a differing amount of error from each PRN. However, relative changes may be observed between PRNs using the constant clock error approximation, if the stability assumption above holds true.

Receiver Clock Stability

The receiver clock in this case is based on the sampling frequency of 9.885 MHz. The stability of this frequency reference is considered.

Timing Jitter The Datum ET-6000 oscillator phase noise parameters were given in Table 5.5. The majority of phase noise occurs at less than 10 Hz offset from the nominal frequency, with the phase noise at 1 Hz being -94 dBc/Hz and dropping to -115 dBc/Hz at 10 Hz offset. Linearly interpolating a phase noise characteristic between the values given in Table 5.5, RMS timing jitter does not exceed 10^{-11} s. The equivalent range effect of this jitter is 30 cm from sample-to-sample. This level of error will not significantly affect EPE measurement over time, as other errors are much larger and will obscure the jitter effect.

Long-Term Time Stability Over 60 s, the stability of the sampling clock is considered. Allan standard deviation for the ET-6000 is between 2×10^{-11} and 4×10^{-11}. Multiplying the larger of those two values by 60 s gives the approximate one-sigma timing error over 60 s as approximately 2.4 ns, or less than 1 m equivalent distance. A change in EPE on any given PRN on the order of 1 m over 60 s might therefore be a clock effect. Changes exceeding this level are likely due to propagation effects including atmospheric disruptions and multipath.

Based on the above, it is reasonable to use a constant clock bias to determine EPE. The clock bias is taken as the average clock error from the least-squares solutions. It therefore includes true clock bias and a bias transferred from pseudorange errors. It will therefore not be possible to compare pseudorange errors between PRNs directly, but changes in estimated pseudorange error over the course of the data set will be observable. Variations at levels greater than about 1 m are thought to be valid.

EPE Results From Peak Detection Estimates

Figures 6.19–6.20 present estimated pseudorange errors for the two reference data sets, and the higher-SNR Tube and Terraario rover data sets (1000 ms and 5000 ms respectively). Each data set has had its clock bias determined individually, so absolute comparisons of EPEs are not completely meaningful. Additionally, the positions of the Tube and Terraario rovers were only estimated. In the Tube case, the estimate is based on the average of least-squares positions. In the Terraario case, the position is estimated as being vertically 6.0 m below the reference position.

EPE Results From Code Phase Discriminator Estimates

The EPE data, calculated using the same clock biases and truth positions as were used for the first EPE calculations reported above, are presented in Figures 6.21–6.22 for the pseudoranges calculated using non-coherent code phase discriminators. The results shown are for a 0.5 chip discriminator for the Tube data set, and a 0.45 chip discriminator for the Terraario data set.

Discussion of EPE Results

The measurement of EPE is believed to isolate major errors caused by propagation and measurement errors. Reference EPE data consists primarily of measurement uncertainty, due to the limited resolution used for peak detection (0.02 chips, or approximately 5.9 m), and atmospheric propagation delays. These errors are less than 10 m. Rover errors in excess of that value are indicative of further measurement errors and effects of the propagation channel.

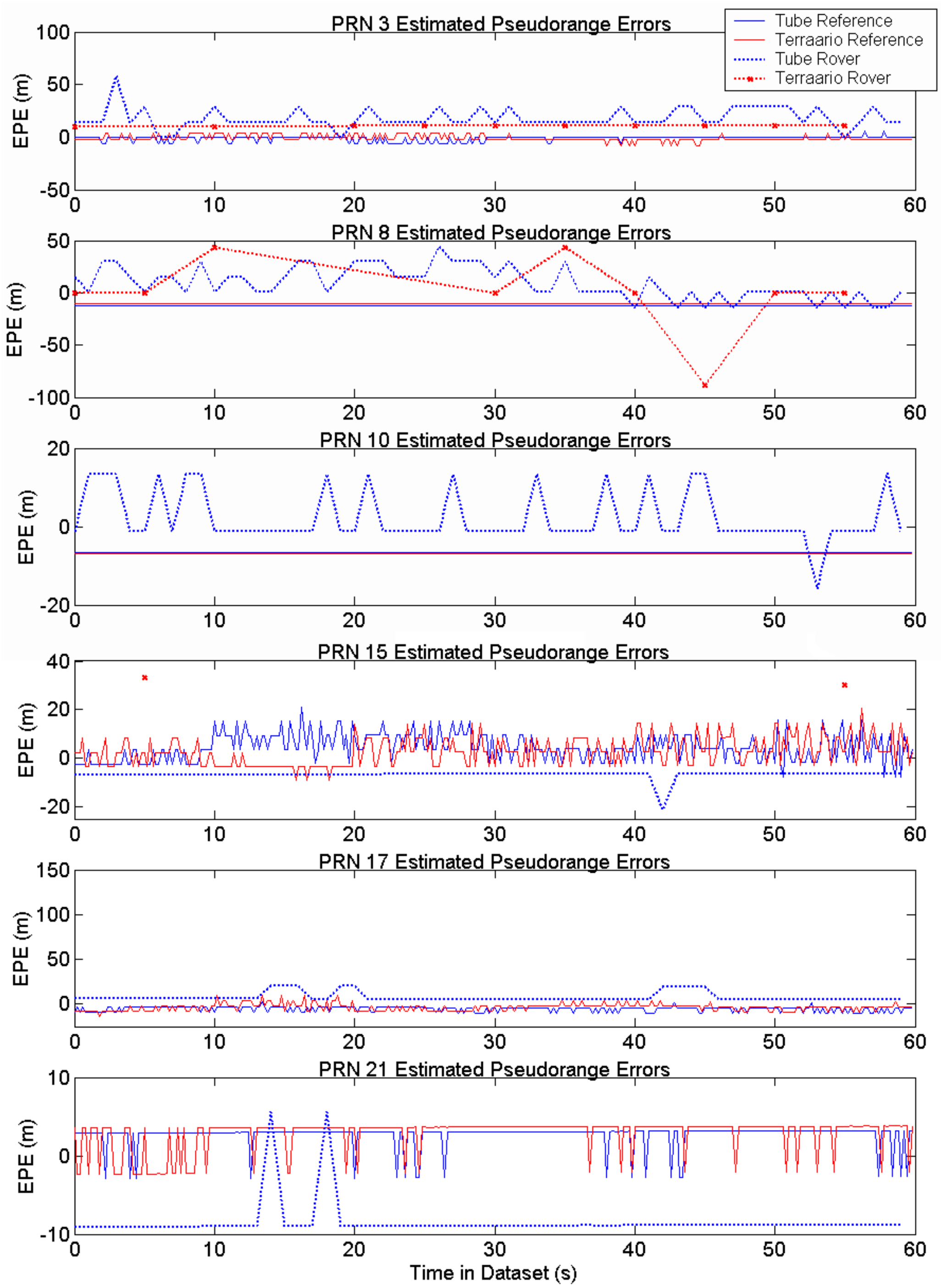

Figure 6.19: Estimated Pseudorange Errors (Peak Detection)—PRNs 3–21

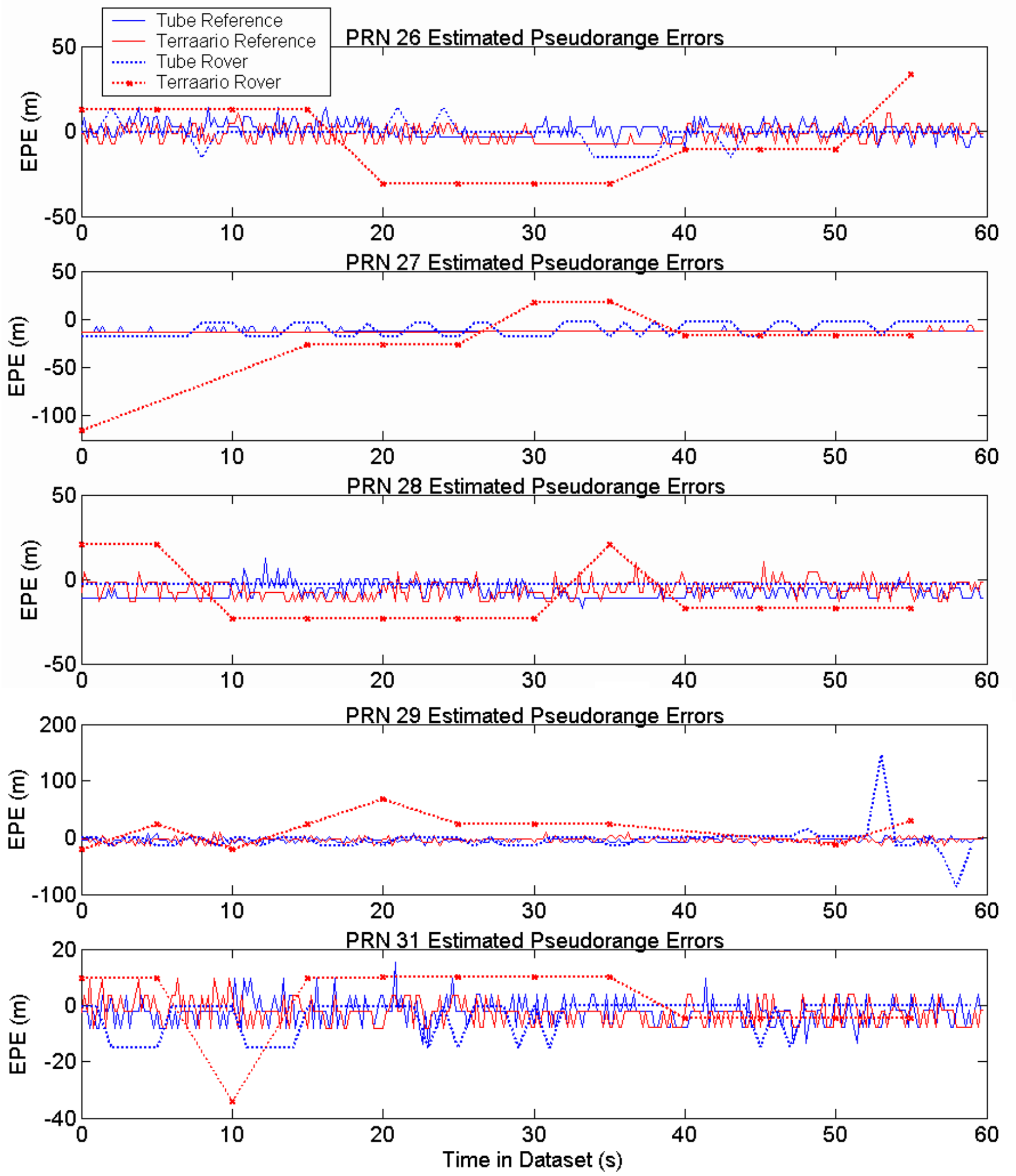

Figure 6.20: Estimated Pseudorange Errors (Peak Detection)—PRNs 26–31

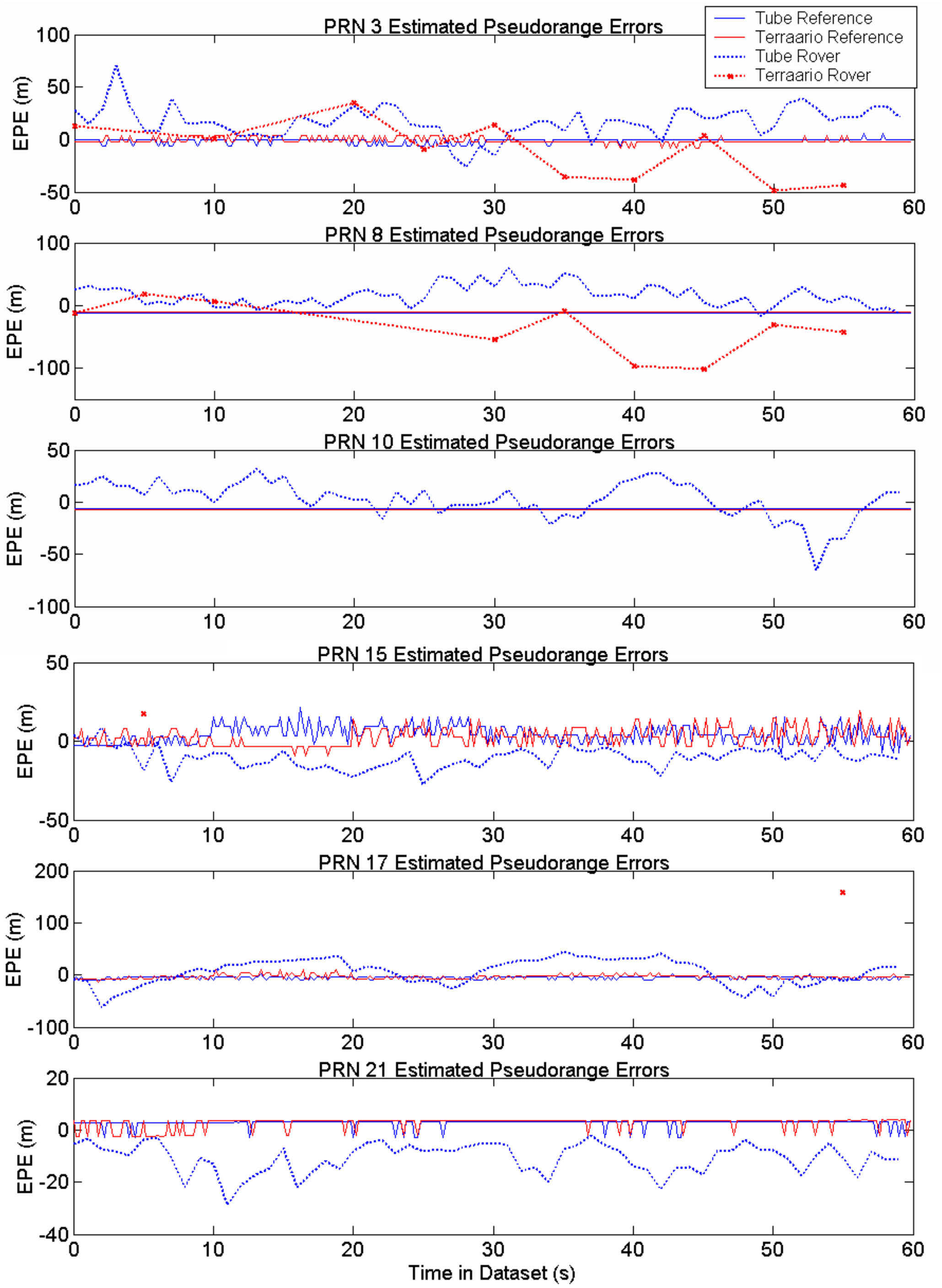

Figure 6.21: Estimated Pseudorange Errors (Non-Coherent Discriminator)—PRNs 3–21

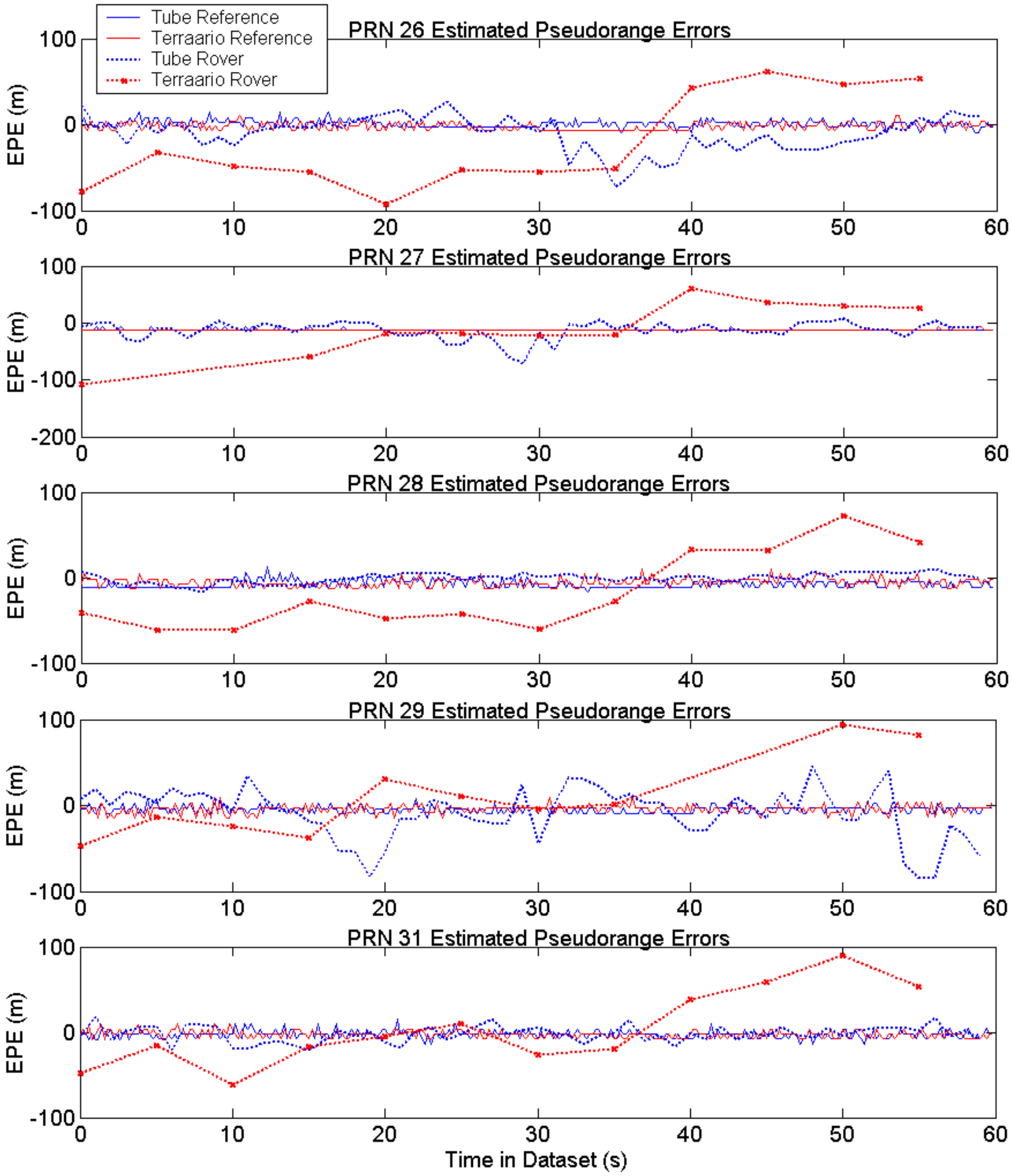

Figure 6.22: Estimated Pseudorange Errors (Non-Coherent Discriminator)—PRNs 26–31

A major motivation for measuring EPE was the potential to identify changes in pseudorange, possibly representative of changing multipath conditions. The results from analysis of the EPEs are presented for the Tube and Terraario environments separately.

Significant Results from Tube Rover Few major changes in EPE were observed on Tube data sets using either peak detection or discriminator techniques. Overall EPE average levels and trends using the two methods were similar for all PRNs. The strong fading events of PRN 21 are not correlated with large changes in EPE. It is unlikely, therefore, that the fades were caused by sudden long-delay multipath acquisition and interference.

Significant Results from Terraario Rover Among those PRNs for which signals were measured in the Terraario environment, EPE characteristics vary somewhat. The EPE for PRN 3 measured with peak detection is stable, while that measured with the non-coherent discriminator is quite variable. No other PRNs show this level of disparity. Potential reasons include higher noise on the early and late discriminators, and time-varying distortion of the correlation function due to weak multipath.

Overall trends of EPE observed for PRNs 8 and 27 are similar using the two methods. These are high-elevation satellites that show heavy fading. While the EPE results do not directly support the postulate that these are direct, attenuated signals, the similarities in results from both methods indicate that their correlation functions are not significantly distorted from the nominal shape.

PRNs 26, 28, 29, and 31 have similar trends. The EPEs measured using a non-coherent discriminator all increase significantly toward the end of the data set, whereas the EPEs measured with the peak detection technique do not, except for the final data point of PRN 26. Similarities among four PRNs may indicate a systemic error in the measurement method, or some commonality yet to be identified. These PRNs are not similar in their overall fading behaviour, and have widely distributed azimuths. It is also possible that this behaviour is due to random noise.

6.3.6 Discussion

Position has successfully been computed in both indoor environments despite signals in excess of 40 dB below open-sky levels due to fading and shadowing. Excellent accuracy is obtained using a direct measurement of the correlation peak code offset. Accuracy is most dependent on measurement resolution and satellite availability. Received C/N_o has a lesser effect, as long as processing techniques can be used to boost SNR above a good detection threshold.

Comparison of results using the peak detection method and a non-coherent discriminator shows some degradation with a wider correlator spacing. This is an effect of lower SNR on early and late correlators and some amount of multipath distortion. It is unclear which effect is more significant, but similarities in results with various integration times indicate that code peak distortion may be a more significant effect. Interestingly, the degradations have a smaller effect than may have been expected given previous research of indoor positioning. Therefore, while peak distortion and measurement noise have a negative effect, these factors are not as significant to positioning as satellite availability.

Improving Position Measurement

Measurement Resolution The techniques used to measure position may be improved through various techniques. First, limited correlator resolution was used in these tests to ensure reception of the signal with reasonable processing time. This resolution of 0.05 chips, or approximately 15 m, causes some measurement error in peak detection techniques. Improved measurements may be obtained with narrower correlator spacing. To date, this has not been attempted due to processing time issues.

DGPS The potential to apply differential GPS (DGPS) techniques to improve indoor performance is limited. Based on the EPE data, corrections derived from reference positions are at levels lower than 10 m for most PRNs, with none exceeding 20 m. In contrast, there are two clear classes of pseudorange error observed on rover data. First, some PRNs have rover EPE comparable to the level of reference EPE. Application of DGPS corrections may have a significant impact on position estimates in these cases. Second, a large number of PRNs have EPE levels far in excess of the reference corrections. Application of DGPS corrections would have no significant impact in these cases.

Instances of rover EPEs comparable to reference EPEs are limited to measurements made with the peak detection technique. For example, PRN 10 in Figure 6.19 has reference EPE bias of approximately -7 m, and rover EPE ranging from -15 m to +14 m. While the levels are comparable, it is apparent that application of a +7 m correction to the rover pseudoranges would provide a significant positioning impact, but not necessarily a positive impact. The differing bias levels indicates either that some error affects the rover, but is uncorrelated with those errors affecting the reference, or that the estimated rover position is badly biased. This cannot be verified without a precise *a priori* truth position for the rover, rather than one based on an average.

Most EPEs measured with the non-coherent discriminators are at levels much higher than the reference EPEs, with the exception of Tube PRNs 28 and 31. The EPEs are not correlated in either magnitude or direction, indicating that the bulk of the ranging error indoors is due to uncorrelated errors, namely noise and multipath. Application of corrections to these pseudoranges could be used to remove atmospheric and orbital errors, but would be insignificant in relation to the overall errors induced by the indoor channel.

6.4 Targeted Analysis of Selected Signals

Based on fading, position, and pseudorange characteristics observed in the preceding analyses, a selection of signals is analyzed further. The Tube data set is of high enough strength to allow a higher-rate analysis of fading. The signals are received with 200 ms coherent integration, increasing fading data to 5 Hz. Similarities and differences to the data measured with 1000 ms integration time are examined.

Specifically, the large periodic fade events of PRN 21 are targeted for identification of any unusual characteristics. High-resolution correlation functions in the code-frequency ambiguity domain are compared before, after, and during the fading events to identify possible causes.

6.4.1 High-Rate Power Measurement (Tube)

Tube rover C/N_o is presented at 5 Hz in Figures 6.23–6.24, with statistics in Table 6.3. Based on the defined SNR detection threshold of 11.6 dB, the C/N_o detection threshold using 200 ms integration is 18.6 dB-Hz.

Trends in C/N_o observed in the initial fading measurement remain in the higher rate data. However, the higher rate data shows fades of up to 10 dB that were not detected in the preliminary analysis due to their short coherence times. Higher standard deviation of the measurements reflects this. Fading at rates higher than 5 Hz has not been examined. The results from the 5 Hz test indicate shorter fading coherence times than 200 ms. Based on the available data, it is not possible to determine fading behaviour at rates much higher than 5 Hz in the Tube environment because the loss of processing gain would leave many of the observed signals below the valid detection threshold defined in Chapter 6. The presence of both high-frequency (higher frequency than can be measured) and low-frequency fading characteristics adds complexity to any model development process.

Probability Distributions

Availability of up to 300 data points above threshold gives an opportunity to examine probability distributions of the signal envelope. Over such a short period, the indoor signal envelope shows some similarity to a Rician or Loo's distributions in certain cases for which the long-term trend is stable, but no identifiable trend in cases for which trends are observed over 10 s or longer. The distribution for PRN 3 is shown in Figure 6.25 along with a similar Rician envelope. Conceivably, a Loo distribution could provide a similar match. Conversely, other PRNs show no resemblance to

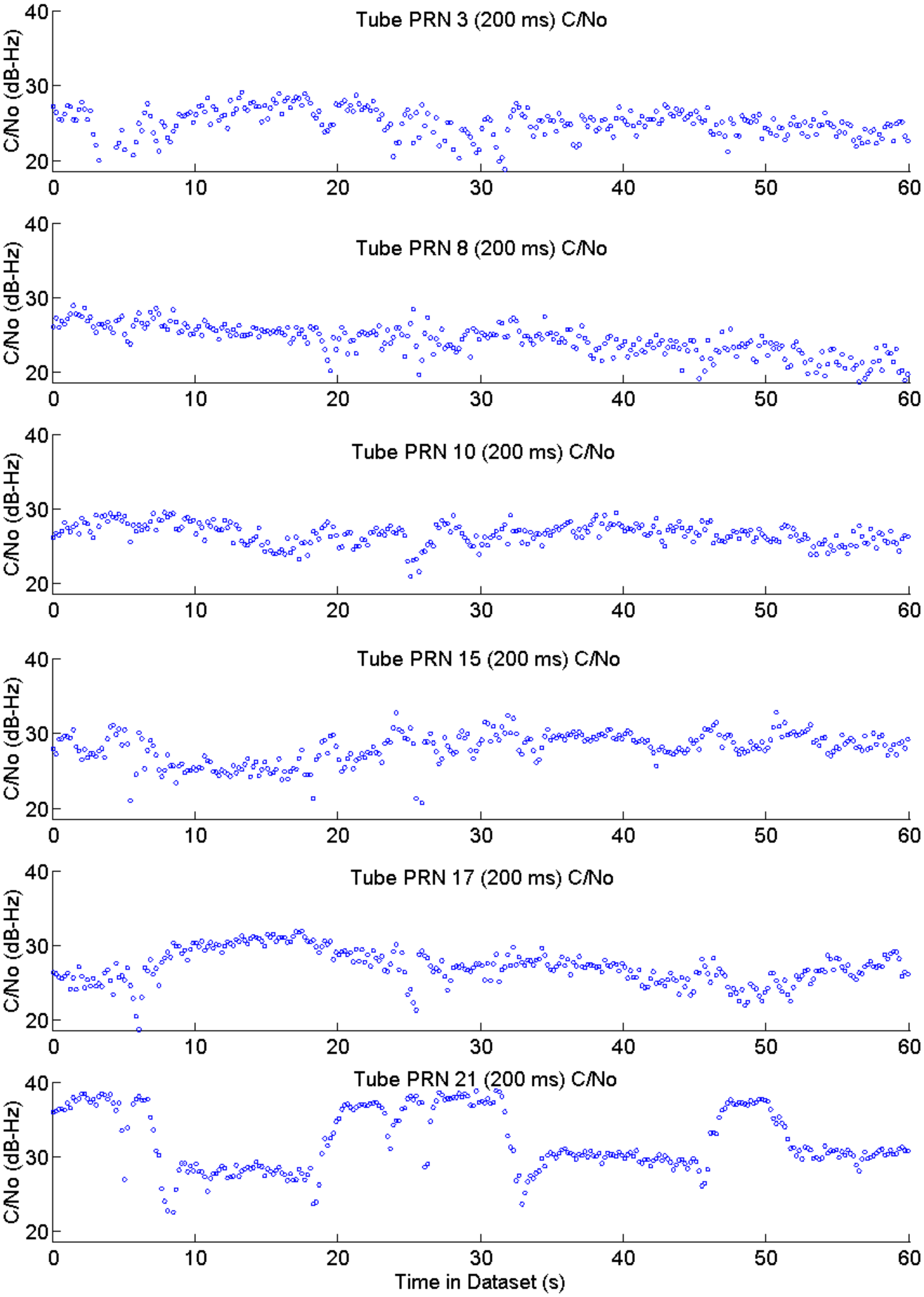

Figure 6.23: Tube Rover C/N_o at 5 Hz—PRNs 3–21

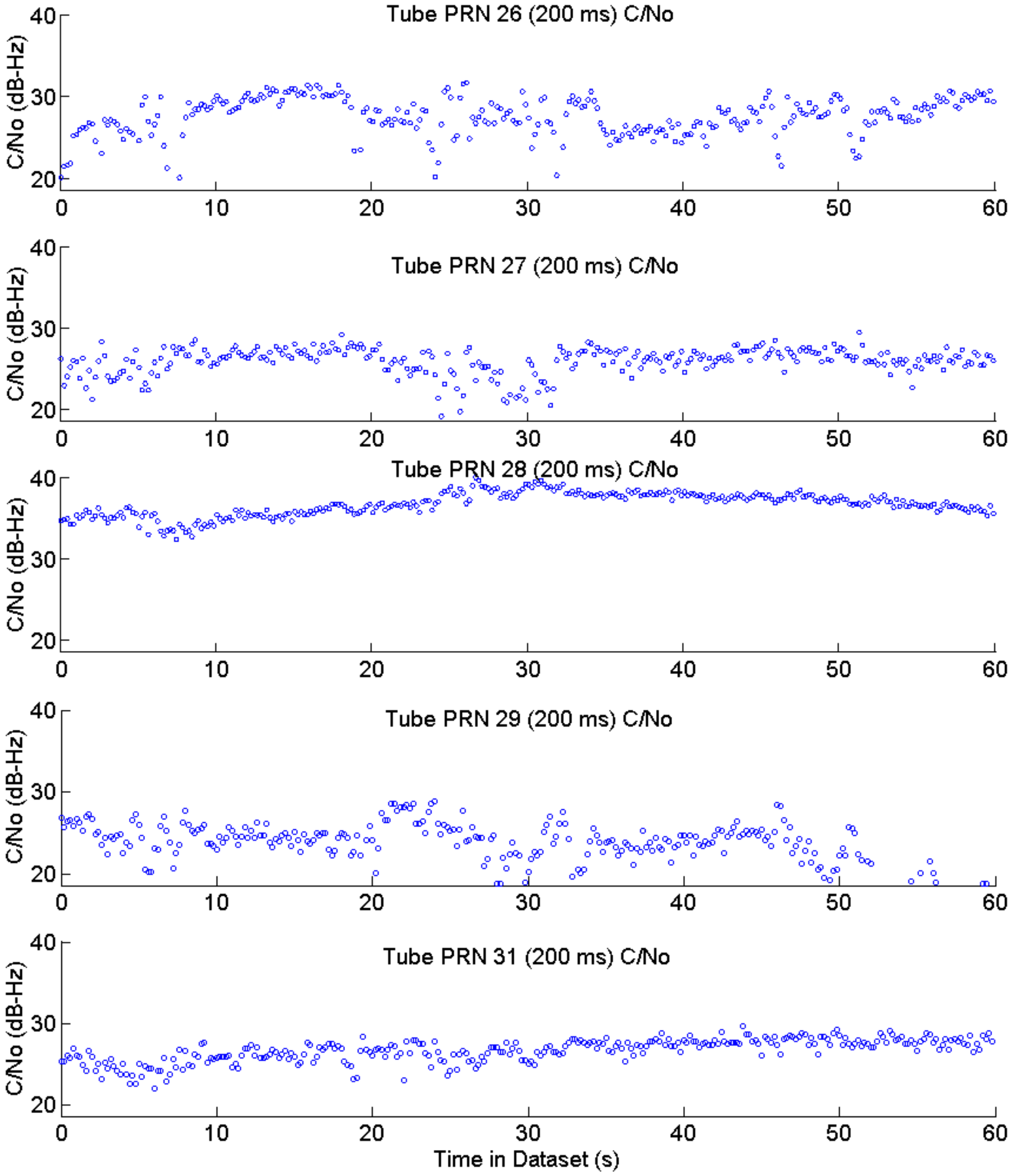

Figure 6.24: Tube Rover C/N_o at 5 Hz—PRNs 26–31

PRN	Mean (dB-Hz)	Max (dB-Hz)	Std Dev (dB-Hz)	% Above Threshold
3	25.2	29.2	1.86	96.7
8	24.4	29.0	2.04	99.3
10	26.7	29.6	1.42	100.0
15	28.1	32.8	2.05	99.3
17	27.2	32.0	2.27	100.0
21	32.2	40.1	4.11	99.7
26	27.6	31.7	2.32	97.7
27	26.0	29.5	1.67	99.7
28	36.7	39.9	1.43	100.0
29	24.1	28.9	2.13	87.7
31	26.7	29.7	1.40	100.0

Table 6.3: Tube Rover High-Rate C/N_o Statistics

existing probability distributions, most likely due to their long-term trends. The unusual trend of PRN 21 clearly causes a bimodal distribution, but others such as PRN 29, shown in Figure 6.26, show no particular distribution even though the time-series characteristics are qualitatively similar to those of PRN 3. While true fast fading might therefore be represented by common statistical models, any long-term trends must evidently be accounted for with alternative methods.

6.4.2 Examination of PRN 21 Fading Events

The signal strength of PRN 21 measured at the rover undergoes significant changes at various points within the Tube data set. Specifically at times 6–8 s, 18–20 s, 31–33 s, and 45–47 s. We wish to identify the nature of these changes, and the causes if possible. The following tests were performed:

- High-resolution signal strength measurement during transition times

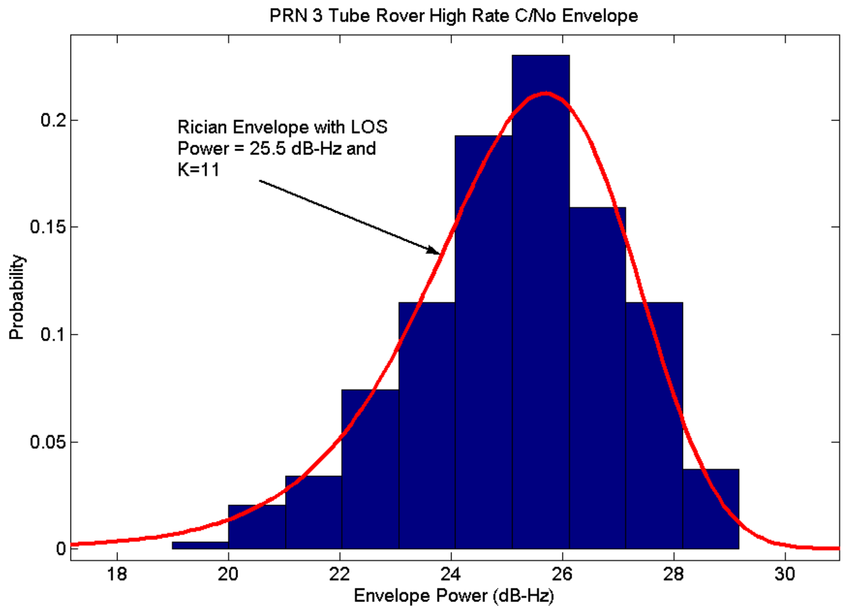

Figure 6.25: PRN 3 Envelope (Tube Rover) and Rician Approximation

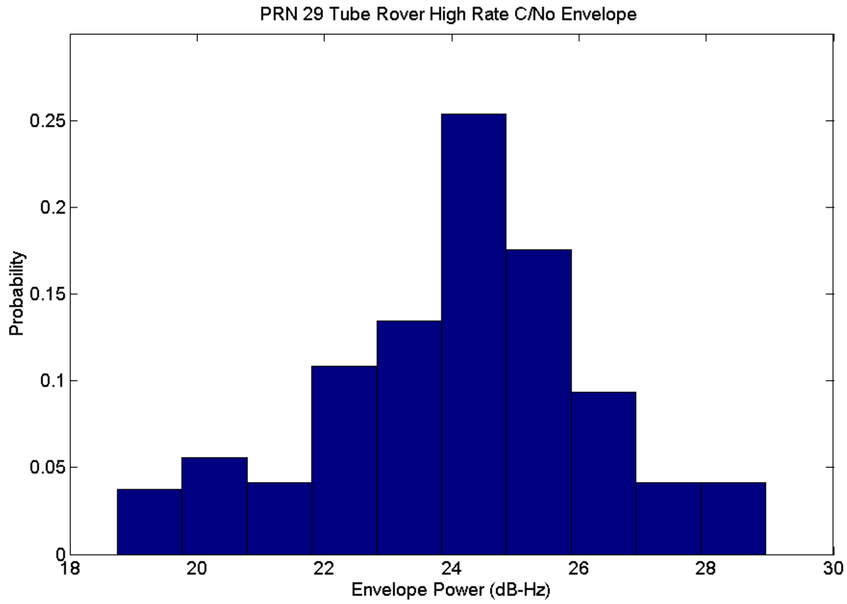

Figure 6.26: PRN 29 Envelope (Tube Rover)

- Correlation peak characterization at high- and low-power epochs
- Observation of correlation peak changes during high-low transition

Fade Events in High Resolution

PRN 21 rover signal was received with a minimum SNR of approximately 20 dB using a 1000 ms integration period. The high-rate fading of 200 ms suffers approximately 7 dB power loss compared to the initial test, giving a minimum power at this rate slightly above the 11.6 dB threshold. The signal strength at 5 Hz during each of the transition epochs identified above is plotted in Figure 6.27 along with the corresponding 1 Hz data from the preliminary fading analysis.

Each instance of rapid signal strength change occurs over 1–2 s, and introduces on the order of 10 dB change in power. During those 1–2 s, the power changes smoothly, rather than very abruptly. This may indicate the slow introduction or removal of a multipath component to the signal. Measurements of EPE and signal phase changes (Section 6.5) do not support this possibility, however. Without further data, it is impossible to determine if the periodicity is a true property of this fading or if it is simply due to random circumstances. To attempt to identify this phenomenon as being due to multipath or not, the correlation peaks were compared in the high- and low-power states. If strong multipath is the cause of the fading, the correlation peak of the signal may be noticeably different in its high state as compared to its low state. Figures 6.28 and 6.29 compare the PRN 21 correlation peak at high- and low-power epochs. The peaks of Figure 6.28 represent eight selected 200 ms epochs between 30.0 and 31.6 s, before a fading event. Those of Figure 6.29 are from epochs immediately after the fading event, from 33.2 to 34.0 s. The latter peaks are

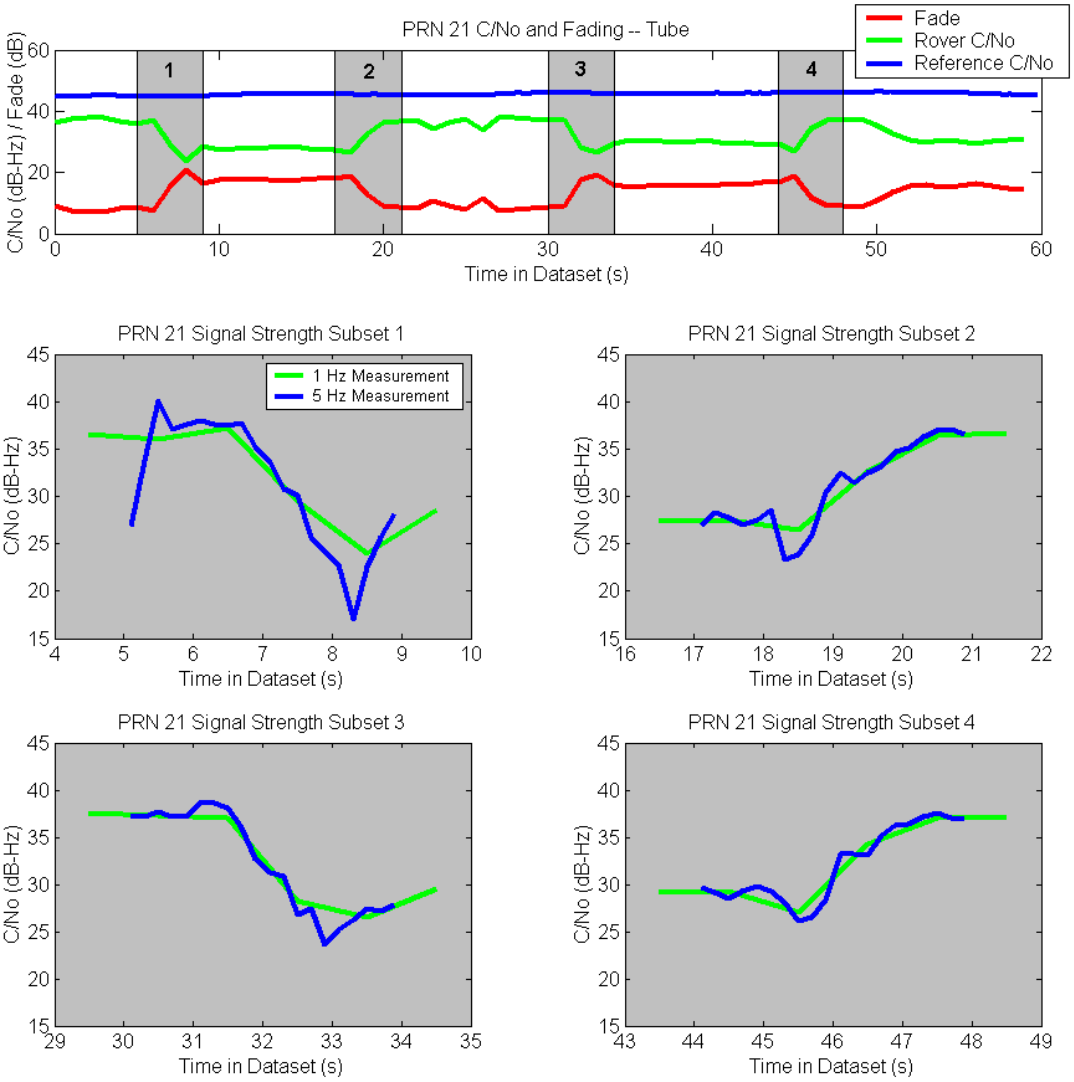

Figure 6.27: Detail of PRN 21 Signal Strength at Selected Epochs

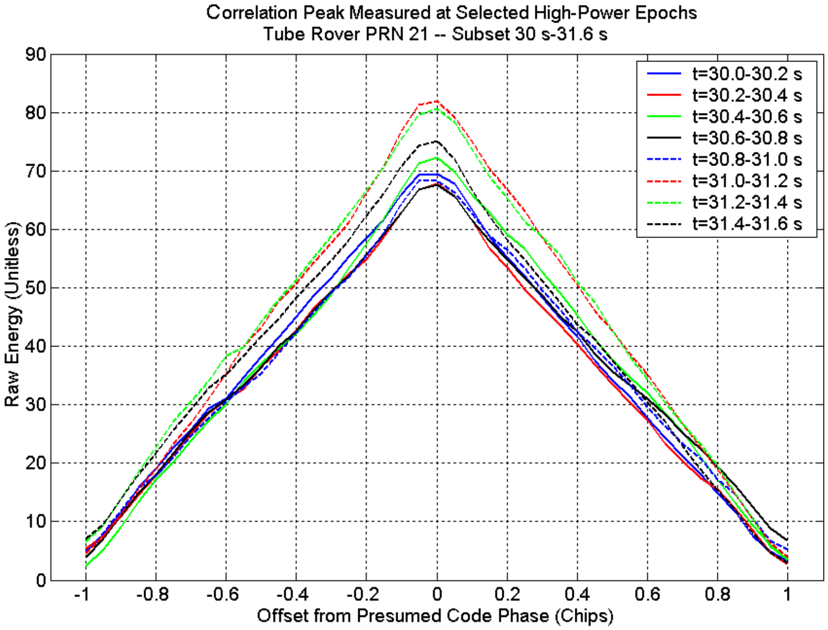

Figure 6.28: PRN 21 Correlation Energy at Selected High-Power Epochs

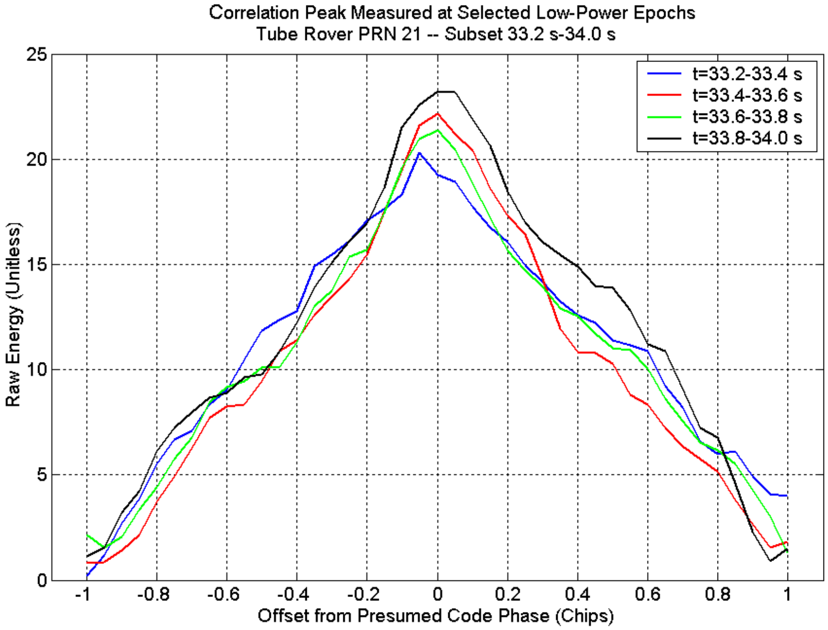

Figure 6.29: PRN 21 Correlation Energy at Selected Low-Power Epochs

distorted by noise, but show no consistent distortion trend. If changing multipath is the source of these fades, it is not identifiable by any means available.

6.5 Doppler and Carrier Phase Channel Effects

The sources of Doppler identified in Chapter 5 were expected to contribute both stable Doppler biases and a level of unpredictable Doppler. The analysis of Section 5.5 confirms that the unpredictable Doppler sources observed by the reference receivers are at a level low enough to allow up to 10 s coherent integration without significant degradation. Beyond that period, degradations occur, with the suspected source being drift of the Digitizer's frequency reference.

The remaining Doppler effects caused by outdoor-indoor propagation are thought to be at a lower level than the limiting receiver frequency error. The Doppler rolloff characteristics of signals received indoors are analyzed with long integrations to test this hypothesis. Furthermore, the measured phase of the received signal is analyzed over the course of the data sets to detect any instances of severe phase change, which may indicate changing multipath conditions.

6.5.1 Doppler Power Rolloff for Long Integrations

For each of the fading tests conducted, the peak position of the correlation function in the Doppler offset domain has been compared with that predicted theoretically. For relatively short 200 ms integrations, maximum offsets of up to 0.3 Hz were observed, but the nature of the sinc-squared function remained accurate. In these cases, the addition of noise to the wide Doppler power rolloff function is believed to be a cause of the minor offsets. For longer integrations of 5000 ms, no instances of Doppler error greater than 0.15 Hz were observed except in the cases of weak PRNs with signals below the detection threshold. It has not been feasible to examine data from all PRNs over each data set in high Doppler resolution due to processing limitations. Tests with up to 10 s integration in the Terraario environment—the more difficult of the two—are therefore taken as representative of any severe Doppler errors induced under static conditions. In that environment, signals that are above the detection threshold appear to have Doppler power rolloff characteristics minimally distorted from the ideal sinc-squared rolloff, regardless of the level of code distortion observed. Conversely, signals that do not meet the threshold are significantly affected by noise, and their rolloff functions distorted accordingly.

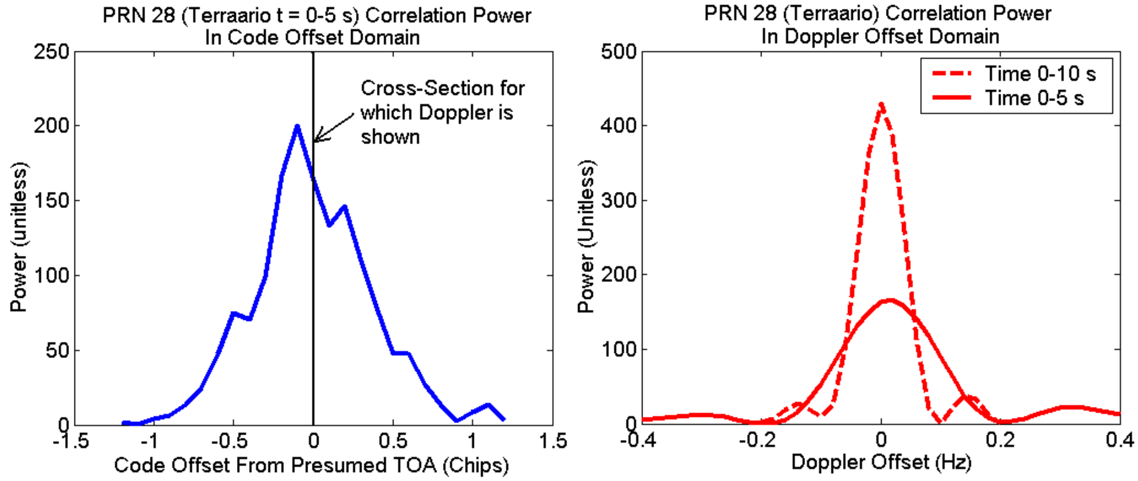

Figure 6.30: Distorted Code Peak Showing Near-Ideal Doppler Characteristics

As an example, the badly distorted code peak of PRN 28 (shown as total power) observed during the first 5 seconds of the Terraario data set, is shown in Figure 6.30. The distortion of the peak is not limited only to the centre Doppler frequency, but is similar on all frequencies within 0.1 Hz of the centre. Still, no major distortion appears in the Doppler offset domain, shown alongside measured with the same 5 s integration. The integration has been extended to 10 s to confirm that the Doppler traits are normal at the highest resolution measurable. This trait is similar for all PRNs observed in the Terraario data set, although the entire data set has not been examined in this high resolution.

If the attenuation and code peak distortion of weak indoor signals is caused by multipath interference, static multipath appears to have minimal impact in the post-correlation Doppler offset domain. If the attenuation is primarily the effect of shadowing the LOS signal, the shadowing caused by building materials appears to have no significant Doppler effect. These results do not necessarily imply that the GPS-indoor channel is frequency-flat, or that Doppler spread is non-existent. Selectivity in the frequency domain may occur, but in such a way that the de-spread signal power is received with the expected Doppler power rolloff characteristic. This is to say that as the bandwidth of the signal is reduced by de-spreading, any frequency-specific effects in the full bandwidth may average out to a negligible effect in the de-spread Doppler power rolloff function.

6.5.2 Detection of Rapid Phase Shifts

The fading series data are examined further to determine the level of phase change occurring over time. Unmodelled phase changes indicate that either rapid changes in multipath occur, or certain Doppler effects exist. Using a frequency lock technique to receive the signal introduces a base phase change between each epoch of coherent integration. In general, the duration of the epoch is not a whole number of Doppler wavelengths, thereby introducing a phase shift when the demodulating signal is reset at the beginning of each epoch.

This base phase shift can be predicted, however, with knowledge of the Doppler during each integration period. Removing this allows the observation of any phase shifts in the signal itself, which may represent Doppler noise or multipath changes. Figure 6.31 presents measurements of epoch-by-epoch phase changes for the Tube rover data set. For 10 of 11 PRNs, the phase change is near 0 for the majority of the time (also seen as a phase shift near 2π). PRN 3 is an exception, with the average epoch-to-epoch phase shift with a mean near π, although this is believed to be an artifact of processing.

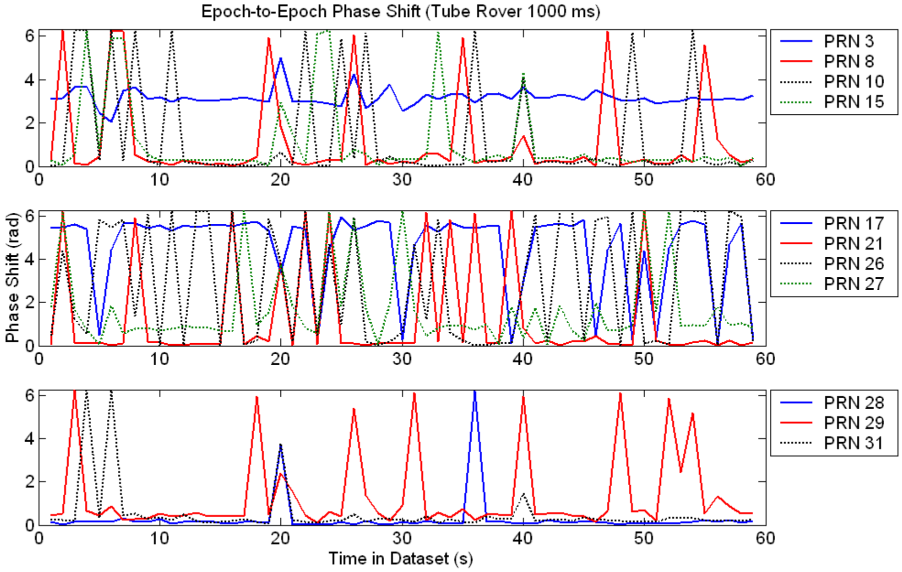

Figure 6.31: Tube Rover Observed Phase Shifts

Phase shifts far from the mean value (0 for most PRNs) may indicate changing multipath conditions. All PRNs experience instances of epoch-to-epoch phase shifts, with major effects observed on PRNs 10, 15, 28, and 31 among others. Most of these occurrences are for a single epoch only, however, with only a handful of examples where successive epochs have large phase shifts. Indications are, therefore, that the observed characteristics are due to either a quickly-changing multipath condition, or simply a measurement noise effect. In fact, phase measurement is not precise given that angles near multiples of 90° have a very low I or Q component, giving rise to a noisy phase measurement.

The unusual fading behaviour of PRN 21 near time 8, 19, 32, and 46 seconds is not clearly linked to phase shifts in the signal. Only one instance of a large phase shift is observed for PRN 21 during these four events, that being at 20 seconds. The remaining times have phase shifts near 0 or 2π.

Terraario rover phase effects have not yet been analyzed using this method. The long integration times required to detect Terraario signals result in a very limited set of results. The analysis should be performed, however, to compare with results from the Tube rover.

6.6 Measurement of Multipath Spread Effects

The signal distortions induced by multipath are examined directly with two separate approaches. First, the impulse response of the channel was measured using a typical correlation method (Ma, 2003), after which super-resolution methods were considered. Following that, the power spread induced by the channel was characterized using a more statistical approach.

6.6.1 Impulse Response Estimation with Correlation Method

Attempts to estimate impulse response directly have been unsuccessful. A selection of signals with noticeable distortion of the correlation function have been tested, with unsuccessful results. The impulse response estimates obtained for PRN 28 from overlapping 5 s integrations are presented in Figures 6.32. The signal has peak SNR of approximately 16 dB in each case, with qualitative similarity in the peak distortion in each epoch. Impulse response in each of the I and Q channels is estimated with the correlation method, and combined to form a power delay response. The estimates of $|h(t)|^2$ for the two case are significantly different.

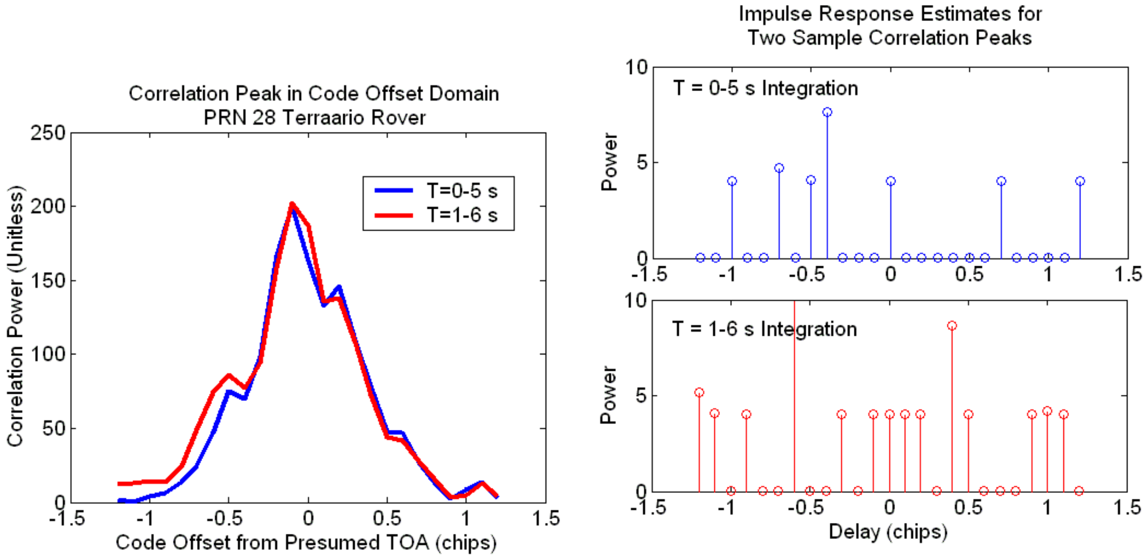

Figure 6.32: Distorted Correlation Power Peak Samples and Resultant Impulse Response Estimates

Qualitatively, the power delay response estimated for the 0–5 s integration appears reasonable. The second estimate is likely in error, as it is dominated by a single strong response well above the scale shown. Results are inconsistent likely due to noise and the limited resolution achievable with this method. The delay resolution shown is approximately 97 ns, which is comparable to the limits set by the sampling period of 101 ns.

6.6.2 Exploration of Super-Resolution Techniques

Techniques to improve impulse response resolution have been explored unsuccessfully. Super-resolution techniques such as MUSIC have been shown to be useful for estimating TOA in CDMA cellular systems in the presence of multipath, as in for example, Klukas (1997) and Dumont (1994). In connection with this research, another member of the PLAN research group has implemented a MUSIC technique in software and tested the ability to achieve better and more accurate impulse response resolution than was achieved with the correlation method.

Several major limitations are believed to have limited the utility of the MUSIC method. First, the MUSIC method operates on the assumption that the number of multipath components are known in advance. In a complex indoor environment, methods to attempt to estimate the number of multipath components have been unsuccessful. The second limit involves the long integration times required to increase SNR to a reasonable level for indoor signals. If the channel is time-variant, changing multipath over the integration period distorts the signal being measured. Finally, a necessary assumption of MUSIC is that multipath components be uncorrelated for separation. In all likelihood, multipath components within a largely unchanging environment are at least partially correlated.

6.6.3 Statistical Power Spread of Correlation Peak

An overall characterization of correlation peak distortion has been examined, after the standard method of estimating impulse response failed. An average power delay profile was developed for each PRN in the Tube rover data set from measurements of the signal power at various code offsets. At each epoch, the peak of the correlation function is detected using direct measurement with multiple correlators. Using the peak correlator as a reference, power is measured at various code offsets. An example of correlation peak properties over time is presented in Figure 6.33 for PRN 17. The normalized peaks are analyzed statistically at each code offset giving a representation of the expected amount of power received at each offset.

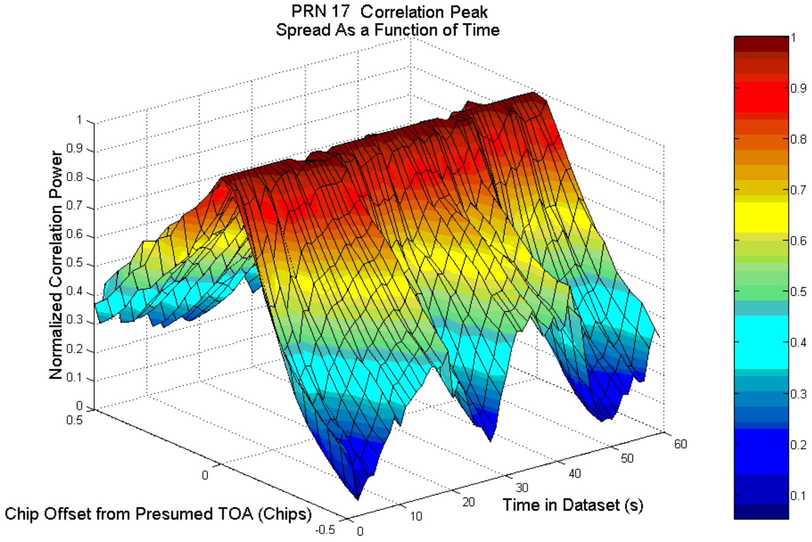

Figure 6.33: Normalized Correlation Peak PRN 17 Over 60 s

Results of this characterization are presented for all PRNs in Tables 6.4 and 6.5. At offsets from -0.4 chips to +0.4 chips from the maximum power, the following statistics are given: First, mean power as a fraction of predicted (undistorted) power at that chip offset. Second, standard deviation of the power at that chip offset, again as a fraction of the expected power. These two characteristics combined give some idea of the delay spread distortion, and the variability of the delay spread for each PRN.

Specific interesting characteristics include the direction of power distortions and the level of deviation expected on these distortions. Examining the data for PRN 29, it can be seen that average power is significantly below that expected in the early part of the correlation function as compared to the ideal autocorrelation function. In the late part, power is very close to expected levels. PRN 26 has a similar characteristic, whereas that of PRN 27 is the reverse.

Significance

These characteristics are representative of two effects. First, the nominal power at any given code offset represents the average level of code peak distortion due to multipath observed during the limited 60-second data set, especially in cases with low relative standard deviation. Second, the normalization of the code peaks also magnifies the effects that noise has on distorting the code peak. A very weak peak, distorted by noise, is given the same weight in the averaging process as a very strong peak distorted by multipath. These instances are identified by the high standard deviation of the measurements, as for PRN 17 at code offsets of ±0.4 chips.

Further characterization of the power spread properties will require longer data sets, but the approach based on a high-resolution measurement of the code peak should be valid.

Power Spread Characteristics—Tube Data Set (1/2)

PRN	Chip Offset	Relative Power	Relative Std. Deviation	PRN	Chip Offset	Relative Power	Relative Std. Deviation
3	-0.4	0.98	0.18	8	-0.4	1.05	0.28
	-0.3	0.98	0.16		-0.3	1.08	0.23
	-0.2	1.00	0.11		-0.2	1.15	0.19
	-0.1	1.03	0.06		-0.1	1.04	0.11
	0.0	0.99	0.03		0.0	0.97	0.03
	0.1	0.99	0.07		0.1	0.94	0.08
	0.2	0.98	0.07		0.2	0.90	0.10
	0.3	0.96	0.10		0.3	0.84	0.11
	0.4	0.95	0.13		0.4	N/A	N/A
10	-0.4	0.96	0.21	15	-0.4	0.90	0.11
	-0.3	0.95	0.15		-0.3	0.90	0.10
	-0.2	0.94	0.12		-0.2	0.92	0.07
	-0.1	0.99	0.06		-0.1	0.97	0.04
	0.0	1.00	0.01		0.0	1.00	0.00
	0.1	0.93	0.04		0.1	0.99	0.03
	0.2	0.93	0.06		0.2	1.00	0.05
	0.3	0.90	0.09		0.3	1.00	0.06
	0.4	0.89	0.11		0.4	1.02	0.08
17	-0.4	1.01	0.35	21	-0.4	0.93	0.08
	-0.3	0.96	0.24		-0.3	0.92	0.07
	-0.2	0.96	0.15		-0.2	0.95	0.05
	-0.1	0.99	0.06		-0.1	1.00	0.02
	0.0	1.00	0.01		0.0	1.00	0.00
	0.1	0.96	0.04		0.1	0.96	0.02
	0.2	0.98	0.06		0.2	0.98	0.03
	0.3	0.98	0.09		0.3	0.97	0.03
	0.4	1.01	0.14		0.4	1.00	0.05

Table 6.4: Measured Power Spread Characteristics (1/2)

Power Spread Characteristics—Tube Data Set							
PRN	Chip Offset	Relative Power	Relative Std. Deviation	PRN	Chip Offset	Relative Power	Relative Std. Deviation
26	-0.4	0.76	0.24	27	-0.4	0.97	0.16
	-0.3	0.76	0.18		-0.3	0.99	0.16
	-0.2	0.79	0.15		-0.2	1.00	0.13
	-0.1	0.91	0.09		-0.1	1.00	0.06
	0.0	1.00	0.01		0.0	0.99	0.02
	0.1	0.97	0.04		0.1	0.91	0.04
	0.2	0.97	0.06		0.2	0.91	0.07
	0.3	0.95	0.08		0.3	0.88	0.10
	0.4	0.97	0.14		0.4	0.87	0.11
28	-0.4	0.94	0.07	29	-0.4	0.85	0.40
	-0.3	0.94	0.06		-0.3	0.81	0.32
	-0.2	0.96	0.05		-0.2	0.79	0.26
	-0.1	0.98	0.03		-0.1	0.83	0.19
	0.0	1.00	0.00		0.0	0.97	0.07
	0.1	0.96	0.02		0.1	0.99	0.07
	0.2	0.95	0.03		0.2	1.01	0.12
	0.3	0.92	0.03		0.3	1.00	0.21
	0.4	0.91	0.05		0.4	1.03	0.26
31	-0.4	0.93	0.12				
	-0.3	0.94	0.09				
	-0.2	0.98	0.07				
	-0.1	0.97	0.05				
	0.0	1.00	0.01				
	0.1	1.04	0.04				
	0.2	1.03	0.06				
	0.3	1.00	0.07				
	0.4	1.00	0.10				

Table 6.5: Measured Power Spread Characteristics (2/2)

Chapter 7

Synthesis of Model Characteristics

The analyses of the two raw data sets have examined two main areas. Sections 6.2 and 6.3 examined the availability and accuracy of GPS performance indoors using a high-sensitivity technique and a static receiver. These are, of course, the main points of concern when determining a receiver's functionality indoors. Sections 6.1 and 6.4–6.6 examined various aspects of the received signals to determine likely causes for the performance degradations, and to search for possible models to represent these degradations. This chapter reviews the significant results in an attempt to synthesize a suitable model framework for indoor GPS signals.

7.1 Signal Power Effects and Positioning Performance

7.1.1 Fading

Fading has been observed in both indoor environments at rates from 0.2 Hz to 5 Hz. The most apparent observation is the difference in mean fades in a relatively open environment (Tube) versus one deep indoors (Terraario). Mean fade of 18.4 dB observed in the Tube environment increased to over 35 dB for detected signals in Terraario. With standard receivers, signal levels in both environments were too low for reliable detection and tracking. In itself, however, this is not a novel result as heavy signal attenuation deep indoors has been identified and studied in the past. Rather, the ability to receive and measure signals with C/N_o nearing 0 dB-Hz using

10 s integration times has provided an idea of the signal strength variations that actually occur, regardless of a standard receiver's ability to measure them.

Nearly all signals analyzed showed fairly constant mean fade levels throughout the 60-second data sets, with the exception of PRN 21 in the Tube data set. There is an apparent dependence of the mean fade on the direct propagation path and its relationship to the environmental surroundings. This sort of relationship has been observed in other studies, and is theoretically expected. Higher-frequency analysis of Tube fading showed a more random characteristic with fades of a few decibels with low coherence times. Even more rapid changes over periods shorter than the integration time—a minimum of 200 ms—are not observable with the technique implemented.

Probability distributions of the signal envelopes in the Tube environment at 5 Hz showed mixed results. Most PRNs had no resemblance to standard fading distributions. Possible reasons include the limited amount of data available—only 300 data points—and the longer-term trends which may require more data to characterize. Also, 200 ms is the minimum feasible integration time to receive the Tube rover signals, which introduces averaging of any fading occurring at faster rates. Despite these limitations, PRN 3 in particular showed a strong similarity to either a Rician or Loo distribution. This may indicate that for PRN 3, the component signals actually consist of a strong direct signal and a number of scattered multipath components. Other PRNs may show such a distribution if de-trended.

Implications for Modelling

Signal strength degradation indoors is clearly related to environmental surroundings, with mean fades defined partly by the nature of the direct propagation path. There is also an apparent high-frequency fading component present in the data, however, which is not a clear factor of the environment. The observed fast fading (5 Hz or faster) on the Tube rover data set shows some Rician-like (or Loo-like) characteristics, indicating that the indoor signal likely consists of a dominant signal and a large number of scattered or diffracted multipath components. Further fading measurements are necessary to examine fading distributions over a longer term.

7.1.2 Position Performance

Computing position using various techniques shows a dependence of accuracy on the technique employed. In the Tube environment, positions calculated with the peak detection method at both 200 ms and 1000 ms integration times have similar error statistics. Meanwhile, application of a typical non-coherent code phase discriminator gives degraded accuracy, with the degradation increasing with correlator spacing. Again, statistics are similar for the 200 ms and 1000 ms integration cases using a 0.5 chip spacing discriminator.

Two factors lead to position degradation when using the discriminator. First, a multipath-affected correlation peak may have its true peak at the correct TOA, as long as multipath is weaker than the direct signal. However, the shape of the peak may be distorted, affecting the discriminator's peak estimate. Second, the wider correlator spacing requires the use of lower-power measurements away from the peak power. Therefore, in addition to code peak distortion, noise has a more significant effect on more widely-spaced correlators.

The similarities between the two integration times, despite approximately 7 dB difference in SNR, suggests that noise is not the most significant contributor to position degradation in the Tube environment. For peak detection, a combination of limited measurement resolution and some level of noise caused the observed errors. For the discriminator cases, it is likely that distortion of the code peak by weaker multipath is a large contributor to pseudorange measurement error.

Terraario positions computed with 5000 ms integration times have a similar relationship. Those computed with the peak detection method have moderately better performance than those computed with a 0.45 chip spacing discriminator. The difference is not as great as observed for the Tube data, partly because lower peak measurement resolution was used in the Terraario case.

A greater dependence on integration time was observed for the Terraario positions. The use of 5000 ms integration time provided 100% position availability, and good average DOPs with at least 5 SVs used for positioning in all epochs. Reduction of integration time to only 1000 ms reduced position availability to only 33%, with an average of only 4.2 SVs available at these epochs and a maximum of only 5 SVs used. Significant degradation in the north and vertical directions resulted. The degradation is mostly due to the larger DOPs, though, and not due to large measurement errors. The accuracy of measured pseudoranges is actually similar for both integration times, when a signal is detected above the threshold.

Implications for Modelling

The most important aspect of GPS performance, namely position accuracy, is evidently most degraded by low satellite availability due to fading and attenuation. The other common degradations caused by multipath and noise were shown to be less significant than the effect of losing signals completely. The implication is that a model designed to test indoor receiver performance must place a strong emphasis on accurately modelling signal strength.

Pseudorange measurement errors caused by noise and multipath have not been separately identified with any certainty. The superior position-domain performance of peak-detection techniques is evidence that any multipath distortion is caused by weak multipath, and does not significantly alter the position of the absolute correlation peak. However, differences between peak-detection performance and that with a non-coherent discriminator seem to indicate that some peak distortion occurs. To accurately test a receiver with any form of discriminator, approximating peak distortion will be necessary even though it is a less significant contributor to error than fading.

7.2 Specific Signal Characteristics on the Indoor Channel

7.2.1 Doppler Errors

No significant Doppler errors have been observed in either data set, with received power closely matching that predicted theoretically in the Doppler offset domain. Two conclusions are considered. One possibility is that no major Doppler errors are induced by the GPS-indoor channel. The second is that any Doppler errors are large enough to prevent detection of signals, and thereby prevent the measurement of those Doppler errors. Based on the successes measuring signals at all epochs in the Tube environment, the first explanation of no major Doppler errors is considered more likely.

In the case of moving receivers, a completely different channel results, however. Relative Doppler differences between direct and NLOS paths are expected to be significant in those cases, causing a spreading of the Doppler rolloff function and limitations on coherent integration times. The possible effects of these changes cannot be predicted without testing and examination of signals gathered under dynamic conditions.

7.2.2 Phase Changes Between Integration Epochs

Phase changes have been measured from epoch-to-epoch, accounting for the inherent phase change induced by the frequency-locked receiver implementation used. All PRNs in the Tube environment experienced some epochs of significant phase shift, possibly indicating a change in multipath conditions. There is no apparent relationship between these phase shifts and observed fading or position errors, however. In particular, the unusual fading events observed on PRN 21 in the Tube environment do not have associated phase shifts.

A fundamental limitation of the frequency-locked high-sensitivity implementation is revealed here. Any phase shift that occurs during a coherent integration simply serves to attenuate the overall received power. It is therefore not possible to conclude that epoch-to-epoch phase shifts are representative of true signal characteristics. In fact, the high-frequency fading observed in the Tube rover data set indicates that there are rapid phase shifts occurring at all times, which are simply obscured in the integration process. Therefore, the lack of measured phase shifts does not give any significant direction for channel modelling one way or another.

7.2.3 Impulse Response Characteristics

The impulse response of the channel could not be estimated using standard estimation techniques or the MUSIC super-resolution algorithm. Two likely reasons have been suggested. First, the level of noise remaining on the signal even after high-sensitivity processing is sufficient to make standard channel estimation ineffective. Second, the impulse response might vary rapidly, especially during a coherent integration. If this occurs, the effects to be measured are destroyed by time averaging.

In a complex indoor environment, it is reasonable to assume that signals would have significant time-varying properties. It was initially assumed that these temporal variations would be minimal over only 60 seconds, and adequately approximated as being static. However, that does not appear to be the case based on observations of fading, position error, phase shifts, and correlation peak distortions. A constant impulse response is therefore not a reasonable description for an indoor channel, or even a subset of that channel, such as from a single satellite to a receiver.

7.2.4 Power Delay Characterization

A general description of multipath power spread in the Tube environment has been developed in Section 6.6. The level of power spread on the correlation peak has been quantified relative to the expected power delay profile. The description actually incorporates two effects: the effect of additive noise in low-SNR epochs, and the average power spread thought to be caused by multipath. With additional data to analyze, this type of characterization might prove useful for modelling multipath indoors. Currently, the two effects of multipath and noise have not been separated, but the variance of the spread statistics is useful for identifying true multipath spread and noise effects. Clearly further refinement is necessary to use such a description for signal modelling.

7.3 GPS-Indoor Channel Properties

The most significant observed channel properties are reviewed in this section, and related to the modelling requirements for indoor GPS.

1) Position Degradation Most Significant Due to Low Availability

The most significant degradations in GPS position in either environment were seen under conditions of low satellite availability. Using only 4 SVs, large position errors resulted in the directions with poor DOP, while positions comparable to those obtained under higher-SNR conditions were seen in the direction with good DOP. Replication of the satellite availability is therefore of prime importance to replicating accurate GPS behaviour indoors.

2) Heavy Dependence of Fading on Geometry and Materials of Environment

A very strong correlation between signal strength and the receiver location is observed by comparison of the Tube and Terraario environments. A mean fade of approximately 18 dB in the Tube environment increases to over 35 dB only a few metres away in Terraario. This is an intuitive result, but emphasizes the need to model fading based on specific environmental characteristics.

A weaker correlation was observed between signal fading and the presumed LOS propagation path from each SV. Further observation is necessary to confirm this correlation, but previous tests using high-sensitivity receivers have also measured such a relationship. Furthermore, it is obvious from a theoretical perspective that signals penetrating various disparate materials will experience different levels of fading.

3) Low-Frequency Fading on High-Sensitivity Intervals

Fading has not been measured at rates greater than 5 Hz. However, over intervals greater than 1 s, fades are highly correlated except in unusual circumstances. Over shorter intervals, such as the 200 ms tests used in the Tube environment, fading between epochs is more variable and shows some similarity to established fading PDFs used for communications channels.

4) Sources and Nature of Multipath Remain Unclear

No instances of strong, long-delay multipath were observed in either environment. Short-delay multipath clearly has some effect, as characterized with the power delay spread in Section 6.6, but the actual sources of multipath have not been identified. Fast fading and quickly-changing correlation peak distortion indicate that most multipath is short-delay and relatively random, as from diffraction or scattering. If this holds true, the fading effects of multipath may be considered somewhat independently from the distortion effects. With sufficient multipath components, overall signal strength may be determined statistically according to a theoretical distribution, such as Loo's distribution, regardless of the path delays. Multipath power spread becomes, in that case, an independent property. Unfortunately, the nature of changing multipath distortion on the inphase and quadrature channels has not been determined. It is necessary to model the two channels independently to accurately test receiver performance.

7.4 Recommended Model for GPS-Indoor Channel

The outline of a GPS-indoor channel model is presented in this section based on the channel properties identified in the previous section.

7.4.1 Environmental Framework

To account for severe differences in channel characteristics based on elevation and azimuth, the basic framework of a suitable indoor channel model must be a representation of the indoor environmental characteristics. This should include information on environmental geometry, composition, and orientation. It is not suitable to describe an environment with general statistical parameters, because each satellite is affected differently depending on propagation paths. The importance of constellation geometry on positioning has been demonstrated.

Complexity of the environmental framework shall depend on the conditions for which modelling is required. A fully-developed simulated environment with specific material properties as in Pérez-Fontan et al. (2004) is not necessary to test E-911 GPS receiver performance. Rather, an elevation-azimuth category description as in Spirent's GSS 6560 hardware simulator may be more appropriate. Definition of specific categories requires more extensive testing with various techniques.

7.4.2 Signal Composition

Having failed to identify and characterize specific multipath sources in the two environments tested, a geometric ray-based model is not recommended. The potential scattering and diffraction sources indoors are numerous, likely giving rise to more NLOS paths than can be deterministically simulated.

It is recommended that signal strength and multipath distortion be modelled separately. Separation of these two effects is physically unrealistic, but properties of observed signals indoors have shown a level of de-correlation between fading and multipath. This may be due to the presumed complex nature of multipath.

Signal Strength

Signal strength may be defined as the sum of an attenuation, induced by building materials, and a statistical component introducing rapid changes over time. Insufficient data has been gathered to recommend a specific statistical characterization, but some evidence of Rician-like or Loo-like statistics has been observed. Further measurements may allow selection of a statistical function suitable for whatever environmental categories are defined. In order to replicate the Tube and Terraario environments, the time-varying nature of signal strength should have a low-frequency component to account for changes over several seconds, and a high-frequency component to account for changes at rates greater than 5 Hz. A standard statistical model may be used for the high-frequency component, but further investigation is required to characterize slow changes.

This recommendation does not account for dramatic power changes such as that observed on PRN 21 in the Tube environment, which are so far unexplained. Indoor environments are very complex, and certainly introduce specific effects which cannot be modelled generically.

Multipath Distortion

Multipath distortion of the correlation peak is a result of the combination of numerous NLOS components. Without specifically identifying these components, a statistical model for simulating this distortion is recommended. The channel may be represented as a time-varying statistical distribution of delayed impulses. Low-frequency changes on the order of a few seconds are suggested to replicate the behaviour observed in the data.

To separate the effects of overall power changes and multipath changes, amplitude and delay of multipath should be adjusted separately from overall power. Implementation of separate power and multipath statistics will require control of signals to an extent that may be unrealistic physically. However, receiver performance should be realistically tested.

7.4.3 Model Customization Techniques

Creating simulations of representative environments for receiver testing will require customization of the model components. The most variable parameter is likely to be signal strength attenuation and variability, which depends highly on the propagation medium. Two tested environments have shown over 20 dB variation in a single building. Delay spread observed on all PRNs shows less dependence on the medium of propagation. Short-delay multipath can be well approximated statistically, but other indoor environments may have significantly different delay spreads. Accurate model parameters will result from techniques suggested as future work.

7.5 Comparisons with Existing Models

The recommended model has not been implemented or tested in simulation or hardware. Future work will be undertaken to implement and customize this model, or a similar type, and test with real GPS receivers. The possible improvements as compared with those models reviewed in Chapter 3 are briefly discussed here, from a purely theoretical perspective.

Statistical fading models were discussed and have been shown to represent the fading probability of GPS signals fairly well over long periods. The major limitations of these models include their lack of ability to generate realistic time-domain fading series, and their generic categorization of fading based on elevation, average level of obstruction, or other general properties of the environment. While the suggested model relies on statistical descriptions of fading, several improvements over standard statistical models are foreseen. First, an environmental framework allows the fading to be tailored to the specific propagation path, which is extremely important indoors. This tailoring includes the use of a 'mean attenuation' parameter that varies for each signal. In addition, the ability to generate time series fading with realistic coherence times is to be included.

Improvements in modelling multipath delay and distortion are limited. The suggested model uses a statistical delay spread description, as have previous models. The development of algorithms to accurately generate delay spread is yet to be considered. By using a statistical delay description, the model lacks the ability to test a receiver's ability to separate and reject individual multipath components. This capability is included in a purely geometric model such as in Spirent's GSS 6560. This is an acceptable limitation, however, because indoor performance is more dependent on ability to reject a large amount of attenuation and distortion than that caused by a few strong multipath components.

Incorporating the geometry of the environment into a model is not a novel idea; as mentioned previously, Spirent's GSS 6560, among others, generates signals based on certain propagation categories. These and other geometric methods go further, however, and model individual rays propagating on deterministic paths to create a composite signal. To date, these models have had some success at replicating indoor conditions, but still have limitations. For example, it has proven difficult to accurately model the behaviour of fading and multipath error simultaneously using the GSS 6560, because adjusting model parameters affects both properties. The suggestion to model signal strength and multipath errors somewhat independently may improve the ability to customize a model for a specific environment, without significant field testing in advance.

Chapter 8

Conclusions & Future Work

8.1 Contributions of Research

8.1.1 Development and Test of HS Analysis Tool

The software analysis tools and techniques developed to implement extremely long coherent integrations have proven successful when applied to Digitizer data. The ability to integrate coherently for up to 10 s with minimal signal degradation is virtually unprecedented in the literature. The Doppler modelling necessary to implement this technique has proven sufficient for use in a stationary mode with the Datum ET-6000 OCXO oscillator. In itself, this tool does and will continue to provide an ability to analyze high-bandwidth raw GPS signals in novel ways.

Further development of the main high-sensitivity software is in progress. Its capabilities will be extended to accommodate other data formats and possibly new signals such as the GPS L2C signal nearing deployment. Additionally, techniques to enable high-sensitivity integration in controlled dynamic modes will be investigated. Tests using this technique have been recommended as future work.

8.1.2 Weak Signal Measurements

Fading in excess of 40 dB has been identified indoors and broadly characterized by this research. The ability to receive signals at such low levels, and to generate reasonably accurate positions from those signals, is thought to be a significant achievement.

That said, the work of Peterson et al. (1997) who reported measuring fades as high as 60 dB would seem to indicate that the sensitivity reported herein is not impressive. The results reported in that study cannot be reconciled with results reported herein, or theoretical processing gain equations, however. Even a strong signal of 50 dB-Hz measured in a 4 MHz single-sided bandwidth has an initial SNR of -19 dB. It therefore requires at least 19 dB of processing gain to reach a positive SNR level. With 160 ms integration time, the total processing gain of 61 dB can therefore provide a maximum SNR of only 42 dB. It is unclear, therefore, how weaker signals could be measured more than 60 dB below reference levels. This question remains unresolved after reviewing further research by the authors of Peterson et al. (1997).

Positioning performance has also been observed through the use of high-sensitivity, high-resolution measurement techniques that demonstrate the potential pseudorange accuracy achievable indoors when weak signals can be measured. The generality of the results is limited, however, by the amount of data available. Some conclusions regarding the nature of indoor multipath distortion have resulted from these measurements, along with other analyses of the signal properties such as power spread.

8.1.3 Propagation Channel Characterization

While lacking generality, some conclusions regarding the GPS-indoor channel are significant. Some previous research has been corroborated and other research brought into question. Most significantly, previous results indicating the dependence of signal propagation on the direct propagation path have been supported by the results herein. The deeper fades measured with the high-sensitivity technique have improved understanding of this dependence. Additionally, observed fading distributions at

5 Hz give support to the idea that fast fading may accurately be represented by certain statistical distributions, although the limited amount of data makes it impossible to confidently suggest a distribution. Previously, only long-term distributions had been analyzed indoors.

The results of a study by Haddrell & Pratt (2001) have been brought into question by some results reported herein. Those researchers suggest that the apparent long coherence times of GPS indoor fades were indicative of distinct NLOS rays combining to cause observed fading. Results from Digitizer data analysis suggest that indoor fading is much more complex than that, consisting of a combination of fast fading from random multipath and a long-term effect due to environmental characteristics. These differences could, of course, be due to differences in the environments tested. It is necessary to conduct a number of further tests to draw any definite conclusions.

8.1.4 Model Development

A model has not yet been developed which is immediately suitable for testing GPS receiver performance indoors. The complex nature of indoor propagation requires additional investigation to accurately model. However, several characteristics of the specific GPS-indoor channels available have been identified and linked to related model performance criteria. A framework for a model has been suggested that should appropriately test receiver capabilities in simulated indoor environments.

The specific limitations of the proposed model are related to general indoor characteristics that cannot be accurately measured with only two data sets. Some of the proposed future work will allow generalization of a model, followed by its implementation and test.

8.2 Limitations of Research

The two most significant limitations of this research are as follows:

1. results have limited generality due to limited test environments, and
2. the HS measurement technique has limited ability to measure high-frequency or transient characteristics of weak signals.

The first limitation is easily overcome by testing in a wider variety of environments and improving processing efficiency to facilitate rapid analysis. This will be undertaken in future work by the PLAN group. The second limitation is more fundamental. Techniques to improve the measurement of high-frequency characteristics will require reducing receiver noise, improving receiver frequency synthesis, and developing new post-processing techniques.

Further to the above, the results and conclusions drawn from the research are not actually conclusive. The results tend to *suggest* certain characteristics of the GPS-indoor channel, but there are insufficient data to draw concrete conclusions. Additional data sets are required, but this research has focused instead on developing and testing a novel analysis method with which to analyze those data.

8.3 Recommendations for Future Work

The analysis techniques demonstrated in this thesis will continue to be developed by the PLAN group for further indoor channel measurements. Due to issues of processing time, all desired analyses could not be completed at this time. Further research on specific aspects of the GPS-indoor signal, such as position-domain performance using various processing schemes and techniques, may be undertaken as other researchers see fit.

Further tests of impulse response estimation are not immediately recommended. The failures of impulse response measurements with the Nokia data sets indicates that the complex indoor environment introduces too much noise and too many transient multipath characteristics to accurately measure this property. Instead a focus on broadly characterizing the power delay spread measurement should be undertaken.

To proceed with more specific model development, a number of additional data-gathering campaigns and analyses are recommended.

8.3.1 Recommended Indoor Digitizer Tests

Time-Offset Tests While a long-term data gathering would be ideal for observing overall environmental characteristics, this is not feasible with the Digitizer given the large amount of data it produces. Rather, a series of static tests are recommended in a single location with intervals of 30–60 minutes between tests to attempt to identify long-term environmental characteristics. Similarly, data should be gathered in a single location at two epochs separated by 12 sidereal hours, as the GPS constellation is approximately the same every 12 sidereal hours. Such tests would allow identification of channel properties which are correlated and uncorrelated over time due to the changing GPS constellation.

Various Antenna Configurations Experiments with various antenna types may prove useful to further evaluate multipath characteristics. Tests with linearly-polarized antennas may provide significantly different multipath characteristics which are more representative of true conditions, before being affected by GPS antenna gain and polarization. Another potential set of tests with specific antennas is suggested to examine potential specular multipath. The signals of PRN 21, for example, which were fairly strong in the Tube rover environment, had a presumed propagation path through the western building. A pair of successive tests with a directional antenna pointing at the satellite and in the direction of a possible specular reflection might give more information on its true propagation path.

Dynamic Tests A test with a dynamic antenna is recommended to aid in identifying multipath through Doppler separation. As mentioned, long integrations are impossible if dynamics are not modelled. However, the use of a controlled source of motion, such as a computer-controlled moving platform, may induce a Doppler effect than can be accurately modelled. A linear speed of as little as 10 cm/s may provide the means to identify and separate LOS signals from multipath. The ability to account for controlled receiver dynamics in high-sensitivity processing is the first priority for modifying the existing software. This test, along with time-offset tests are highly recommended to fully explore the capabilities of channel analysis using the Digitizer.

Measurements to Generalize Channel Properties A campaign to gather Digitizer data in a large number of different environments is *not* specifically recommended to derive more general channel properties. The limited amount of data provided by the Digitizer makes any results from a single epoch very specific to current conditions. Results are not general enough for this purpose, so the Digitizer should be reserved for targeted analyses of specific conditions as recommended above.

More thorough analysis of GPS propagation through building materials may be conducted using the Digitizer in a manner similar to that used by Klukas et al. (2004). Tests of shadowing and reflection would allow one to identify the nature of received Digitizer data under controlled conditions, perhaps aiding in the identification of these propagation conditions in other environments. Introduction of controlled multipath would be similarly useful.

8.3.2 Additional Work Recommended

The implementation issues relating to the model framework presented in Chapter 7 have not been analyzed. The framework will require some complex algorithms to implement the signal strength and multipath effects realistically. Before proceeding with research to customize this type of framework, it is recommended that the implementation issues be examined and any possible points of difficulty identified.

Bibliography

Aiga, Y., K. Washizu, M. Nakamura, K. Sorita, M. Shoji, & Y. Ogasa (2003) Space Time Characteristics of the RF Absolute Power of Indoor GPS Signals. *Proceedings of ION GPS/GNSS 2003 (September 9-12, Portland OR)*, 1149–1157. US Institute of Navigation, Alexandria VA.

Akturan, R. & W. J. Vogel (1997) Path diversity for LEO satellite-PCS in the urban environment. *IEEE Transactions on Antennas and Propagation*, 45, 1107–1116.

Caratori, J., M. Francois, & N. Samama (2003) UPGRADE: An Indoor Positioning System Using A Standard GPS Receiver. *Proceedings of ION GPS/GNSS 2003 (September 9-12, Portland OR)*, 593–602. US Institute of Navigation, Alexandria VA.

Chansarkar, M. M. & L. Garin (2000) Acquisition of GPS Signals at Very Low Signal to Noise Ratio. *Proceedings of ION National Technical Meeting (January 26-28 2000, Anaheim CA)*, 731–737. US Institute of Navigation, Alexandria VA.

Dumont, L. R. (1994) *Super-Resolution of Discrete Arrivals in a Spread Spectrum System*. Master's thesis, University of Calgary Department of Electrical and Computer Engineering.

El-Gizawy, M. & S. Skone (2002) A Canadian Ionospheric Warning and Alert System. *Proceedings of ION GPS 2002 (September 24-27, Portland OR)*, 1345–1351. US Institute of Navigation, Alexandria VA.

FCC (1996) Docket No. 94-102. Revision of the Commission's Rules to Ensure Compatibility With Enhanced 911 Emergency Calling Systems.

GEO (2005) GeoForschungsZentrum Potsdam Website. http://www.gfz-potsdam.de/index-en.html.

Goldhirsh, J. & W. J. Vogel (1998) Handbook of Propagation Effects for Vehicular and Personal Mobile Satellite Systems. Technical Report A2A-98-U-0-021 (APL) / EERL-98-12A (EERL), Johns Hopkins University Applied Physics Laboratory and University of Texas at Austin Electrical Engineering Research Laboratory. Accessible at http://www.utexas.edu/research/mopro/index.html (last accessed November 5, 2004).

Haddrell, T. & A. R. Pratt (2001) Understanding the Indoor GPS Signal. *Proceedings of ION GPS 2001 (September 11-14, Salt Lake City UT)*, 1487–1499. US Institute of Navigation, Alexandria VA.

Haykin, S. (2001) *Communication Systems, 4th Edition.* John Wiley & Sons, Toronto, ON.

Hoffman-Wellenhof, B., H. Lichtenegger, & J. Collins (2001) *GPS Theory and Practice*. Springer-Verlag Wein, New York NY.

ICD200C (2000) NAVSTAR GPS Space Segment / Navigation User Interfaces. GPS Interface Control Document.

IGS (2005) IGS Product Downloads. http://igscb.jpl.nasa.gov/components/prods.html.

Kaplan, E. D., ed. (1996) *Understanding GPS: Principles and Applications*. Artech House, Boston MA.

Karasawa, Y., K. Minamisono, & T. Matsudo (1995) A Propagation Channel Model for Personal Mobile-Satellite Services. *Proceedings of Progress of Electromagnetic Research Symposium of the ESA*, 11–15. European Space Agency, Noordwijk, Netherlands.

Karunanayake, M. D., M. E. Cannon, G. Lachapelle, & G. Cox (2004) Evaluation of Assisted GPS (AGPS) in Weak Signal Environments Using a Hardware Simulator. *Proceedings of ION GNSS (September 21-24, 2004, Long Beach, CA)*, 2416–2426. US Institute of Navigation, Alexandria VA.

Klukas, R., O. Julien, L. Dong, E. Cannon, & G. Lachapelle (2004) Effects of Building Materials on UHF Ranging Signals. *GPS Solutions*, 8, 1–8.

Klukas, R., G. Lachapelle, C. Ma, & G.-I. Jee (2003) GPS Signal Fading Model for Urban Centres. *IEE Proceedings on Microwaves, Antennas and Propagation*, 150, 245–252.

Klukas, R. W. (1997) *A Superresolution Based Cellular Positioning System Using GPS Time Synchronization*. Ph.D. thesis, University of Calgary Department of Geomatics Engineering. Available at http://plan.geomatics.ucalgary.ca/publications.php.

Krakiwsky, E. J. (1990) The Method of Least Squares: A Synthesis of Advances (ENGO 629 Course Notes, Department of Geomatics Engineering, University of Calgary).

Lachapelle, G. (2002) Navstar GPS: Theory and Applications (ENGO 625 Course Notes, Department of Geomatics Engineering, University of Calgary).

Lachapelle, G., E. Cannon, R. Klukas, S. Singh, R. Watson, P. Boulton, A. Read, & K. Jones (2003a) Hardware Simulator Models and Methodologies for Controlled Performance Assessment of High Sensitivity AGPS Receivers. *Proceedings of GNSS 2003 (April 22-25, Graz Austria)*, 21 Pages. European Group of Institutes of Navigation (EUGIN).

Lachapelle, G., E. Cannon, R. Klukas, S. Singh, R. Watson, P. Boulton, A. Read, & K. Jones (2004) Hardware Simulator Models and Methodologies for Indoor Performance Assessment of High Sensitivity Receivers. *Canadian Aeronautics and Space Journal*, 50, 151–168.

Lachapelle, G., H. Kuusniemi, D. T. H. Dao, G. MacGougan, & M. E. Cannon (2003b) HSGPS Signal Analysis and Performance Under Various Indoor Conditions. *Proceedings of ION GPS/GNSS 2003(September 9-12, Portland OR)*, 1171–1184. US Institute of Navigation, Alexandria VA.

Lavergnat, J. & M. Sylvain (2000) *Radio Wave Propagation: Principles and Techniques*. John Wiley & Sons, Toronto, ON.

Lee, J. S. & L. E. Miller (1998) *CDMA Systems Engineering Handbook*. Artech House Publishers, Boston, MA.

Loo, C. (1985) A Statistical Model for a Land Mobile Satellite Link. *IEEE Transactions on Vehicular Technology*, VT-34, 122–127.

Lutz, E., D. Cygan, M. Dippold, F. Dolainsky, & W. Papke (1991) The Land Mobile Satellite Communication Channel–Recording, Statistics, and Channel Model. *IEEE Transactions on Vehicular Technology*, 40, 375–386.

Ma, C. (2003) *Techniques to Improve Ground-Based Wireless Location Performance Using a Cellular Telephone Network*. Ph.D. thesis, University of Calgary Department of Geomatics Engineering. Available at http://plan.geomatics.ucalgary.ca/publications.php.

Ma, C., G. Jee, G. MacGougan, G. Lachapelle, S. Bloebaum, G. Cox, L. Garin, & J. Shewfelt (2001) GPS Signal Degradation Modeling. *Proceedings of ION GPS 2001 (September 11-14, Salt Lake City UT)*, 882–893. US Institute of Navigation, Alexandria VA.

Ma, C., G. Lachapelle, & M. E. Cannon (2004) Implementation of a Software GPS Receiver. *Proceedings of ION GNSS (September 21-24, 2004, Long Beach, CA)*, 956–970. US Institute of Navigation, Alexandria VA.

MacGougan, G., G. Lachapelle, R. Klukas, K. Siu, L. Garin, J. Shewfelt, & G. Cox (2002) Degraded GPS Signal Measurements with a Stand-Alone High Sensitivity Receiver. *Proceedings of ION National Technical Meeting (January 28-30 2002, San Diego CA)*, 191–204. US Institute of Navigation, Alexandria VA.

Mattos, P. G. (2003) Solutions to the Cross-Correlation and Oscillator Stability Problems for Indoor C/A Code GPS. *Proceedings of ION GPS/GNSS 2003 (September 9-12, Portland OR)*, 654–659. US Institute of Navigation, Alexandria VA.

NOAA (2005) NOAA Space Environment Center. http://www.sec.noaa.gov/.

Orsak, G. C. (1997) Optimum Receivers. J. D. Gibson, ed., *The Communications Handbook*, Chapter 12, 141–153. CRC Press / IEEE Press, Boca Raton FL.

Papoulis, A. & S. U. Pillai (2002) *Probability, Random Variables and Stochastic Processes, 4th Edition*. McGraw Hill Higher Education, Toronto, ON.

Parkinson, B. W. & J. J. Spilker, eds. (1996) *Global Positioning System: Theory and Applications*. American Institute of Aeronautics and Astronautics, Inc., Washington DC.

Parsons, J. D. (2000) *The Mobile Radio Propagation Channel, 2nd Edition*. John Wiley & Sons, Toronto, ON.

Pérez-Fontan, F., B. Sanmartin, A. Steingass, A. Lehner, J. Selva, E. Kubista, & B. Arbesser-Rastberg (2004) Measurements and Modeling of the Satellite-to-Indoor Channel for Galileo. *Proceedings of ION National Technical Meeting (January 26-28 2004, San Diego CA)*, 190–202. US Institute of Navigation, Alexandria VA.

Peterson, B., D. Bruckner, & S. Heye (1997) Measuring GPS Signals Indoors. *Proceedings of ION GPS (September 16-19 1997, Kansas City, MO)*, 615–624. US Institute of Navigation, Alexandria VA.

Peterson, R. L., R. E. Ziemer, & D. E. Borth (1995) *Introduction to Spread Spectrum Communications*. Prentice Hall Inc., Upper Saddle River, NJ.

Petovello, M. G., O. Mezentsev, G. Lachapelle, & M. E. Cannon (2003) High Sensitivity GPS Velocity Updates For Personal Indoor Navigation Using Inertial Navigation Systems. *Proceedings of ION GPS/GNSS (September 9-12 2003, Portland OR)*, 2886–2896. US Institute of Navigation, Alexandria VA.

Pritchard, W. (1997) The Calculation of System Temperature for a Microwave Receiver. J. D. Gibson, ed., *The Communications Handbook*, Chapter 71, 966–975. CRC Press / IEEE Press, Boca Raton FL.

Rappaport, T. S., R. Muhamad, & V. Kapoor (1997) Propagation Models. J. D. Gibson, ed., *The Communications Handbook*, Chapter 84, 1182–1196. CRC Press / IEEE Press, Boca Raton FL.

Ray, J. K. (2003) Advanced GPS Receiver Technology. (ENGO 699.73 Course Notes, Department of Geomatics Engineering, University of Calgary).

Smith, D. R. (1997) Channel Models. J. D. Gibson, ed., *The Communications Handbook*, Chapter 11, 131–140. CRC Press / IEEE Press, Boca Raton FL.

Steingass, A. & A. Lehner (2003) Land Mobile Satellite Navigation - Characteristics of the Multipath Channel. *Proceedings of ION GPS/GNSS 2003 (September 9-12, Portland OR)*, 1016–1022. US Institute of Navigation, Alexandria VA.

Syrjärinne, J. (2001) *Studies of Modern Techniques for Personal Positioning*. Ph.D. thesis, Tampere University of Technology.

USDoD (2001) Global Positioning System Standard Positioning Service Performance Standard. Available at http://www.igeb.gov/SPS-2001-final.pdf.

van Diggelen, F. (1998) GPS Accuracy: Lies, Damn Lies, and Statistics. *GPS World*.

Vishakantaiah, P. & W. J. Vogel (1989) LMSS Drive Simulator for Multipath Propagation. *Proceedings of NAPEX XIII*, 42–47. JPL, San Jose, CA.

Walpole, R. E., R. H. Myers, & S. H. Myers (1998) *Probability and Statistics for Engineers and Scientists, 6th Edition*. Prentice Hall, Upper Saddle River, NJ.

Weisstein, E. W. (2005) Noncentral Chi-Squared Distribution. From Mathworld–Wolfram Web Resources http://mathworld.wolfram.com/NoncentralChiSquaredDistribution.html (Accessed January 2005).

Appendix A

GPS Introduction

A.1 GPS Overview

A.1.1 System Concept

The Global Positioning System (GPS) is a satellite radionavigation system owned and operated by the United States Department of Defense. It was the first, and is currently the only, fully-operational example of a Global Navigation Satellite System (GNSS), although Russia has a partially-operational system in place (GLONASS) and the European Commission and the European Space Agency are currently developing their own GNSS, known as Galileo. The purpose of a GNSS is to provide continuous, accurate positioning and navigation information to users worldwide. GPS was specifically intended for use by the American military and its allies, but its civilian applications have grown to the point that civilian users now far outnumber military users.

The GPS actually consists of three main segments: the space segment, comprising the GPS satellites in space and the signals they broadcast; the control segment, comprising a number of ground control and monitoring stations; and the user segment, comprising all GPS receivers designed for positioning and navigation (Hoffman-Wellenhof et al., 2001). While not generally considered to be a component of the GPS system, the signal propagation channel could be considered a fourth, uncontrolled segment, because varying signal channels have a direct effect on the utility of GPS or any GNSS.

The principles of operation of GPS are discussed in the following sections. While other references should be consulted for a detailed overview of the GPS system, the concepts particularly relevant to the research conducted in this thesis are presented herein. Parkinson & Spilker (1996) is a comprehensive resource covering all of the information contained in this Appendix.

A.1.2 Multilateration and the GPS Constellation

GPS positioning is based on a multilateration technique. A user (receiver) may compute his own position and time by using the distances from four or more known positions; in GPS, these known positions are the locations of satellites in precisely-known orbits. Each satellite continuously broadcasts a description of its own orbit along with a timing signal; these signals are then easily converted to distance by the receiver using the known speed of radio propagation (299 792 458 m/s in a vacuum). Due to synchronization issues, true ranges cannot be received from GPS satellites, but rather pseudoranges are received, which have an unknown bias that is common to all observed ranges. The bias is, in fact, a receiver timing error which is solved in the same manner as position-domain variables: computation is done by adjustment of these pseudorange observations to estimate a position. The solution is based on a least-squares adjustment, and generally results in position accuracies within several metres.

Using multilateration as the basis for a GNSS requires that the minimum number of ranges, four, be available to a user at any time. GPS employs a nominal constellation of 24 satellites in Medium Earth Orbit (MEO); the satellites are distributed in six orbital planes, each inclined approximately 55° from the equatorial plane. This constellation ensures that a user anywhere on Earth will view at least 8 satellites above the horizon at any time - more than the minimum of 4 satellites required for a position fix. The constellation is also designed to ensure a fairly even distribution of satellites throughout the visible hemisphere, as geometry of the constellation is a major factor in positioning accuracy.

A.1.3 Availability and Accuracy

A simple measure of system availability is the coverage of Earth's surface over time. With this metric, system availability is 100%, as at least 8 satellites are visible at any time and place. However, this availability measure is based on the assumption of open-sky conditions, with a direct line-of-sight (LOS) available between all satellites and a receiver. Myriad environments exist in which the weak GPS signal cannot be received with enough power to measure pseudorange. The signal degradations caused by complete RF blockage, attenuation, and multipath are significant in most indoor locations and many outdoor ones such as urban canyons. In situations like that, the satellite-to-receiver channel can be considered as a fourth segment of the GPS system—one that is not controlled, but has serious effects on positioning.

Accuracy of positioning by GPS depends on several factors. These factors may include any or all of the following:

- Receiver processing techniques
- Satellite constellation geometry (dilution of precision - DOP)
- Satellite position errors (orbital errors)

- Satellite timing errors (clock errors)
- Atmospheric propagation errors
- Receiver timing errors (clock errors)
- Measurement noise
- Multipath

Of the above list, the only factor which cannot be mitigated to some extent by receiver techniques (user segment) is satellite constellation geometry; techniques have been developed to mitigate the errors caused by all of the other factors. Satellite timing and orbital errors, and atmospheric propagation errors are mitigated to a large extent by the use of differential GPS (DGPS), which eliminate these highly-correlated errors over short distances. For the remaining, more random errors, advanced processing techniques are constantly being developed to minimize their effects. Refer to Parkinson & Spilker (1996), Ray (2003), Lachapelle (2002), Hoffman-Wellenhof et al. (2001), and others for details of common error mitigation techniques.

A.2 GPS Signal Structure and Ideal Propagation

GPS provides two separate navigation signals, broadcast on two frequency bands: The coarse/acquisition (C/A) code is broadcast on the L1 carrier at 1575.42 MHz, and the precise (P(Y)) code is broadcast on both the L1 and L2 (1227.60 MHz) carriers. As this research is concerned primarily with effects on the civil signal, the structure of the C/A code on the L1 carrier is discussed.

A.2.1 Ideal GPS Signal and Propagation Effects

Time-Domain Signal Representation

The GPS system uses a code division multiple access (CDMA) technique to divide its allotted spectrum among transmitting satellites. The civil (C/A) signal is a pseudorandom noise (PRN) code with a chip rate of 1.023 Mcps and length 1023 chips, or 1 ms. There are 32 separate PRN codes available for GPS use, with low cross-correlation between each. The PRN code is modulo-2 added to a navigation data message with a bit rate of 50 bps. This combined code, with overall rate of 1.023 Mcps, modulates the L1 inphase carrier at 1575.42 MHz. The same frequency also carries the P(Y) code, which is a 10.23 Mcps CDMA signal; the two signals modulate the carrier in phase quadrature, resulting in minimal interference—the P(Y) code is considered simply as a noise source for purposes of this thesis.

The civil signal transmitted by each GPS satellite is represented below:

$$L1_{C/A}(t) = C_n(t)M_n(t)\cos(2\pi f_{L1}t) + n(t) \tag{A.1}$$

where $C_n(t)$ = Pseudorandom noise C/A code for PRN “n”

$M_n(t)$ = Navigation data message for PRN “n”

f_{L1} = L1 frequency (1575.42 MHz)

$n(t)$ = additive noise

Each GPS satellite is in a 12-hour orbit with radius of approximately 26 500 km. These orbits result in observed satellite distances ranging from a maximum of approximately 25 700 km at the horizon to a minimum of approximately 20 100 km as satellites pass directly overhead. The time derivative of the range (range rate) varies from a maximum of approximately 1000 m/s at the horizon to 0 m/s at the zenith, causing a Doppler effect of up to 5 kHz as observed on the earth's surface. The nominal carrier frequency is therefore seen to vary from approximately 1575.415 MHz to 1575.425 MHz.

The civil signal, as received at Earth's surface, is represented below:

$$L1'_{C/A}(t) = \sum C'_n(t) M'_n(t) \cos\left(2\pi(f_{L1} + f_d n)t + \phi_n(t)\right) + n(t) \tag{A.2}$$

where $C'_n(t)$ = Delayed, Doppler shifted C/A code for PRN "n"

$M'_n(t)$ = Delayed, Doppler shifted navigation data for PRN "n"

f_d = Doppler frequency for PRN "n"

$\phi_n(t)$ = Carrier phase shift for PRN "n"

Without considering propagation effects, the received signal for any given PRN should be identical to the transmitted signal, except that it is delayed in time and experiences a Doppler shift.

Spectrum of C/A Code at Baseband

The PRN codes employed by GPS are an implementation of a direct-sequence spread spectrum multiple access system. All satellites' signals share a common spectrum, with individual signals being identifiable by their (nearly) mutually-orthogonal PRN codes.

The basic function forming the C/A code sequence is a rectangular pulse of duration 977.5 ns. The modulo-2 addition of the 50 bps navigation message has no effect on this basis function since it is exactly synchronized with the C/A code word. The magnitude spectrum of the PRN sequence is a sum of impulses (Dirac delta functions) falling within the envelope of $(P_s/f_c)\mathrm{sinc}^2(T_C f)$ where T_C is the chip period, P_s is the total signal power, and f_c is the frequency of the PRN code chip sequence (Parkinson & Spilker, 1996). The sinc-squared envelope has its first null at $\pm(1/T_C)$ Hz, with subsequent nulls located at multiples of T_C away from the centre frequency. Based on the chip frequency of 1.023 MHz, the main lobe width of the C/A code magnitude spectrum is 2.046 MHz, with side lobes extending infinitely.

The main lobe contains approximately 90% of the power of the signal, with over 98% contained within ±5 MHz of the centre frequency. The basic form of the power spectrum of the C/A code is shown in Figure A.1

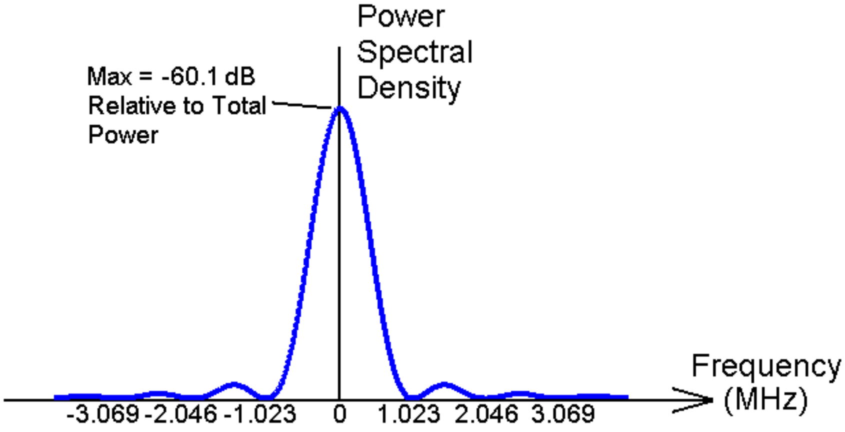

Figure A.1: C/A Code Power Spectrum at Baseband

Spectrum of Broadcast C/A Code on L1 Inphase Carrier

The inphase carrier at the time of transmission can be considered to be a cosine at the nominal L1 frequency with zero phase offset:

$$x_t(t) = \cos(\omega t) = \cos(2\pi f t) \tag{A.3}$$

where $x_t(t)$ = GPS L1 carrier for transmission

f = carrier frequency in Hz (1575.42 MHz)

ω = carrier frequency in rad/s (9.89866×10^6)

In the frequency domain, the carrier is represented by a pair of delta functions at $\pm\omega$, with phase response of 0 (no phase shift). The propagation time and Doppler shift have the effect of making the received carrier shift in frequency and adds an unknown phase shift:

$$x_r(t) = \cos\left((\omega + \omega_d)t) + \phi\right) \tag{A.4}$$

where $x_r(t)$ = GPS L1 carrier as received on earth

ϕ = phase offset in radians

ω_d = Doppler frequency

The received carrier's magnitude spectrum is represented by a delta function at $\pm(\omega + \omega_d)$. The phase spectrum at these frequencies is a constant $(0 \pm \phi)$ in both the positive and negative frequency regions.

The effect of modulating the L1 carrier with the C/A code is a translation of the C/A code magnitude spectrum from baseband to the Doppler-shifted L1 frequency. The power spectral density is also halved. The phase shift caused by the propagation distance is as described in Equation A.2

A.3 GPS Receiver Operations

GPS receivers consist of three basic segments: RF front end, signal processor, and navigation processor. These segments are discussed here for the reader unfamiliar with the GPS receiver.

A.3.1 RF Front End

The RF front end consists of an antenna, filters, amplifiers, and mixers intended to condition the signal for quantization and signal processing.

Reception and Filtering

The GPS signal is filtered on reception. The bandwidth of the signal is theoretically unlimited, but it is filtered by GPS satellites on transmission to a 20 MHz two-sided bandwidth. Most of the power is contained within several megahertz of the centre frequency. A filter of approximately 10.23 MHz width (from 1570.42 to 1580.42 MHz) passes over 99% of the spectral power. Realizable filters have some amplitude rolloff, however for theoretical purposes we will consider only linear "brick-wall" filters with linear phase response. This filter rejects all out-of-band frequency components, passes all in-band components with zero magnitude adjustment, and has linear phase response within the passband, introducing no distortion.

Downconversion to Intermediate Frequency (IF)

The received and filtered RF signal is downconverted by analog means to an intermediate frequency to make quantization possible at a reasonable rate. The downconversion method may use multiple IFs, or may use a single-stage downconversion. The IF is chosen based on the signal bandwidth, and the speed of analog-to-digital conversion available, in order to avoid introducing distortion of the signal.

A single-stage downconversion is discussed in this section. The downconversion oscillator is mixed with the received and filtered RF signal and then filtered to eliminate high-frequency components. The local oscillator is represented herein as having no phase offset. A local phase offset is a constant which is absorbed during least-squares adjustment, and thus can be ignored. Considering now only the information transmitted by a single satellite, the downconversion operation is described. Downconversion on a sum of signals from multiple satellites is a linear operation.

Received signal:

$$x_R(t) = CA'_n(t)M'_n(t)\cos(\omega_n t + \phi_n) \tag{A.5}$$

where $x_R(t)$ = received signal for single PRN

$CA'_n(t)$ = digital C/A code for satellite "n"

$M'_n(t)$ = digital navigation message for satellite "n"

ω_n = nominal carrier frequency + Doppler for satellite "n"

ϕ_n = phase offset at receiver for satellite "n"

Local oscillator:

$$x_{LO}(t) = 2\cos(\omega_L t), \tag{A.6}$$

where $x_{LO}(t)$ = local oscillator signal

ω_L = synthesized local oscillator frequency (rad/s)

Mixing the two signals results in the following:

$$x_{IF}(t) = CA'_n(t)M'_n(t)\Big[cos((\omega_n - \omega_L)t + \phi_n) + cos((\omega_n + \omega_L)t + \phi_n)\Big] \tag{A.7}$$

where $x_{IF}(t)$ = IF signal suitable for sampling

Filtering the high-frequency component leaves:

$$x_{IF}(t) = CA'_n(t)M'_n(t)\Big[cos((\omega_n - \omega_L)t + \phi_n)\Big] \tag{A.8}$$

Of course, recall that the received signal is a sum of signals from multiple satellites, giving the general form of the IF signal:

$$x_{IF}(t) = \sum_n CA'_n(t) M'_n(t) \Big[cos((\omega_n - \omega_L)t + \phi_n) \Big] \tag{A.9}$$

Distortion may occur if the positive and negative frequency components of the signal are allowed to overlap after downconversion. This may be avoided by ensuring that the IF frequency is chosen to be at least one half of the RF bandwidth. If this requirement is not met, sampling of both inphase and quadrature signals is required to receive the signal.

A.3.2 Signal Processing

Signal processing is usually done in the digital domain, so an analog-to-digital converter is the usual link between the RF front end and signal processor.

The purpose of the signal processing segment of a GPS receiver is to extract the pseudorange, carrier phase, Doppler, and navigation information from the received RF signal. Modern receivers have 12 to 24 channels, each of which is designed to process data from a single satellite on either the L1 or L2 frequencies. The operations on a single channel are discussed.

Doppler Removal

The final conversion to baseband, involving removal of the residual IF and Doppler, is generally done in digital processing. The process is illustrated here in analog terms for simplicity, however the operations are equivalent.

The IF + Doppler carrier is removed through mixing with a sinusoid of the appropriate frequency and lowpass filtering to remove the double-frequency harmonic.

This operation is done on both an inphase and quadrature channel to obtain two separate signals:

$$\begin{aligned} x_{IF}(t) &= CA_n'(t)M_n'(t)cos(\omega_I Ft + \phi_n) && \text{(A.10)} \\ x_L^I(t) &= 2\cos(\omega_L t) && \text{(A.11)} \\ x_L^Q(t) &= 2\sin(\omega_L t) && \text{(A.12)} \\ &= 2\cos(\omega_L t - \frac{\pi}{2}) && \text{(A.13)} \end{aligned}$$

Mixing the IF signal with the local signals gives the following:

$$\begin{aligned} x_{BB}^I(t) &= CA_n'(t)M_n'(t)[[cos((\omega_{IF} - \omega_L)t + \phi_n) + \\ &\quad cos((\omega_{IF} + \omega_L)t + \phi_n)] && \text{(A.14)} \\ x_{BB}^Q(t) &= CA_n'(t)M_n'(t)[[cos((\omega_{IF} - \omega_L)t + \phi_n - \frac{\pi}{2}) + \\ &\quad cos((\omega_{IF} + \omega_L)t + \phi_n - \frac{\pi}{2})] && \text{(A.15)} \end{aligned}$$

With a properly-chosen frequency plan, the higher frequency component will fall outside of the baseband filter bandwidth used in the previous stage, and can thus be removed. Additionally, if the local oscillator is correctly tuned to match the IF + Doppler frequency, it completely removes the carrier resulting in the following signals:

$$\begin{aligned} x_{BB}^I(t) &= CA_n'(t)M_n'(t)cos(\phi_n) && \text{(A.16)} \\ x_{BB}^Q(t) &= -CA_n'(t)M_n'(t)cos(\phi_n - \frac{\pi}{2})] && \text{(A.17)} \end{aligned}$$

Each of the above baseband signals is an amplitude-scaled replica of the transmitted signal, with the phase offset providing a constant amplitude scaling.

Correlation and Integration

The received, baseband signal is mixed with a local copy of the digital ±1 C/A spreading code, an operation termed *correlation*. With the correct offset, the correlation of the C/A code with itself gives a constant value of 1. The navigation data can be ignored if integration times are under 20 ms (and bit-synchronized). In order to precisely remove the C/A code, the local code must have its period adjusted to account for the Doppler frequency of the received C/A code. In short integrations, this is not a concern, but becomes serious for longer integrations.

Integration is the process of adding received and correlated signal samples for a certain time period, normally up to 20 ms. The accumulation is essentially a convolution of the received signal with a rectangular time window of length T. Convolution in the time domain is equivalent to multiplication in the frequency domain. Thus, the integration operation is equivalently a filter which removes higher-frequency noise and co-channel interference while passing the de-spread signal. This yields processing gain.

Processing Gain Equations

Processing gain is realized by accurately de-spreading and demodulating the signal of interest, while rejecting noise and some co-channel interference by filtering. The operation is illustrated in Figure A.2 showing the amplitude spectrum of the GPS signals and noise. The single-sided convention for bandwidth B is used because data used in this thesis were provided at baseband. In Figure A.2, the narrower filter illustrated is not actually a constant gain filter, but is sinc-squared shaped and has rectangular equivalent single-sided bandwidth of $1/(2T)$ as shown in the figure.

Initial noise, shown as the grey shaded area, is $N = BN_o$. After filtering, the noise is reduced to $N = N_o/(2T)$. Assuming co-channel interference is negligible, and all power from the signal of interest is de-spread to a small bandwidth, the ratio of original noise to filtered noise gives the processing gain as

$$G = 2BT. \tag{A.18}$$

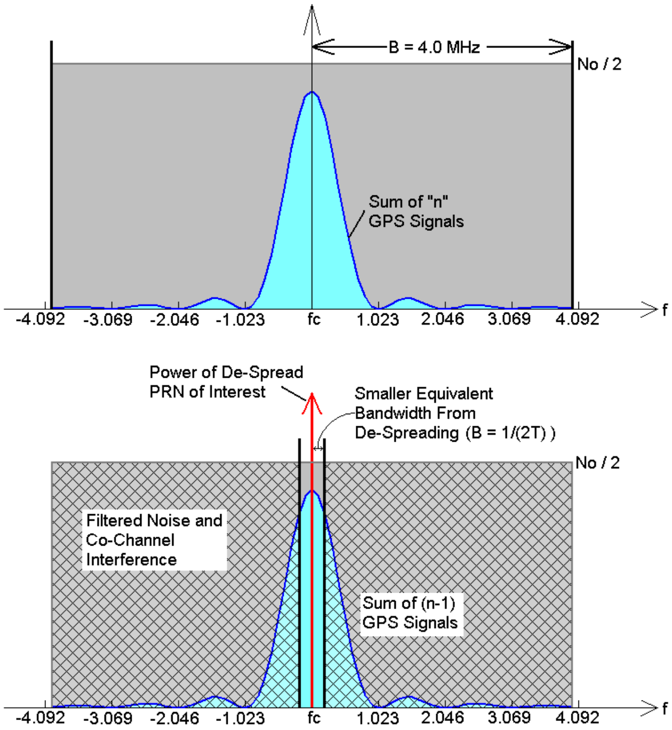

Figure A.2: Processing Gain as a Filtering Operation

The standard processing gain equation does not accurately account for co-channel interference which is non-white. With the GPS civil signal, power is spread to a first-null width of 1.023 MHz, but the highest power spectral density of the signal is still found at the nominal carrier frequency. Therefore, reducing noise equivalent bandwidth by a factor of $2BT$ reduces white noise power by that factor, but co-channel interference is not attenuated linearly because of its lower PSD away from the nominal carrier frequency. This is seen in Figure A.2 as the filtering operation clearly does not attenuate interfering GPS signal power linearly as the filter bandwidth is reduced by increasing integration time.

The non-linear nature of co-channel interference attenuation is significant only if that interference is a significant contributor to overall noise+interference. In most cases, the combined power from up to 12 GPS satellites remains significantly below thermal noise, largely due to attenuation of signals by antenna gain patterns. In general, therefore, we consider the standard processing gain equation accurate. As well, the relative attenuation of noise and co-channel interference is nearly identical for increases in integration time above 1 ms. The PSD of interfering GPS signals is nearly constant within 1 kHz of the nominal carrier frequency, and it thus undergoes nearly linear attenuation as the noise equivalent bandwidth is reduced from 1 kHz by further integration.

Carrier and Code Tracking

For real-time operations, the changing code offset and Doppler frequency are tracked with a delay-locked loop (DLL) and phase-locked loop (PLL) respectively.

DLL Overview The received signal is correlated with a local C/A code using, usually, three different offsets. The *prompt* correlator represents the best current estimate of the actual offset of the code. The *early* and *late* correlators are offset some fraction of a chip earlier and later than the prompt correlator.

Based on the ideal C/A code autocorrelation function, which is triangular with width of 2 chips, the relationship between early, prompt, and late correlators is precisely defined for any code offset. These values are therefore input to a discriminator which determines the current offset from the actual code offset at any time. The discriminator output is filtered and fed back to the local C/A code generators to adjust timing, completing the delay-locked loop. DLL design factors determine how successfully a receiver can track a signal under conditions of changing delay or multipath distortion.

PLL Overview The Doppler removal operation is simultaneously conducted with an inphase carrier and a quadrature carrier, which are 90° offset from one another. The goal of the PLL is to ensure that the incoming carrier phase is matched by the local inphase carrier. Ideally, therefore, all of the signal power should be measured on the inphase branch and none on the quadrature branch.

The power on each branch is compared by the carrier phase discriminator, which provides an estimate of the phase error. This output is filtered and fed back to the receiver's local oscillator to adjust carrier phase and maintain phase lock. Similar to the DLL, the PLL's ability to track a carrier in noise and with certain Doppler dynamics depends on its design factors.

A.3.3 Navigation Processing

Position, velocity, and time are computed by the navigation processor using the raw pseudorange, Doppler, and navigation bit stream provided by the signal processor. The navigation processor must decode the 50 Hz navigation data and compute GPS satellite positions. With that information, it can then estimate position and time by least-squares adjustment of pseudoranges. With accurate position information, Doppler measurements can also be used to precisely estimate velocity.

The algorithms and techniques used in navigation processing vary with each receiver implementation, and depend on the purpose for which the receiver is intended. Beyond the typical least-squares approach, some receivers implement heavy filtering of position and time, or use other error detection and mitigation techniques.

Least-Squares Adjustment

The process of least-squares adjustment is not discussed in detail here. Least-squares adjustment is a commonly-used technique that is widely discussed in the literature. This discussion is based on information in Krakiwsky (1990), which provides detailed discussion of least-squares methods and implementation, and Hoffman-Wellenhof et al. (2001). Some important concepts are reviewed herein to provide background on accuracy measures of GPS positioning.

GPS position computation is a parametric estimation problem. Observations, $\mathbf{l}$, consist of measured pseudoranges. These observations are related to the parameters of interest, $\mathbf{x}$, by a *design matrix*, $\mathbf{A}$. That is to say,

$$\mathbf{l} = \mathbf{A}\mathbf{x}. \tag{A.19}$$

The parameters include three geometric parameters—perhaps latitude, longitude, and height—and a time parameter. $\mathbf{A}$ is a matrix representation of the mathematical equations that relate the pseudorange observations to the four parameters. Ideally, in the absence of measurement errors, Equation A.19 has a unique solution. However, measurement errors do exist and adjustments are necessary to solve for the parameters. A vector of corrections, termed *residuals* ($\mathbf{r}$), is required to result in a unique solution. In addition, the resultant parameter estimates consist of the actual parameter values and some estimated adjustments δ.

$$\mathbf{l} + \mathbf{r} = \mathbf{A}\mathbf{x} + \delta. \tag{A.20}$$

The least-squares solution is found by minimizing the residuals according to the condition

$$\hat{\mathbf{r}}\mathbf{P_l}\hat{\mathbf{r}} + \hat{\delta}\mathbf{P_x}\hat{\delta} = \text{minimum}, \tag{A.21}$$

where $\hat{\mathbf{r}}$ and $\hat{\delta}$ are the best estimates of the vectors of residuals and parameter adjustments respectively. $\mathbf{P_l}$ and $\mathbf{P_x}$ are weight matrices related to the variance-covariance matrices $\mathbf{C_l}$ of the observations and $\mathbf{C_x}$ of the parameters. The variance-covariance matrices represent the quality of the associated measurements or parameters.

The detailed method to conduct the adjustment required to satisfy the condition of Equation A.21 is left to more comprehensive references. The key concept to understand for determining GPS accuracy is that the design matrix, $\mathbf{A}$, is a matrix representation of the geometry of positioning.

Estimating Accuracy of Position & Time

GPS receivers output, along with position and time, an estimate of the accuracy of those parameters. Accuracy is estimated with two basic elements of the least-squares operation: the level of adjustment required, represented by the residuals, and the geometry of positioning, represented by dilution of precision (DOP).

Residuals indicate how much error is present in individual measurements. Low residuals indicate good pseudorange estimates, whereas large residuals indicate that the measurements have significant errors. Receivers use various methods to convert residuals to an estimate of measurement accuracy.

Geometry of positioning is determined from the cofactor matrix $\mathbf{Q_X} = (\mathbf{A^T A})^{\mathbf{-1}}$ where $\mathbf{A^T}$ is the transpose of the design matrix. This is a square matrix with dimensions 4-by-4 that can be used to define DOPs. The main diagonal elements of the cofactor matrix are used in various combinations to give DOP in the direction of interest. Common versions of DOP include horizontal (HDOP), vertical (VDOP), geometric (GDOP), position (PDOP), and time (TDOP).

DOP values are used with the estimated accuracy of measurements to give geometric accuracy. For example, horizontal accuracy is obtained by multiplying the measurement accuracy of the pseudoranges by the horizontal DOP (HDOP) value. If user equivalent range error (UERE) is 10 m and HDOP is 1.5, the horizontal position accuracy is on the order of 15 m.

A number of statistics are used to represent positioning accuracy. Common statistics include 3D RMS error, 2DRMS (twice the horizontal RMS error), spherical error probable, and circular error probable (van Diggelen, 1998). In this thesis, all accuracy is reported as RMS error in a single dimension to avoid the confusion of using multiple accuracy measures.

Appendix B

Software Overview

B.1 Input Files

CorrTool is configured by the user to analyze a specific PRN within a raw data set with whatever parameters are desired. The input files used by CorrTool are discussed in this section with listings provided as appropriate.

B.1.1 Raw GPS Data File

Data is in binary form with one byte per sample. Each byte contains three bits for the inphase sample, three bits for the quadrature sample, one synchronization bit, and one unassigned bit. The raw data file may be of any size.

B.1.2 SV Info File

For each data set, the user must provide a listing of information for the SVs thought to be visible at the time of test. This file includes one row per SV, with the following data for each SV (in order from left to right): PRN, initial Doppler, initial Doppler drift, initial code phase, milliseconds since last navigation transition, and Doppler jerk parameter. The fifth parameter—milliseconds since last navigation transition—is a vestige of previous software design and is no longer used. A sample info file is shown in text format in Listing 1, although the real file must be input in .mtx format.

B.1.3 Navigation Data File

Navigation data is also stored in .mtx format. The file contains one column for each of the PRNs from the SV info file listed above. Each column consists of entries that have two parts: a sign, and a sample number. The sample number represents the best estimate of the point within the raw data file where a navigation bit transition may occur for that PRN, whether a transition occurs or not. The sample number is given a positive or negative sign, indicating the state of the navigation bit during the epoch commencing at that sample number.

For a data set of 60 s duration, there are therefore approximately 3000 entries in each column of the navigation data file.

B.1.4 User Option File

CorrTool's behaviour is controlled by a text option file, a sample of which is presented in Listing 2 below. The entries regarding filenames are self-explanatory. The remaining entries are explained:

Channel Number determines which PRN will be analyzed. This is a number representing a row in the SV info file, with the first row having the index 0.

Milliseconds to Skip sets the starting point within the raw data file for analysis.

Num Correlators is the number of correlators with which to examine the signal. The total search space is defined by spreading this number of correlators out by the spacing.

Correlator Spacing is the spacing between correlators, in chips.

Num Frequency Bins is the number of Doppler frequency bins to test. The total Doppler search space is defined by spreading this number of bins out by the spacing.

Frequency Bin Spacing is the spacing in hertz between frequency bins.

Coherent Correlation Length is the length of each coherent correlation.

B.1.5 Mask File

The program conducts correlations at code and frequency offsets centered on the presumed code phase and frequency. This presumed correlator location is defined by the initial code phase, Doppler frequency, and the Doppler model. The search space is defined by the number and spacing of the code and frequency bins defined by the option file. Thus, if 25 correlators and 15 frequency bins are used, a total of 375 individual correlator locations are examined, centered on the presumed code phase and frequency.

A mask file may be used to selectively eliminate some of the correlators nominally tested. The purpose is to allow targeting of specific areas of the code-frequency ambiguity domain in high resolution while minimizing processing time. The file is in .mtx format, with the number of columns and rows equal to the number of correlators and frequency bins (respectively) defined in the option file. A correlator will be examined as usual if the mask file entry is 1, and ignored if the entry is 0.

The mask file name is an optional parameter used in command line execution of CorrTool.

LISTING 1: SAMPLE SV INFO FILE

```
3   -1033.836      -0.640411      983.53     6     0.00004026
8    -264.650      -0.597159      680.02    19    0.000015116
10  -2105.814      -0.579828     708.625    13     0.00007784
15   2141.441      -0.558431      144.34     4    -0.00008863
17  -2483.780      -0.450218      427.19     6     0.00010767
21   -448.423      -0.676747      941.59     6     0.00002684
26   3121.033      -0.340364       98.21    12    -0.00008129
27  -1959.303      -0.374406      944.04    14     0.00004246
28   2996.620      -0.368817       400.3    11    -0.00008192
29   2042.947      -0.426445       872.4    14    -0.00006408
31   1095.659      -0.679708     822.885     9    -0.00005614
```

LISTING 2: SAMPLE USER OPTION FILE

```
** OptionFiles for Correlation Program **

General
  Name of Raw Data File       : C:\Data\terr_ref.dat
  Name of Nav Data File       : C:\Data\TerrNavData_Complete.mtx
  Name of Info File           : C:\Data\TerrRefInfo.mtx
  Channel Number              : 2

Data Options
  Milliseconds to Skip        : 10000

Correlation Options
  Num Correlators (odd #)           : 25
  Correlator Spacing                : 0.1
  Num Frequency Bins (odd #)        : 15
  Frequency Bin Spacing (Hz)        : 0.75
  Coherent Correlation Length (ms)  : 200
**************************************************************
```

B.2 Program Flow

CorrTool is invoked at a command prompt in one of two modes: single-epoch or sequential. In single-epoch mode, a single correlation search is conducted for the epoch specified by the start time and the coherent integration length. In sequential mode, the process repeats for a user-defined period. It outputs a set of results for each epoch and a summary file listing the peak code offset and Doppler frequency in each epoch. The program execution, with data flow, is presented in Figures B.1–B.4.

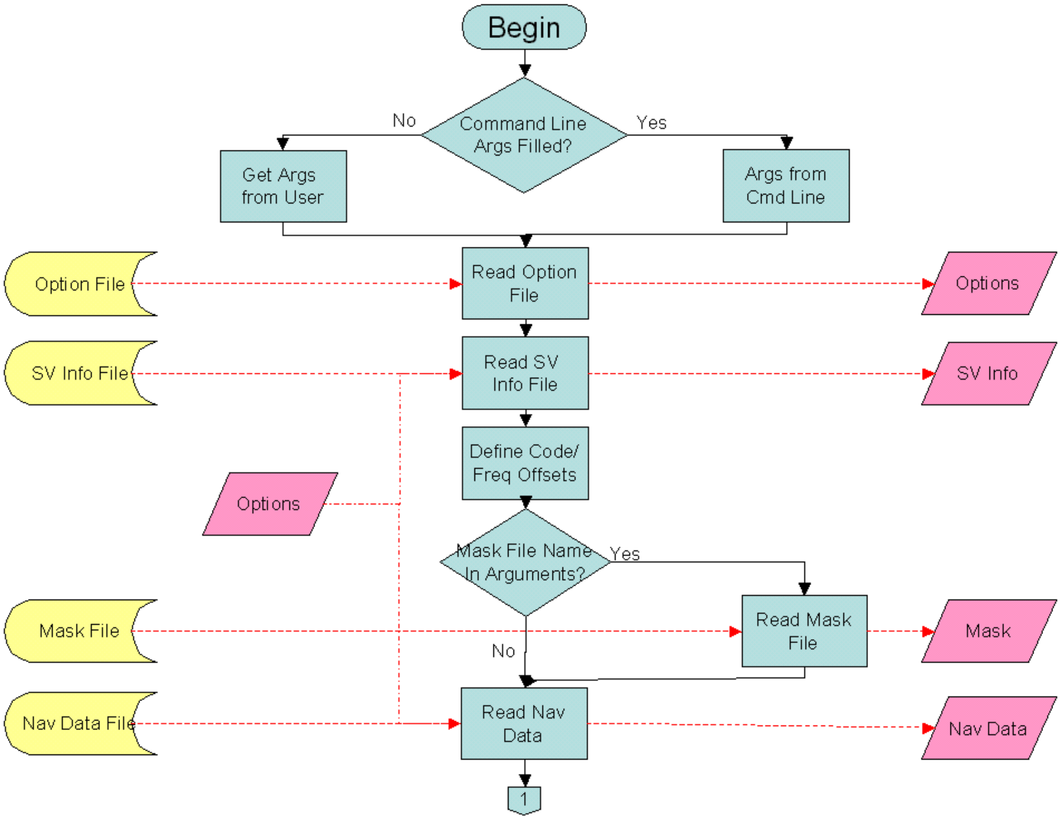

Figure B.1: CorrTool Program Flow With Data (1/3)

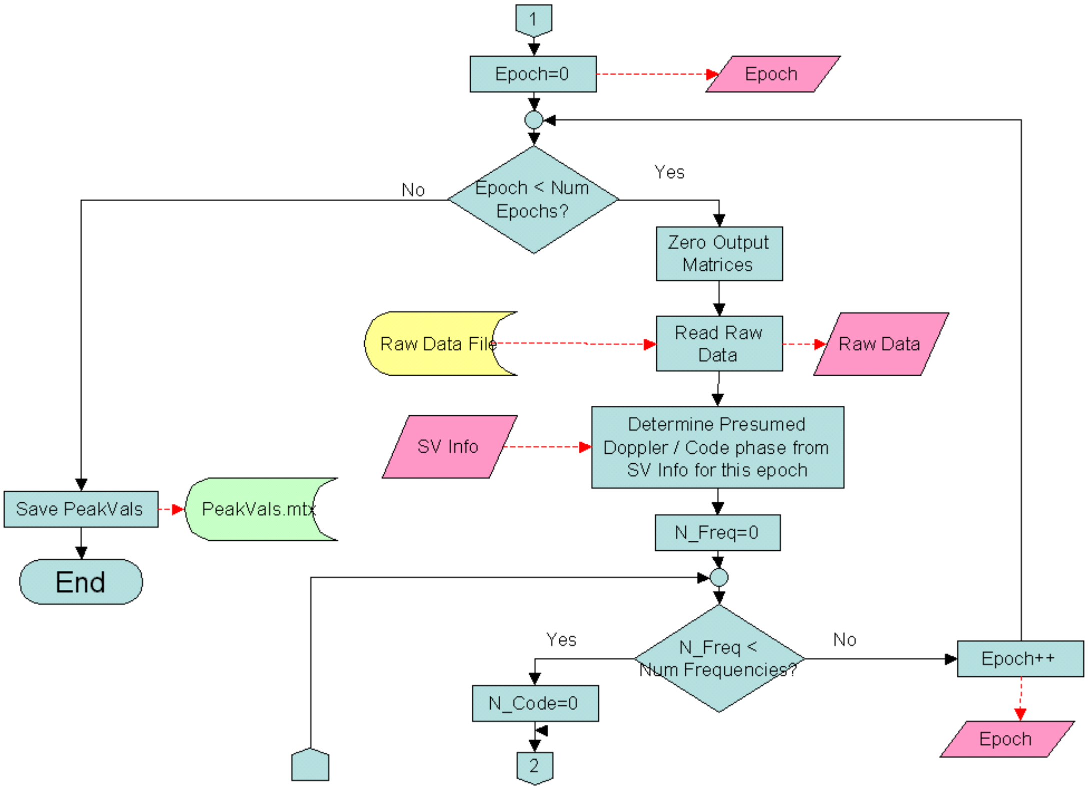

Figure B.2: CorrTool Program Flow With Data (2/3)

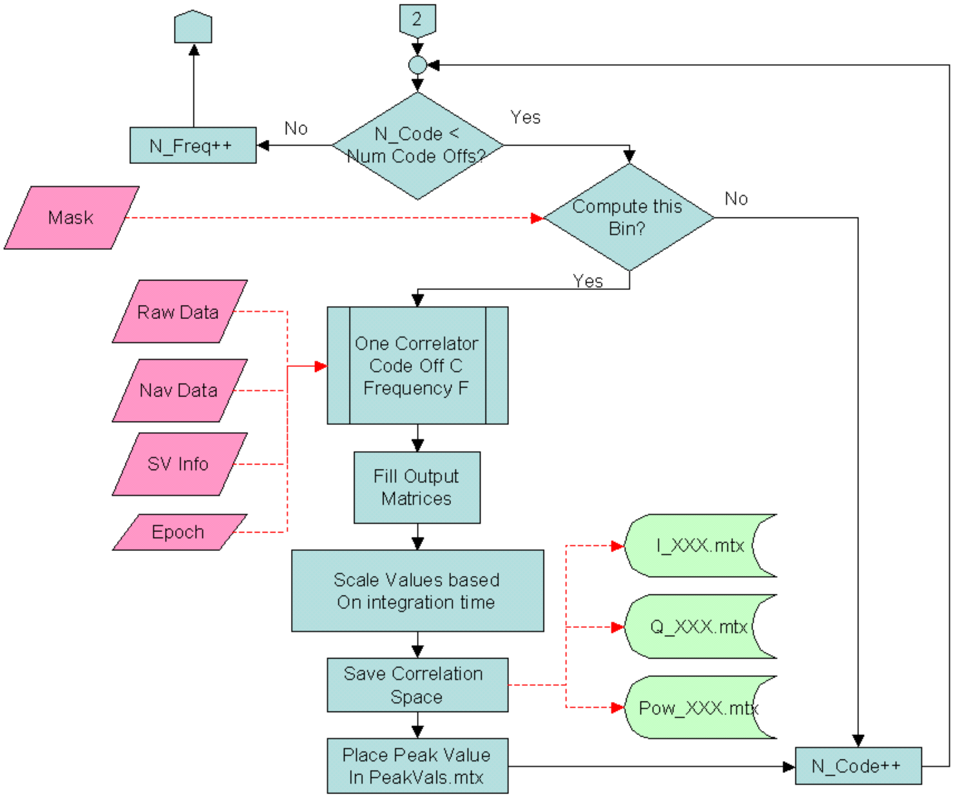

Figure B.3: CorrTool Program Flow With Data (3/3)

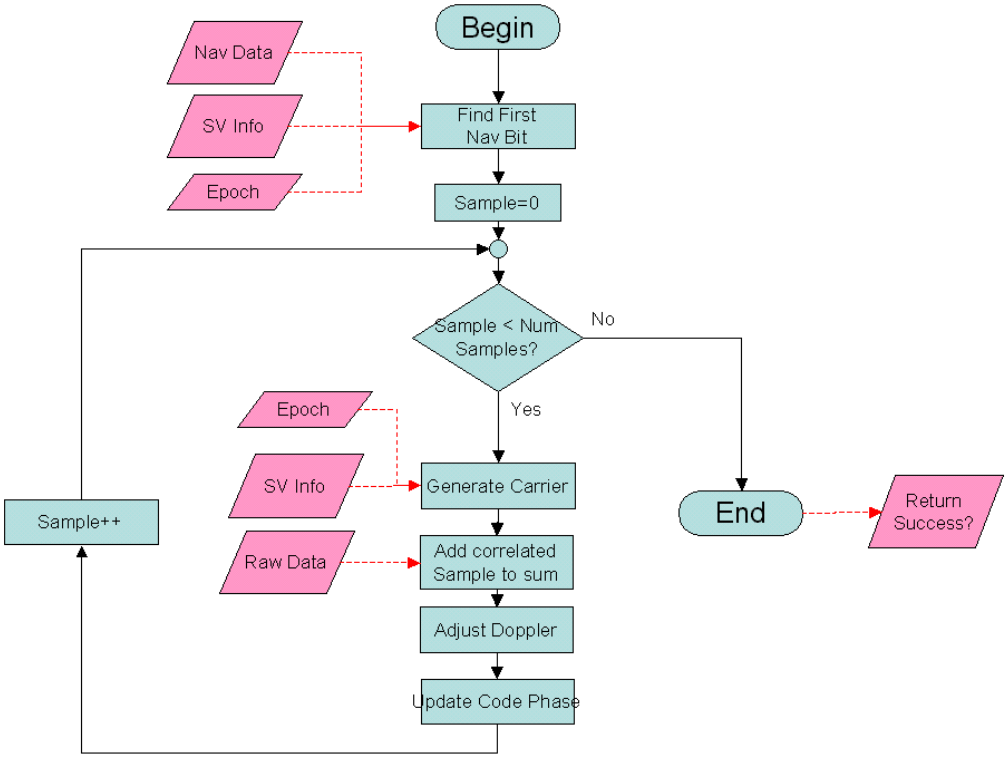

Figure B.4: *One Correlator* Subroutine Flow With Data

Appendix C

Navigation Data Verification

The integrity of navigation data has been verified using two approaches. First, the data recorded for each PRN was partially decoded to verify the accuracy of several parts of the navigation message. Following that, a more thorough approach was undertaken to verify the bit transition, or lack thereof, at each possible boundary. The two methods are discussed in the following sections.

C.1 Message Decoding

Each subframe begins with an 8-bit preamble, followed by a 22-bit telemetry word. The subsequent 30 bits contain a handover word (HOW) containing information on GPS time of week and other basic flags. The remaining 8 words in each subframe contain almanac, ephemeris, and correction data that changes with each subframe (ICD200C, 2000). For decoding purposes, the first two words have identical format regardless of the subframe number. Only the following data elements have been tested for each of the 9 occurrences of a subframe beginning in each data set:

- Preambles in correct location and with consistent phase (8 bits)
- Correct TOW in all subframes (17 bits)
- Anti-Spoofing flag asserted for all subframes (1 bit)
- Alert flag de-asserted for all subframes (1 bit)

- Subframe ID consecutive between subframes (3 bits)

This initial test showed no apparent errors for any PRNs among the 22 bits examined in each subframe. It is still possible that bit transition errors occur elsewhere in the data sets. Rather than decode the entire navigation data stream and compare with nominal values, a second verification approach was used to detect any errors missed by the partial data decoding, using the fact that no transition errors occur in the limited segments already tested to verify the approach.

C.2 Detection of Transition Errors

After Doppler modelling, it is possible to easily measure power at or near the actual peak of the correlation function throughout the data set, using the recorded navigation data to allow integration across bit boundaries. A series of 20 ms correlations were conducted on each PRN throughout the two data sets, giving 3000 samples of the peak power. Since the data set is not absolutely synchronized with navigation transitions, each 20 ms correlation is likely to cross over a bit boundary. If the bit transition is recorded incorrectly, the 180° phase shift will attenuate the power measured at that epoch. To account for the possibility of unintentional subframe synchronization, a second set of 20 ms correlations is conducted, but with the 20 ms correlations offset from the previous test by 10 ms. Thus, if the initial test were unintentionally synchronized with navigation data, the second test would be unsynchronized.

Bit transition errors are detected by finding power samples that are highly attenuated in either the zero-offset or 10 ms-offset test (or both). An incorrect transition serves to 'cancel' a portion of the received energy, in proportion to the fraction of the integration which is on each side of the bit boundary. Power attenuation levels due to incorrect bit transition for various synchronization errors in a 20 ms coherent integration are presented in Table C.1, using a nominal value of 1 to represent power received with no transition error.

Synchronization Error (ms)	Attenuated Peak Energy	Attenuated Peak Power	Power Loss (dB)
0	1.0	1.00	0.0
1	0.9	0.81	0.9
2	0.8	0.64	1.9
3	0.7	0.49	3.1
4	0.6	0.36	4.4
5	0.5	0.25	6.0
6	0.4	0.16	8.0
7	0.3	0.09	10.5
8	0.2	0.04	14.0
9	0.1	0.01	20.0
10	0.0	0.00	∞

Table C.1: Power Loss Due to Bit Transition Error

C.2.1 Example of Transition Error Detection

Power measurements using 20 ms integrations are shown in Figure C.1 for a data segment during which three navigation bit transition errors have been introduced intentionally at transition points near 4, 6, and 20 seconds. This particular data is centre correlator power for PRN 15 in the Tube data set. Based on the known subframe synchronization for that PRN, we determine that the 20 ms integrations in the zero-offset case straddle a navigation bit boundary by approximately 4 ms, and in the second case by approximately 6 ms. We therefore expect an attenuation of 4.4 to 8.0 dB relative to the average when a bit transition error occurs.

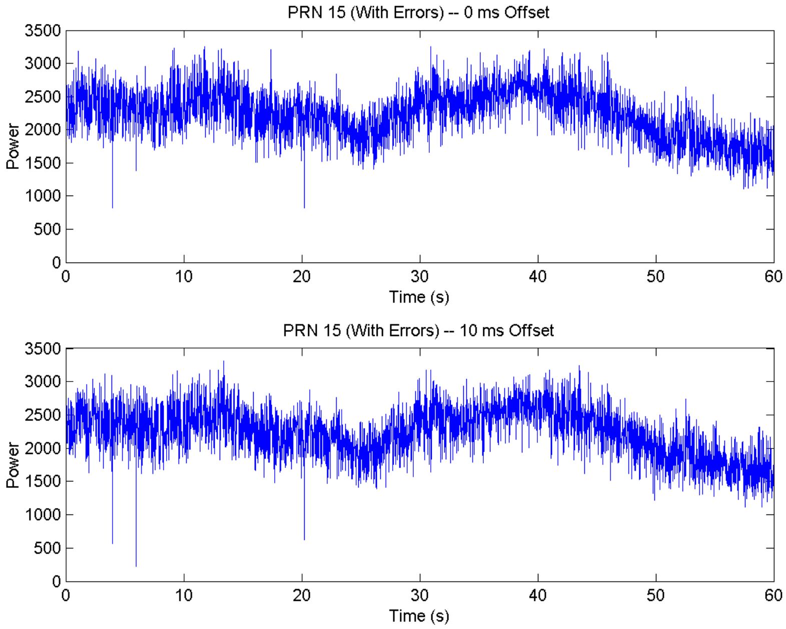

Figure C.1: Centre Correlator Power (20 ms) Showing 3 Transition Errors

The three errors introduced are clearly identifiable as severely attenuated power samples. In the zero-offset case, two samples with approximately 4.7 dB attenuation are observed, and one with 2.5 dB. The second, 10 ms-offset case shows the former two samples with attenuation near 5 to 6 dB, and the latter sample with attenuation increased to near 10 dB. The values of attenuation are not deterministic due to noise, but the observations appear reasonable and it is clear that bit transition errors can be identified using this method even for relatively weak signals.

C.2.2 Test Results

The methods described above confirmed that no navigation transition errors remained in the data sets after repairing one incorrect transition found in the data of PRN 8. Details of the measurements for each PRN in each data set are omitted for space considerations.

Appendix D

Examination of Doppler Effects due to SV Orbital Motion

This appendix examines satellite orbital motion over short periods to determine the degree of polynomial which may be required to describe the received Doppler with required accuracy over short periods. The general form of the polynomial approximation desired is

$$\dot{\phi}(t) = \sum_{n=0}^{N} a_n t^n, \tag{D.1}$$

where a_n is the polynomial coefficient for degree n and N is the order of polynomial.

D.1 GPS Orbital Models and Doppler Prediction

GPS satellite orbits are essentially Keplerian orbits with low eccentricity ($e < 0.03$). Certain non-ideal effects modify the orbits somewhat, but the GPS almanac represents the orbits as near-ideal ellipses, with only one non-Keplerian element. The almanac uses 8 parameters (ICD200C, 2000):

- e and $\sqrt{A}$ define the shape of the ellipse
- δ_i, ω, and $\Omega_\circ$ describe its orientation with respect to Earth
- $\dot{\Omega}$ represents the drift of the ellipse's orientation
  (the only non-Keplerian parameter)

- $M_\circ$ represents the position of the satellite within its orbit
- t_{oa} provides a reference epoch

The broadcast ephemeris is a superset of the almanac, consisting of the aforementioned 8 parameters and 8 additional correction parameters. The corrections are long-term elements which may be considered approximately constant for short periods such as 60 seconds. Thus, an ellipse with low eccentricity should be sufficient to describe SV dynamics as viewed by a user at some point on Earth's surface. Considering that simple model, it seems reasonable to search for a lower-order description of the resultant Doppler effect as viewed by that user, assuming some initial conditions. The dynamics of the Doppler effect are examined in the following section to determine the degree of polynomial necessary to model the Doppler effect over a short period.

D.2 Analysis of Worst-Case Doppler Dynamics

The received Doppler undergoes maximum dynamic effects when a satellite passes from horizon to horizon through the zenith. That will therefore be considered the worst case for attempting to predict Doppler using polynomial models. For this examination, the satellite orbit is approximated in cartesian coordinates as a circle of radius 26 550 km ($R_o = 26\,550$ km) with constant speed over a 12-hour orbit. The observer is on a static circular earth of radius 6360 km ($R_e = 6360$ km), standing at the point $x = 0$, $y = 6360$ km. The zero-time epoch ($t = 0$) for this calculation occurs when the satellite passes through the positive X axis, meaning it does not rise above the observer's horizon until approximately $t = 27$ minutes. This scenario is illustrated in Figure D.1. The satellite range and Doppler dynamics are calculated analytically based on this model.

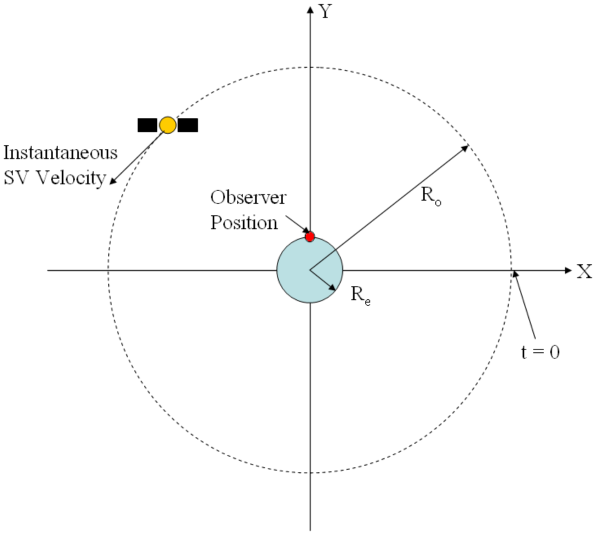

Figure D.1: Model for Approximation of Worst-Case SV Doppler Dynamics

D.2.1 Satellite Range

In the scenario of Figure D.1, the SV-observer range as a function of time is calculated in cartesian coordinates as

$$r(t) = \sqrt{x(t)^2 + (y(t) - R_e)^2} \tag{D.2}$$

where

$$\begin{aligned} y(t) &= R_o \sin(\omega t), \text{ and} \\ x(t) &= R_o \cos(\omega t), \text{ assuming} \\ T &= \text{Orbital Period (43 200 s) , and} \\ \omega &= \frac{2\pi}{T}. \end{aligned}$$

Replacing the terms $x(t)$ and $y(t)$ in Equation D.2 with their equivalents, expanding the square, and reducing with trigonometric identities yields a function of t:

$$r(t) = \sqrt{R_o^2 + R_e^2 + -2R_eR_o\sin(\omega t)}. \tag{D.3}$$

The range function for this situation is presented in Figure D.2(a) for the period during which the simulated satellite is above the observer's horizon.

D.2.2 Range Rate and Doppler

The first derivative of Equation D.3 gives the range rate:

$$\dot{r}(t) = \frac{-R_eR_o\omega\cos(\omega t)}{\sqrt{R_o^2 + R_e^2 - 2R_oR_e\sin(\omega t)}}. \tag{D.4}$$

If we allow

$$\begin{aligned} K_1 &= -R_eR_o\omega, \text{and} \\ K_2 &= R_e^2 + R_o^2, \end{aligned}$$

the range rate equation simplifies to

$$\dot{r}(t) = \frac{K_1\cos(\omega t)}{\sqrt{K_2 + 2\frac{K_1}{\omega}\sin(\omega t)}}. \tag{D.5}$$

The instantaneous doppler is found by converting range rate to phase rate. At the GPS L1 transmitted frequency of 1575.42 MHz, the wavelength is approximately 0.19 m, giving approximately 5.25 cycles/m. The Doppler is therefore found by dividing Equation D.5 by 0.19 m.

$$\dot{\phi}(t) = \frac{1}{0.19\text{ m}}\frac{K_1\cos(\omega t)}{\sqrt{K_2 + 2\frac{K_1}{\omega}\sin(\omega t)}}. \tag{D.6}$$

The Doppler values are presented in Figure D.2(b) for the period during which the simulated satellite is above the observer's horizon. Note that the convention has been used whereby a negative Doppler indicates a decreasing range. This convention is carried through the rest of the analysis in this appendix.

D.2.3 Doppler Drift

Doppler drift, $\ddot{\phi}$, is the first derivative of Equation D.6 with respect to time. This parameter corresponds to acceleration of the satellite in the direction away from the observer. The cumulative effect of an initial Doppler drift is calculated as $\ddot{\phi}t$.

$$\ddot{\phi}(t) = \frac{1}{0.19\ \mathrm{m}}\left[\frac{-[K_1\cos(\omega t)]^2}{[K_2 + 2\frac{K_1}{\omega}\sin(\omega t)]^{3/2}} - \frac{\omega K_1 \sin(\omega t)}{[K_2 + 2\frac{K_1}{\omega}\sin(\omega t)]^{1/2}}\right] \tag{D.7}$$

An equivalent form for the Doppler drift equation is obtained by multiplying the second term in Equation D.7 to obtain a common denominator.

$$\ddot{\phi}(t) = -\frac{1}{0.19\ \mathrm{m}}\frac{K_1^2 + K_1^2\sin^2(\omega t) + K_1 K_2 \omega \sin(\omega t)}{[K_2 + 2\frac{K_1}{\omega}\sin(\omega t)]^{3/2}} \tag{D.8}$$

The Doppler drift values for the period of satellite visibility are presented in Figure D.2(c). The maximum drift is on the order of 0.9 Hz/s. In a 60-second data set, therefore, the maximum linear drift could contribute approximately $0.9\ \mathrm{Hz/s} \times 60\ \mathrm{s} = 54\ \mathrm{Hz}$ to the change in received Doppler.

D.2.4 Doppler Jerk

The third derivative of the satellite position vector is its jerk. While this is only the the second derivative of Equation D.6 with respect to time, it will be referred to herein as 'Doppler jerk' (represented by the symbol J_d) to maintain consistency between position effects and Doppler effects. The contribution of this quadratic term over a time is calculated as $\frac{1}{2}J_d t^2$.

$$J_d = \frac{\cos(\omega t)K_1}{0.19\text{ m}}\left[\frac{2K_1^2 + K_1^2\cos^2(\omega t) - K_1K_2\omega\sin(\omega t) - K_2^2\omega^2}{[K_2 + 2\frac{K_1}{\omega}\sin(\omega t)]^{5/2}}\right] \tag{D.9}$$

The jerk is presented in Figure D.2(d). The maximum value is approximately 1.3×10^{-4} Hz/s^2. Table D.1 lists the cumulative Doppler contribution over increasing time periods for the maximum constant jerk of 1.3×10^{-4} Hz/s^2. The effect is minimal over short periods of up to 10 seconds, but becomes significant over longer periods, especially over the course of a 60-second data set.

T(ms)	2nd Order Doppler Contribution (Hz)
100	6.5×10^{-7}
1000	6.5×10^{-5}
5000	1.625×10^{-3}
10000	6.5×10^{-3}
50000	1.625×10^{-1}

Table D.1: Maximum Contribution of 2nd-Order Effects

D.2.5 Third- and Higher-Order Effects

While the next higher-order effect has not been explicitly calculated, the values of Doppler jerk from Equation D.9 provide a numerical estimate of the effect. The maximum absolute value of $\dot{J}_d$ is approximately 4.3×10^{-8} Hz/s^3. This maximum level of third-order effect contributes to Doppler change over time in an amount calculated as $\frac{1}{6}\dot{J}_d t^3$. The cumulative effect of this maximum third-order parameter is shown in Table D.2 for various periods. It is clear that third-order effects are

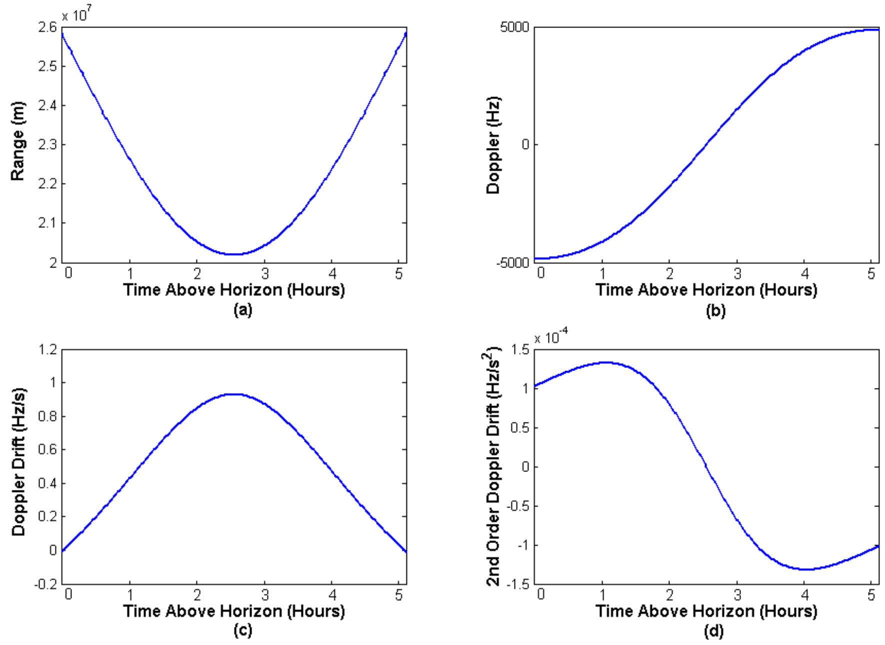

Figure D.2: SV Range, Doppler, and Drift under worst case orbit

insignificant until processing in excess of 50 s of data because the power rolloff function first-null width remains significantly larger than any third-order effects up to that point. However, longer-term predictions must account for at least the third-order effect to maintain accuracy, as seen in Table D.2.

T (s)	3rd Order Doppler Contribution (Hz)	T (min)	3rd Order Doppler Contribution (Hz)
1	7.17×10^{-9}	1.0	1.55×10^{-3}
5	8.96×10^{-7}	2.0	1.24×10^{-2}
10	7.17×10^{-6}	5.0	1.94×10^{-1}
60	1.55×10^{-3}	10.0	1.55

Table D.2: Maximum Contribution of 3rd-Order Effects

D.3 Necessary Polynomial Degree

The preceding analysis shows that over 60 seconds, a second-order polynomial is sufficient to describe the Doppler effect due to SV motion with less than 1.55×10^{-3} Hz error. This level of error is the maximum contribution of the third-order effect which is ignored in the second-order polynomial. Most Doppler change is due to the linear drift coefficient, with the quadratic component contributing less than 0.2 Hz over 60 s.

The generic second-order polynomial has the form

$$\dot{\phi}(t) = a_0 + a_1 t + a_2 t^2. \tag{D.10}$$

To maintain consistency between the polynomial and the physical nature of the dynamics, the following specific form of polynomial will be used:

$$\dot{\phi}(t) = \dot{\phi}(0) + \ddot{\phi}_o t + \frac{1}{2} J_d t^2, \tag{D.11}$$

where $\dot{\phi}(t)$ is the Doppler at time t, $\dot{\phi}(0)$ the initial Doppler at time 0, $\ddot{\phi}_o$ the initial linear drift rate at time 0, and J_d the constant Doppler jerk.

Appendix E

Noise Level Measurements

The following figures represent centre correlator power under various conditions for each data set. Power output from the accumulation and demodulation process is shown for four cases:

- Local code not present in data; 1 ms accumulation
- Local code not present in data; 5 ms accumulation
- Local code not present in data; 20 ms accumulation
- Strong signal in data; 1 ms accumulation

The figures show measured probability distributions that are fitted to theoretical scaled noncentral chi-squared distributions, from which the mean and standard deviation of noise power are determined. These distributions imply the mean and variance of two equal source Gaussian distributions that would result in the observed distributions if squared and added.

E.1 Tube Reference Data Set

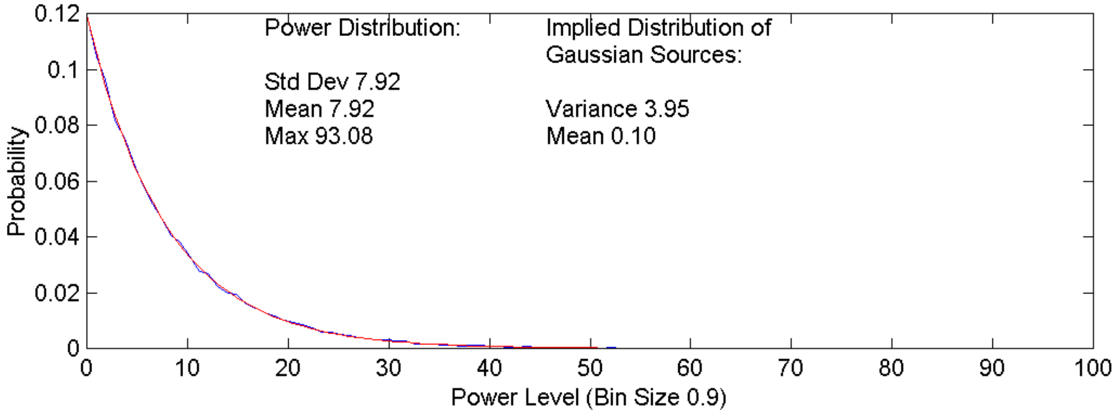

Figure E.1: Tube Reference Noise Power – 1 ms Integration

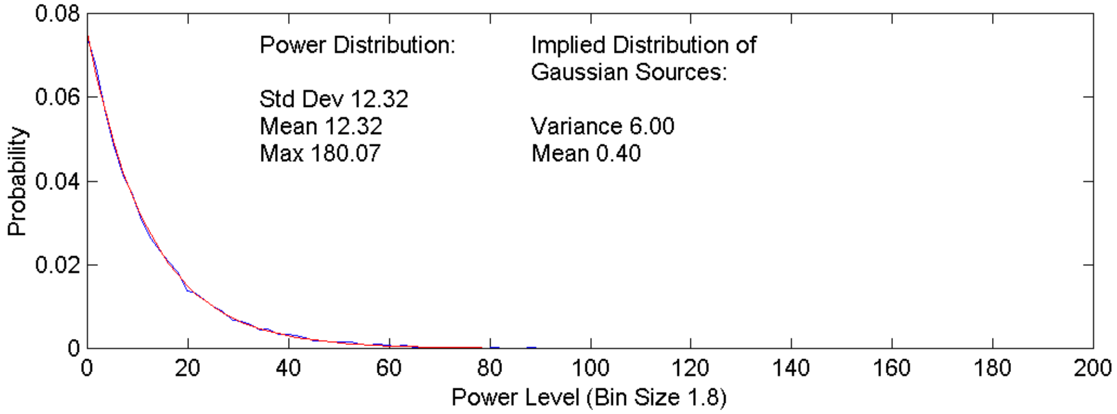

Figure E.2: Tube Reference Noise Power – 5 ms Integration

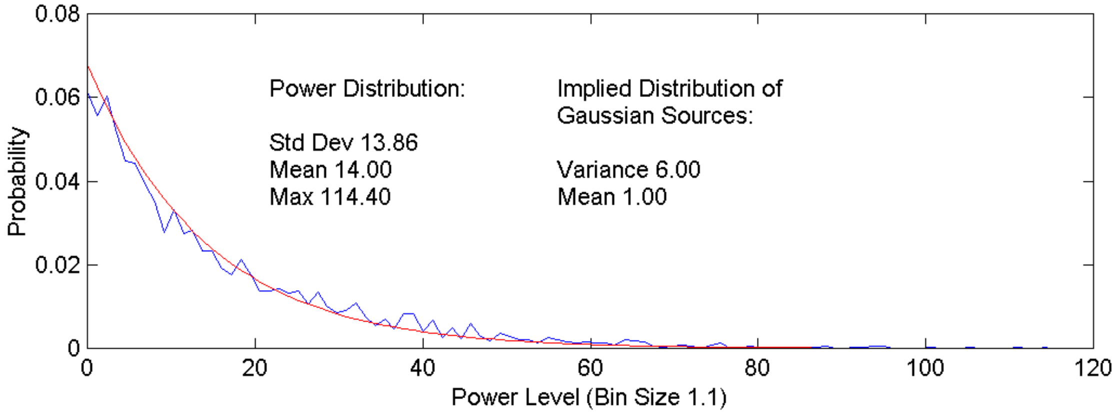

Figure E.3: Tube Reference Noise Power – 20 ms Integration

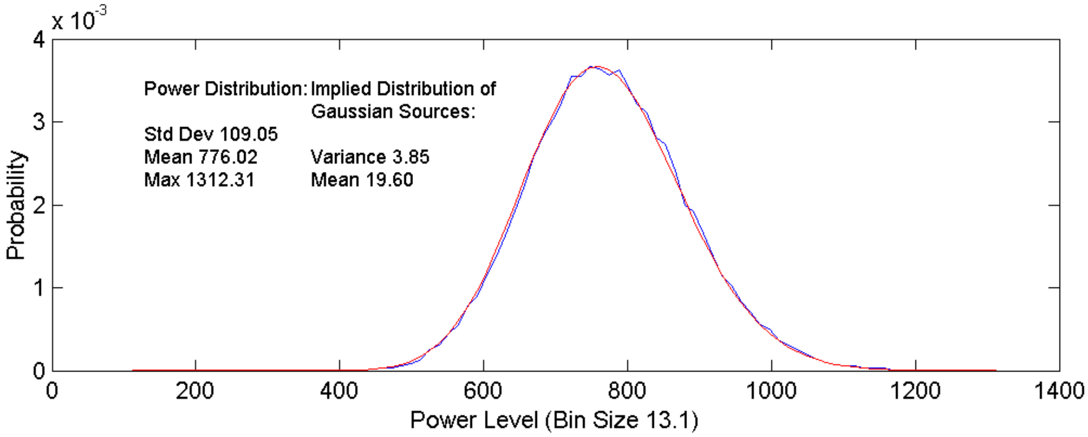

Figure E.4: Tube Reference Power PRN 8 – 1 ms Integration

E.2 Terraario Reference Data Set

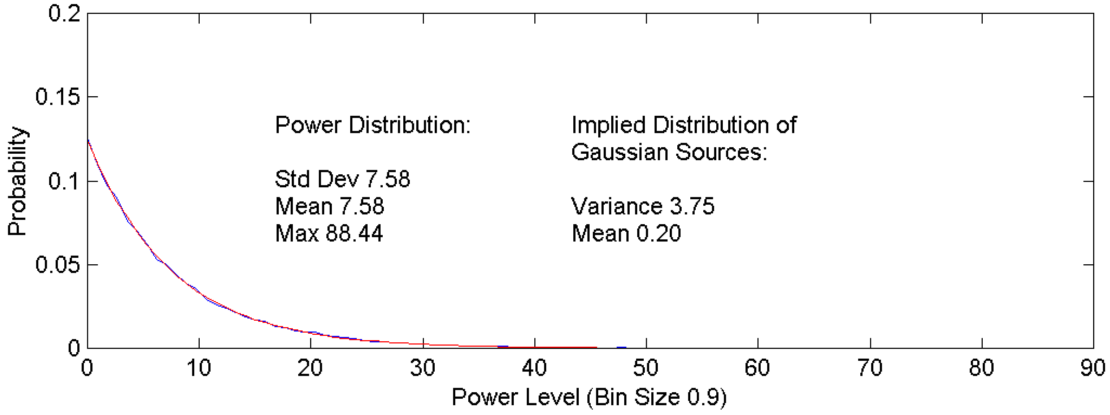

Figure E.5: Terraario Reference Noise Power – 1 ms Integration

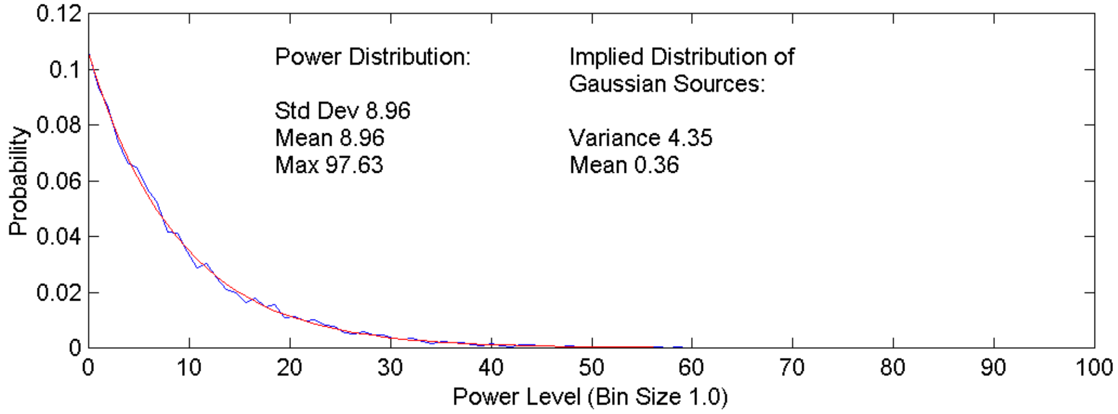

Figure E.6: Terraario Reference Noise Power – 5 ms Integration

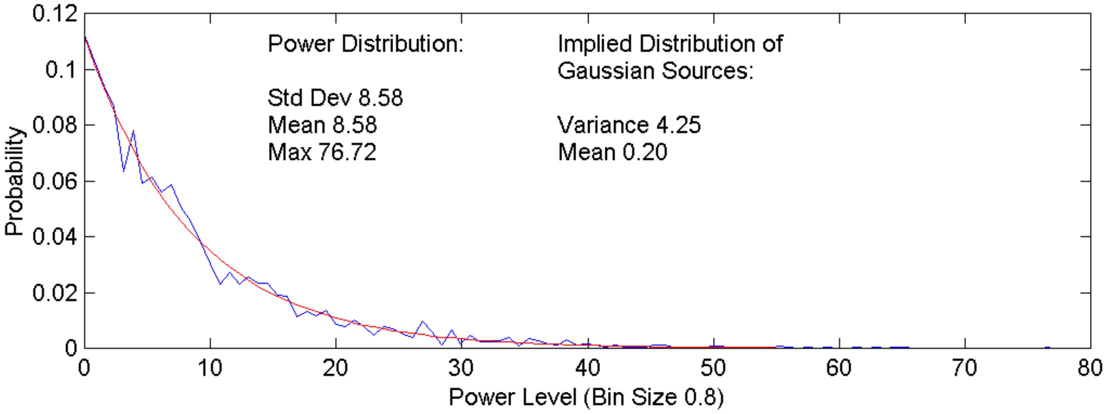

Figure E.7: Terraario Reference Noise Power – 20 ms Integration

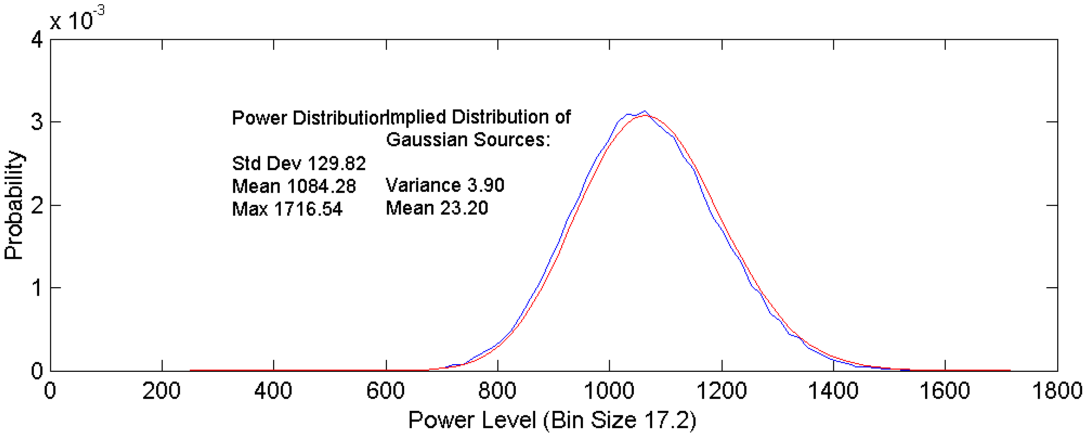

Figure E.8: Terraario Reference Power PRN 8 – 1 ms Integration

E.3 Tube Rover Data Set

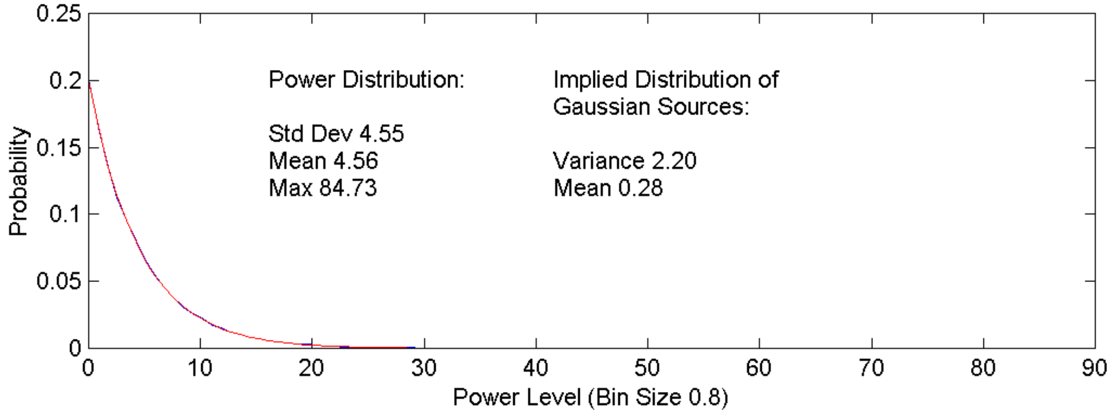

Figure E.9: Tube Rover Noise Power – 1 ms Integration

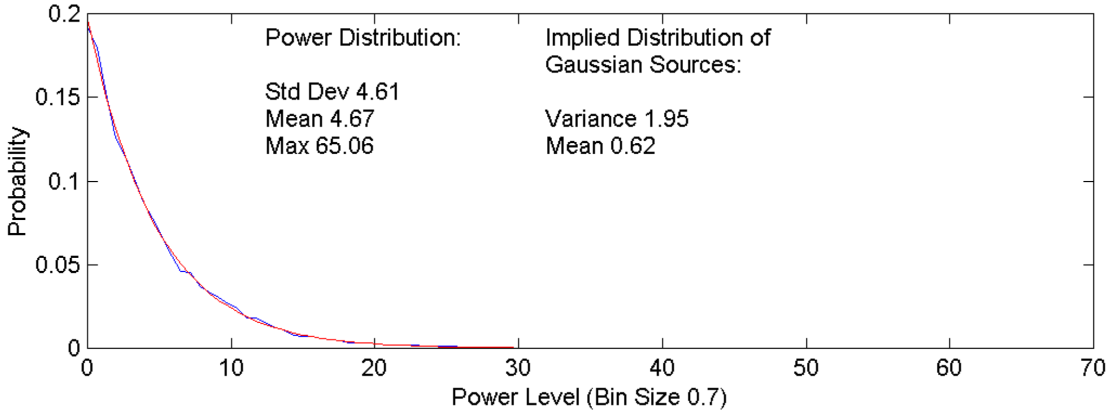

Figure E.10: Tube Rover Noise Power – 5 ms Integration

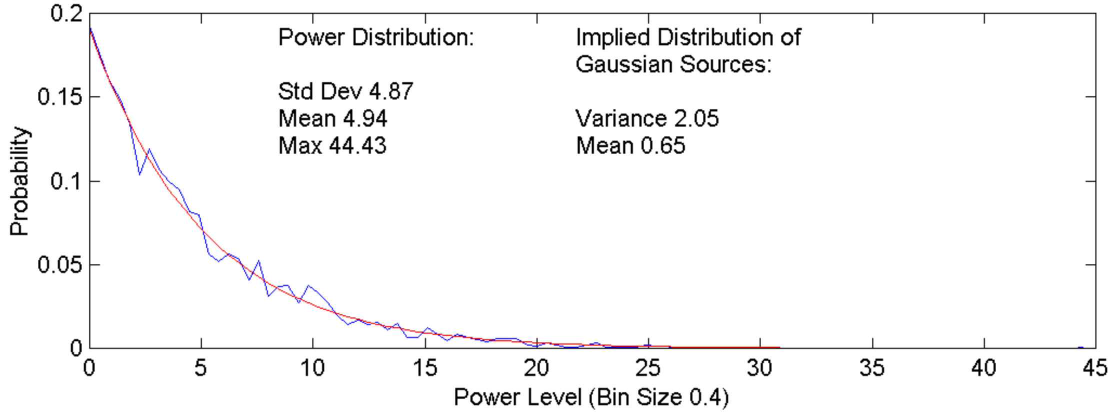

Figure E.11: Tube Rover Noise Power – 20 ms Integration

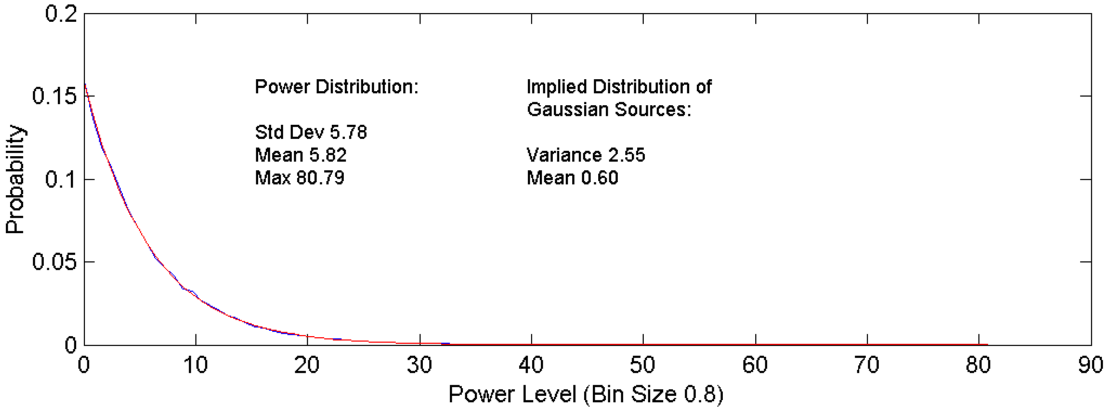

Figure E.12: Tube Rover Power PRN 8 – 1 ms Integration

E.4 Terraario Rover Data Set

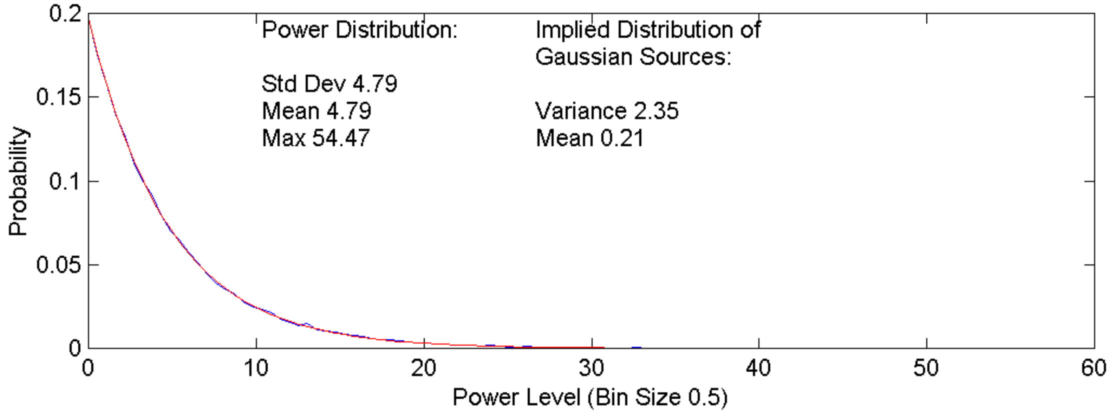

Figure E.13: Terraario Rover Noise Power – 1 ms Integration

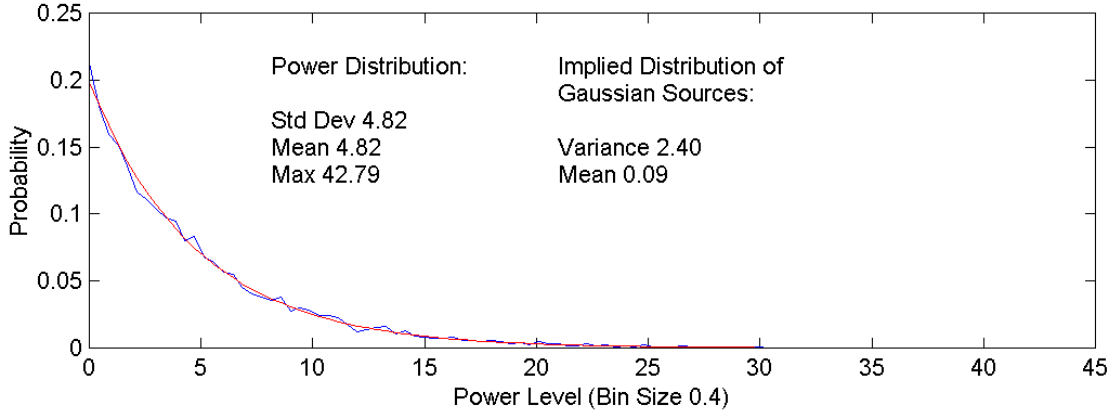

Figure E.14: Terraario Rover Noise Power – 5 ms Integration

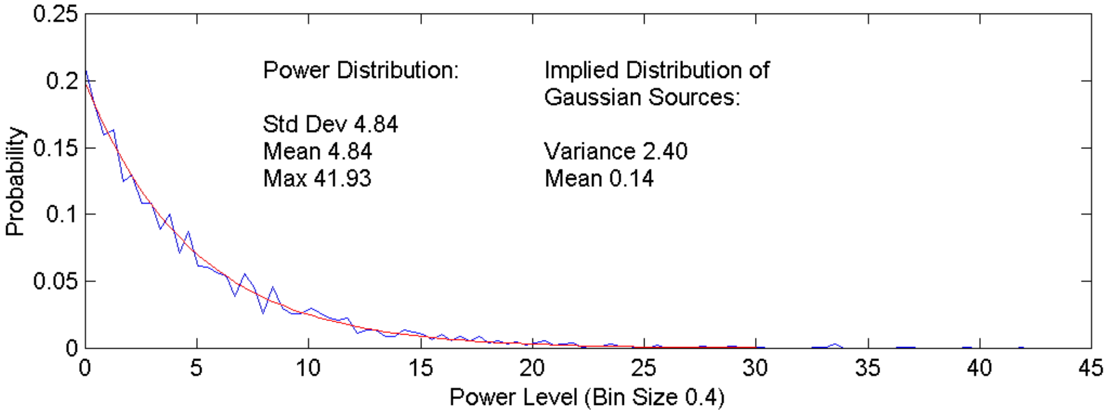

Figure E.15: Terraario Rover Noise Power – 20 ms Integration

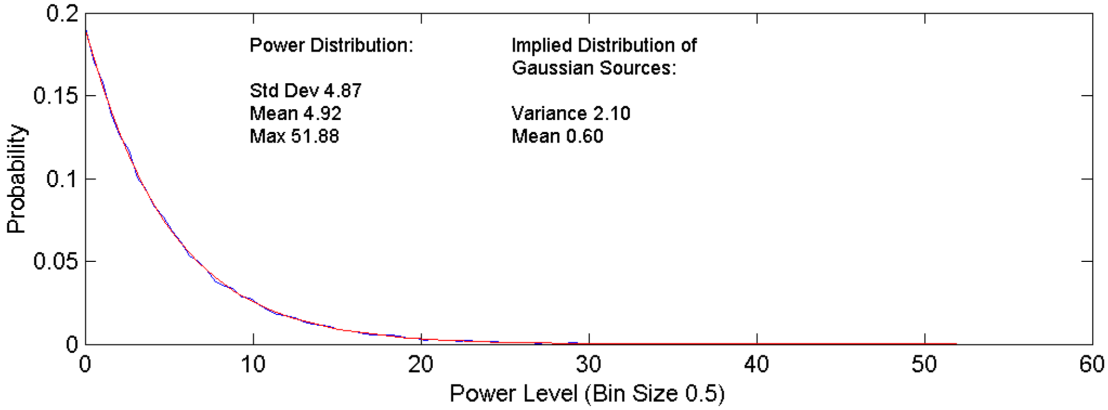

Figure E.16: Terraario Rover Power PRN 8 – 1 ms Integration